DESIGN AND ENGINEERING OF ADVANCED SI-BASED THIN FILM ANODE MATERIALS FOR LI-ION BATTERIES

by

Aliya Mukanova

A Dissertation Presented in Partial Fulfillment of the Requirements for the Degree of Doctor of Philosophy (Ph.D.) in Science, Engineering and Technology

NAZARBAYEV UNIVERSITY

2019

A Dissertation Presented in Partial Fulfillment

of the Requirements of Nazarbayev University

for the Degree of Doctor of Philosophy (Ph.D.) in Science,

Engineering and Technology

DESIGN AND ENGINEERING OF ADVANCED SI-BASED THIN FILM ANODE MATERIALS FOR LI-ION BATTERIES

by

Aliya Mukanova

Supervisor	**Zhumabay Bakenov**
Co-supervisor	**Arailym Nurpeissova**
External supervisors	**Sung-Soo Kim and Maksym Myronov**

ABSTRACT

Lithium-ion batteries (LIBs) are a versatile way of energy conversion and storage. Thin film batteries are the next generation of Li-ion battery technology with the thickness of tens μm and aimed to power a diverse range of microdevices. In order to increase the storage possibility, i.e. capacity, of such batteries, new high capacity electrode materials should be developed. Silicon-based materials are the most promising anodes due to the highest theoretical capacity and a low potential. However, the current drawbacks of Si such as significant volume expansion, electrical contact loss, and low conductivity impede its practical application in LIBs and commercialization. In this doctoral thesis, the research has been performed in two main directions in order to improve the existing microbatteries and find a way to develop a stable Si-based thin film electrode.

The first direction is an investigation of novel silicon carbide thin film (3C-SiC) with a cubic lattice as an anode for LIBs. The advanced method of "single" particle measurement for studying the electrochemical properties of an individual microparticle provided the new data which allowed suggesting the mechanisms of lithiation/delithiation in 3C-SiC film. The use of XRD, TEM, XPS, Raman spectroscopy confirmed that there was no degradation of the 3C-SiC crystal lattice. The obtained results demonstrated that there are in two possible reasons of 3C-SiC thin film electrochemical activity, an intercalation or a capacitance.

The second direction is the design of the three-dimensional (3D) amorphous Si (a-Si) thin film anode. The improvement of a-Si thin film anode was achieved through studying the effects of substrate surface condition, dopants incorporation, electrolyte additive and addition of graphene (GF) underlayer. The designed *n*-type doped porous a-Si thin film and 3D a-Si/GF anode exhibited high electrochemical performance in the lithium cells for several hundred cycles.

TABLE OF CONTENTS

LIST OF TABLES

LIST OF FIGURES

ACRONYMS AND DEFINITIONS

2D	two-dimensional
3D	three-dimensional
AFM	atomic force microscopy
BC	ballistic consolidation
BMS	battery management systems
CC	current collector
CE	coulombic efficiency
CNT	carbon nanotubes
CV	cyclic voltammetry
CVD	chemical vapor deposition
DEC	diethyl carbonate
DIW	deionized water
DMC	dimethyl carbonate
EC	ethylene carbonate
EBE	electron beam evaporation
ED	electrodeposition
EIS	electrochemical impedance spectroscopy
EMC	ethyl methyl carbonate
ECR-MO	Electron Cyclotron Resonance Metal Organic
FEC	fluoroethylene carbonate
FIB	focused ion beam
FTIR	furrier transform Infra-Red Spectroscopy
GC	galvanostatic charge/discharge cycling
GD	glow discharge
GF	graphene
IBD	ion-beam deposition
LFP	lithium iron phosphate
LIBs	lithium-ion batteries

LiBOB	lithium bis(oxalato) borate
LIMBs	lithium-ion microbatteries
LIPON	lithium phosphorus oxynitride
LiTFSI	lithium bis(trifluoromethylsulphonyl)imide
LTO	lithium titanium oxide
LP	low pressure
LPF	lithium hexafluorophosphate
NMP	N-Methyl-2-pyrrolidone
MS	magnetron sputtering
PC	propylene carbonate
PDMS	poly(dimethylsiloxane)
PED	pulsed electron deposition
PE	plasma enhanced
PLD	plasma laser deposition
PMMA	poly(methylmetacrylate)
PVCA	poly(vinyl carbonate)
PVDF	poly(vinylidene fluoride)
QCM	quartz crystal microbalance system
RF, *rf*	radio frequiency
RP	reduced pressure
SEI	solid electrolyte interphase
SEM	scanning electron microscopy
SS	solid state
TEM	transmission electron microscopy
TMOS	trimethoxymethyl silane
VE	vacuum evaporation
VC	vinylene carbonate
XRD	X-ray diffraction
XPS	X-ray photoelectron spectroscopy

AKNOWLEDGMENTS

First of all, I want to thank my supervisor, a great scientist and person, Prof Zhumabay Bakenov, who provided all opportunities for the implementation of this research; my foreign supervisors, Prof Sung-Soo Kim and Prof Maksym Myronov, for their advice and friendship; my co-supervisor Dr. Arailym Nurpeissova, who helped me a lot and has become a close friend, the junior researchers Assem and Assel, who were my extra hands and responsible assistants, and all my colleagues from the battery group, Berik, Almagul, Indira, Sandugash, Nurbol and others, who together have become my another family.

I would like to express the sincere and deep appreciation to my parents Elena and Orazaly, who since childhood encouraged me to go to science; my parents-in-law Svetlana and Sagnay, who looked after my children and home; my husband Aidos, who did not allow me to decline a university offer; my sister Galiya, who always believed in me; and my kids Rasul and Salikha, who motivated me to be a good example for them in future.

DECLARATION

I, Aliya Mukanova, declare that the scientific research presented in this Thesis is my own original work. I confirm that the information derived from other sources has been properly indicated and referenced in the thesis.

The Thesis has not been previously submitted to this or any other university for a degree, and does not incorporate any material already submitted for a degree.

1 INTRODUCTION

1.1 Motivation for Research

The rechargeable lithium-ion batteries (LIBs) are able to provide the most reliable way towards safe portable or off-grid energy that makes many modern conveniences come true. Miniaturization of power sources is extremely important for modern electronic technology, especially for microdevices, that have become essential in many aspects of our life like living, work and health. Current microbatteries are usually nuclear fuel cells, which in spite of the almost infinite life, are low energy and can negatively influence on the human body due to radioactivity [1]. Therefore, the development of safe, non-toxic and low-cost microbatteries is of paramount interest.

Thin film lithium-ion microbatteries (LIMBs) are the advanced direction in Li-ion technology that can achieve high volumetric and gravimetric energy densities at small dimensions (Fig. 1a) [2]. However, in order to achieve them, the battery cell electrolyte and electrode materials and configuration must be properly chosen and optimized. The modern LIMB is on the earliest step of the development. The many materials were tried and investigated so far for LIMBs. However, there are still many challenges related to low capacity or energy density, safety, durability, flexibility, and cost. The development of the most promising electrode materials as well as the search for new materials, which able to change the current state of energy storage field, are the main routes to solve the existing problems.

The high impact of energy storage devices for biological/medical devices (hearing aid, pacemaker, in vivo imaging, etc.) and self-powered microelectronics (actuators, miniature transmitters, sensors, etc.) on economics and society indicates that the development of new materials for such applications has strong social impact providing development and availability of healthcare devices, enhancement of security and safety, raising the education and science level, and will accelerate the development of technologies and relevant industries. On the other hand, the

technological development in all fields demands high energy batteries as power sources, energy backup and storage systems with high durability, stability, and safety. Therefore, new high-performance battery materials are urged by these demands and play a critical role in the technological developments in many fields from medical applications to high power energy storage, electric transport, and portable electronics.

The actuality of this PhD research topic is also confirmed by the market review for the production of microbatteries. Today, micro-sized batteries are commercialized by only a few companies (PowerPaper, Cymbet, Infinite Power Solutions, and ST Microelectronics, Johnson Battery Technology, Front Edge and I-TEN). Currently, the market for microbatteries is small, but in the following years, it is expected to grow from $ 7 million to more than $ 400 million in 2026. Therefore, the prospect of developing advanced thin-film anode materials for future commercialization and their entry into a new wave of development of microsized energy sources is beyond any doubt.

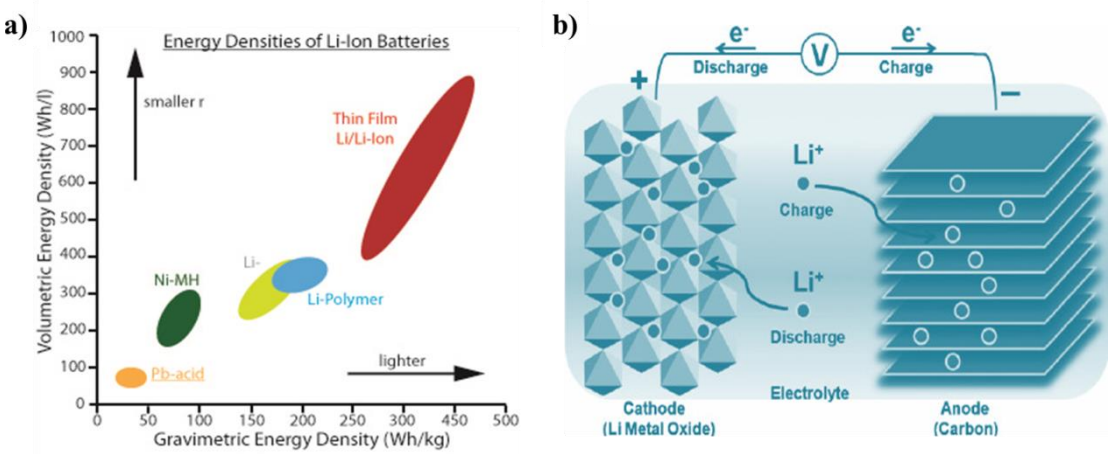

Fig. 1 (a) Ragone plot of various energy storage systems [3], (b) schematic representation of LIB structure and mechanism.

1.2 Battery operation and terms

Among existing types of rechargeable batteries like nickel-metal hybrid, lead-acid, nickel-cadmium, and lithium-ion polymer, LIBs are leading the path for energy

storage and power supply for a wide range of applications from portable electronics to electric vehicles, due to their high energy density and long lifespan [4]. From Fig. 1a, the Ragone chart demonstrates the advantages of LIBs in terms of gravimetric and volumetric energy densities over lead-acid, nickel-cadmium, and nickel-metal hydride batteries.

Battery stores and releases energy by the continuous movement of electrons from one of its end to the opposite. This flow of moving electrons (the electric current) can be used to power device. These two batteries "ends" are known as electrodes. One electrode is called the anode or negative electrode and the other is called the cathode or positive electrode. Generally, the anode in LIBs is graphitized carbon and the cathode can be made from a chemical compound known as a metal oxide (cobalt oxide, for example). The final battery ingredient is the electrolyte, which sits between the two electrodes preventing them from short-circuiting being ionically conductive. In the case of LIBs, the electrolyte is a solution of a salt that contains Li^+ ions.

In general, LIBs work based on principles of reversible oxidation/reduction reactions (Fig. 1b). During the charging process, Li^+ ions move from the positive electrode, through the electrolyte, into the negative electrode. The electrons of the first electrode travel via a different path, i.e. around the external circuit. Further, both ions and electrons move to the negative electrode resulting in insertion process. When ions do not flow anymore, this, generally, means that the battery is charged and 'ready to use'.

The discharge of the battery is essentially the opposite process. The ions and electrons that moved to the anode travel back again to the cathode. Similarly, ions drift through the separator/electrolyte and the electrons take another way around the circuit, until they both meet at the anode, depositing lithium, and eventually, powering the device that uses LIBs. When all the Li^+ ions return into the cathode (from the anode) battery has been drained and needs recharging. [5]

In order to understand what is going on during the electrochemical reactions, below is given an example of the reversible redox reactions taking place in a Si/ $LiFePO_4$ (LFP) full cell at both anode and cathode [6]:

$$\text{Anode: } Li_xSi \leftrightarrow Si + xLi^+ + xe^-;$$

$$\text{Cathode: } Li_{x+y}FePO_4 \leftrightarrow xLi^+ + xe^- + Li_y\,FePO_4.$$

Electrochemical reactions at two terminals with active electrode materials release the stored chemical energy. The electrode materials selected determine the total change of Gibbs free energy ΔG as a result of the electrochemical reactions on the two electrodes. The theoretical cell voltage ($\Delta E = -\Delta G/nF$) can be estimated using given the overall electrochemical reaction and charges transferred.

The performance of LIBs is usually evaluated by the following parameters:

Specific (volumetric) energy (Wh kg^{-1} or Wh m^{-3}) measures the amount of energy that can be stored and released per unit weight (volume) of the battery that is obtained by multiplying the specific (volumetric) capacity (Ah kg^{-1} or Ah m^{-3}) with operating battery potential (V).

Specific capacity measures the amount of charge that can be reversibly stored per unit weight. It is closely related to the number of electrons released per mole of an electrochemical reaction and the atomic weight of the host compound.

Areal and volumetric capacities are the capacities of material or whole cell per surface and volume unit, respectively that sometimes are used as the alternative units where it is appropriate.

Cyclability called also *cycle life*, measures the reversibility of the Li^+ ion insertion and extraction processes, in terms of the number of charging and discharging cycles before the battery loses energy significantly or can no longer sustain function of the device it powers. Also, this term is defined as the dependence of the specific capacity on the number of charge-discharge cycles.

Coulombic efficiency (CE) is the charge efficiency by which electrons are transferred in batteries. CE is the ratio of the total charge extracted from the battery to the total charge put into the battery over a full cycle.

Discharging/charging rate is related to the *current density (A* cm^{-2}*)* applied during discharge and charge, and which is a mere of the speed of the lithiation/delithiation process.

Safety requirements are very high for LIBs with multiple cells. For the battery cells/packs/modules, a *battery management system* (BMS) should be used in order to prevent possible thermal runaway. If a battery cell fails inside a battery pack, the BMS detects and isolates this particular cell [7].

1.3 Materials and research concept

Despite being the most powerful technology among secondary batteries, LIBs cannot meet the demands posed on electrochemical power sources for next-generation electric vehicles, mobile electronics and future generations of other portable devices. Currently, energy and power densities of these batteries are limited by the capacity of commonly used anode – graphite, which has a theoretical capacity of 372 mAh g^{-1}.

Thin film batteries are the next-generation of LIMBs technology, that are inherently simple in concept comprising fire-safe solid state (SS) components of lightweight and compact configuration. The key advantages of thin film electrodes are that it can be deposited directly on any shape with any size using the same techniques as for microdevices manufacturing. The thickness of the battery ranges from 10 to 15 μm, which allows high volumetric energy densities to achieve. The microbatteries are being intensively developed to create new power sources for a diverse range of applications, such as neural and cardio stimulators, smart cards, drug delivery systems, small-scale sensors, radio frequency identification devices, and other portable electronics [7, 8]. Crystalline $LiCoO_2$ (LCO), V_2O_5, $LiMn_2O_4$ (LMO), LFP are usually used as the thin film cathode materials and capable of being cycled

for thousands of times with excellent stability [10]. Lithium phosphorus oxynitride (LiPON) is a commonly used Li-based glass SS electrolyte which possesses a good ionic conductivity with high structural stability. Tin (Sn), carbon (C) or lithium titanate ($Li_4Ti_5O_{12}$) materials are successfully used as anodes for thin film batteries since a use of Li metal as an anode is limited by its high chemical reactivity and melting at higher operation temperatures [11]. Besides, some of these anodes suffer from degradation after being in contact with Li^+ ions, others cannot improve the performance of LIBs due to limited physical and chemical properties.

Anodes based on mainstream semiconductor amorphous silicon (Si) are of paramount interest due to its high theoretical Li^+ ions storage capacity of 4200 mAh g^{-1}, the enormous volumetric capacity of 9786 mAh cm^{-3}, a low operating voltage *vs.* Li/Li^+ – 0.4 V, low cost, safety and abundant availability [12]. Extensive research has been made so far on Si-based thin film anodes [13]; however, the problems of volume variation and rapid capacity fading during cycling still demand practical solutions. Numerous attempts towards the development of stable Si-based anode materials with excellent Li^+ ions storage capability keep being made and the engineering of novel types of materials is still in progress [12, 13].

Another Si-based material - SiC, has been considered as an electrochemically inert material in respect to Li^+ ions for many years [15]. However, it was recently published that SiC can serve as a matrix for Li^+ ions intercalation at which no visible volume expansion occurs. In some sources, it is reported that SiC with cubic lattice (3C-SiC) theoretically can achieve the specific capacity of around 2638 $mAhg^{-1}$ if it is alloyed with Li^+ ions [13, 14]. Considering its superior mechanical stability and possible Li^+ ions storage ability, 3C-SiC can be the promising candidate anode materials. No studies have been devoted to investigate the electrochemical properties of the epitaxial 3C-SiC thin film anode with high crystallinity so far. Therefore, this material is unique and new for LIBs, and the data obtained within this PhD research will bring new insights into the electrochemical behavior of 3C-SiC and its potential application in rechargeable batteries.

Topology is another key that could lead to the enhancement of the battery's anode characteristics [15, 16]. Planar thin film materials are limited by surface area, which obviously plays a crucial role in boosting the electrochemical properties of the electrode materials. In this regard, 3D structured surface morphology can provide a higher specific surface area for chemical reactions with Li^+ ions. Furthermore, the introduction of dopants into Si-based anodes structure has proved to have a positive effect on the electrochemical properties due to enhanced conductivity [17, 18].

1.4 Aim, key objectives, and novelty

The **main aim** of this doctoral dissertation is to study advanced Si-based thin film anode materials and develop the 3D structured anode with stable cyclability and high-energy efficiency for energy storage and conversion applications.

In accordance with the justification provided in the previous section (§1.3), two materials, Si and SiC, were chosen as *the objects of investigation* within this PhD research which contained two main objectives. To the successful implementation of the project, several tasks were determined for each material as well.

Objective 1 is studying a new thin film Si-based material, SiC, as an anode for LIBs.

1. Preparation and characterization.
2. Investigation of the interaction SiC with Li.
3. Investigation of electrochemical activity of material towards to Li^+ ions.

Objective 2 is developing high-performance 3D Si-based thin film anodes for LIMBs.

1. Preparation of Si-based anodes and characterization.
2. Improving an electrochemical cycling performance of the Si thin film anodes.
3. Design novel 3D structured composite Si-graphene thin film anode

The main research approach is reflected in the **hypothesis** of PhD research:

"*If* we use Si-based materials in the shape of thin films with enough dopants' concentration and 3D structure as the anodes for LIBs, *then* the cycling performance and energy efficiency of such battery will be improved, *because* doping incorporation and high surface thin film can enhance electron mobility whilst providing a stable electroconductive network and high current rates".

Novelty of research is, first of all, the new insights obtained through studying the new candidate anode material, 3C-SiC; improving the cycling performance of existing Si anode materials; investigating Si structural and electrical properties before, during and after cycling; design of novel 3D structured Si-based composite anode.

1.5 Role of collaborators and thesis outputs

Collaborators

The main collaborators and simultaneously external supervisors of this doctoral research are:

- Prof Sung-Soo Kim, Dean of the Department of Energy Science and Technology of the Chungnam National University, the head of the Energy Storage and Conversion Lab (Daejeon, South Korea). He advised on the results of electrochemical studies, gave recommendations on the further implementation of the tasks, participated in the adjustment of scientific articles and provided access to the facility for "single" particle measurements.
- Prof Maksym Myronov, a leader of the Nano-Silicon group in the University of Warwick (Coventry, United Kingdom). He provided samples of thin films of single-crystal silicon carbide and participated in the formulation of tasks for the study of this material. Characterization of samples of silicon and its carbide after interaction with metallic lithium at elevated temperatures were performed in his laboratory.

Thesis outputs

During the research 4 full peer-reviewed papers, 2 peer-reviewed conference proceedings were published and two papers were submitted, and it was applied for 1 patent. The list is presented below.

Patent:

1. Silicon carbide and silicon nitride with monocrystalline structure as an anode for rechargeable batteries, Zhumabay Bakenov, Aliya Mukanova, Maksym Myronov / Kazakhstan patent, application № 2018/0102.1 from 15.02.2018 (local, in Russian), *submitted.*

Articles (peer-reviewed):

1. Aliya Mukanova, Arailym Nurpeissova, Arshat Urazbayev, Sung-Soo Kim, Maksym Myronov, Zhumabay Bakenov, Silicon thin film on graphene coated nickel foam as an anode for Li-ion batteries, *Electrochimica Acta* 258, 800-806 (2017) https://doi.org/10.1016/j.electacta.2017.11.129. IF=4.8. Q1

2. Aliya Mukanova, Arailym Nurpeissova, Sung-Soo Kim, Maksym Myronov, Zhumabay Bakenov, *N*-type doped silicon thin film on porous Cu current collector as a negative electrode for Li-ion batteries, *ChemistryOpen* 7(1), 92-96 (2018) http://onlinelibrary.wiley.com/doi/10.1002/open.201700162/epdf. IF=2.9. Q1

3. Aliya Mukanova, Assem Zharbossyn, Arailym Nurpeissova, Sung-Soo Kim, Maksym Myronov, Zhumabay Bakenov, Electrochemical study of graphene coated nickel foam as an anode for lithium-ion battery, *Eurasian Chemico-Technological Journal* 20(2) (2018) 91-97. CS=0.28. Q4

4. Aliya Mukanova, Albina Jetybayeva, Seung-Taek Myung, Sung-Soo Kim, Zhumabay Bakenov, A mini-review on the development of Si-based thin film anodes for Li-ion batteries, *Materials Today Energy*, 9 (2018) 49-66. Q1

5. Aliya Mukanova, Gerard Colston, Arailym Nurpeissova, Sung-Soo Kim, Seung-Taek Myung, Maksym Myronov, Zhumabay Bakenov, High performance

electrodes for lithium-ion microbatteries made of epitaxial semiconductors, *Journal of Power Sources*, submitted. Q1

6. Aliya Mukanova, Assel Serikkazyeva, Arailym Nurpeissova, Sung-Soo Kim, Maksym Myronov, Zhumabay Bakenov, Effect of *p*-, *n*-type dopants and vinyl carbonate electrolyte additive on electrochemical performance of Si thin film anodes for lithium-ion battery, *Journal of Power Sources*, submitted. Q1

Conference Proceedings (peer-reviewed):

7. Aliya Mukanova, Renat Tussupbayev, Agibai Sabitov, Igor Bondarenko, Renata Nemkaeva, Bekbol Aldamzharov, Zhumabay Bakenov / CVD Graphene growth on a surface of liquid gallium, *Materials Today: Proceedings* 4(3) (2017) 4548–4554. CS=0.94.

8. Aliya Mukanova, Arailym Nurpeissova, Assem Zharbossyn, Sung-Soo Kim, Maksym Myronov, Zhumabay Bakenov, *N*-type doped amorphous Si thin film on a surface of rough current collector as an anode for Li-ion batteries, *Materials Today: Proceedings* 5(11)1 (2018) 22759-22763. CS=0.94.

International conferences:

1. A. Mukanova, M. Myronov, G. Colston, D. Batyrbekuly, A. Moldabayeva, A. Molkenova, Zh. Bakenov, Silicon carbide thin film as negative electrode for lithium ion batteries, Abs. #170158, The 20th Topical Meeting of the International Society of Electrochemistry, Buenos Aires, Argentina, 19-22 March, 2017.
2. A. Mukanova, A. Nurpeissova, A. Zharbossyn, A. Molkenova, Z. Bakenov, Si thin film on graphene coated Ni foam as anode for Li-ion batteries, Abs. #FCPJ3 Strasbourg, France, May 22-26, 2017.
3. A. Mukanova, G. Colston, D. Batyrbekuly, A. Molkenova, A. Nurpeissova, M. Myronov, Z.Bakenov, “3C-SiC thin film as negative electrode for Li-ion batteries”, Abs. #GKT2M, Strasbourg, France, May 22- 26, 2017.

4. A. Mentbayeva, A. Mukanova, A. Nurpeissova, A. Urazbayev, Z. Bakenov, *N*-type Amorphous Silicon Thin Film on 3D Current Collector as Negative Electrode for Li-ion Batteries, Abs.#170740, 68th Annual Meeting of the International Society of Electrochemistry in Providence, RI, USA, August 27 – September 1, 2017.
5. A. Mukanova, A. Nurpeissova, S.-S.Kim, M. Myronov, Z. Bakenov , *N*-type doped amorphous Si thin film on porous Cu current collector as anode for Li-ion batteries, Abs. #2G25 58-th Battery Symposium Japan, Fukuoka, Japan, November 14-17, 2017.
6. A. Mukanova, A. Serikkazyeva, A. Nurpeissova, S.-S.Kim, M. Myronov, Z. Bakenov Astana, Kazakhstan, *In situ* Study of Silico*n*-Based Thin Film Anodes for Lithium Ion Batteryю, the 6th INESS-2018, Astana, Kazakhstan, August, 8-10, 2018.
7. A. Mukanova, A. Nurpeissova, S.-S.Kim, M. Myronov, Z. Bakenov, "Si thin film on 3D current collector as an anode for lithium ion microbattery", European Material Research Society, Warsaw, Poland, September 17-20, 2018
8. A. Mukanova, A. Serikkazyeva, A. Nurpeissova, S.-S.Kim, M. Myronov, Z. Bakenov, "Study of Silicon-based thin film on a porous substrate as an anode for lithium-ion battery", NU Research Day, October 18, Astana, Kazakhstan
9. A. Mukanova, A. Nurpeissova, S.-S.Kim, M. Myronov, Z. Bakenov , "Design of silicon-graphene thin film as an anode for lithium ion battery", Abs. #1F21, 59th Battery Symposium Japan, November 27-29.Osaka, Japan.

1.6 Thesis overview

Chapter 1 (Introduction) presents the research motivation, basic background regarding the history of LIB technology and its operation as well as the information about the reasons of the choice of investigated materials, and their basic properties. This section outlines the rationale, objectives, and importance of this work. Along

with this, it describes the goals of the work and provides brief synopses of each chapter of this thesis.

In Chapter 2, the literature review on Si-based thin film anodes history and their current status are discussed in order to provide the detailed description of the anode materials and benefits of using them with the thin film structure. Besides, the information on solid-state electrolytes used with Si-based thin film anodes and methods of thin film deposition are presented in this chapter as well.

Chapter 3 focuses on the general experimental synthesis methods and procedures, features of battery structure and assembling, characterization techniques for physical and electrochemical properties, and equipment used.

Chapter 4 presents the experimental results with a discussion of the research results obtained for 3C-SiC thin film investigated as an anode for LIBs, including the characterization data of structure, “single” particle measurements, thermal annealing with lithium, and electrochemical test results.

Chapter 5 summarized the results on preparation of the current collectors for Si thin film deposition. The details of porous substrate preparation and graphene growth on liquid and solid substrates are described.

Chapter 6 comprises the data on the development of 3D Si thin film anode, the results of characterization and electrochemical tests.

Finally, the entire thesis is summarized in Chapter 7. All new data obtained for the investigated Si-based thin film anodes are summarized along with their brief discussion. Conclusions and recommendations for future work are presented there as well.

2 LITERATURE REVIEW

2.1 General information

Si has come to the forefront candidate among other anode materials suitable for LIBs [21]. It has been already mentioned above, that the interest of scientists is caused by the significant theoretical specific capacity of 4200 mAh g^{-1} achievable at the highest lithiated phase of Si at elevated temperatures, theoretical volumetric capacity of 9786 mAh cm^{-3}, comparatively low discharge potential of 0.4 V *vs.* Li/Li^+ (here and further all potentials are given *vs.* Li/Li^+ if not specified differently), low cost and safety [22–24]. However, an alloying nature of Si lithiation, which results in the high electrical capacity, is inevitably accompanied by undesirable volume expansion. The latter calls strain stress arising in the Si material bulk that leads to its mechanical degradation, pulverization, and electrical contact loss resulting in capacity loss and even safety issues (see Fig. 2a). In addition, the solid electrolyte interphase (SEI) layer, that usually forms on Si anode surface at the first lithiation, becomes very thick upon cycling and impedes Li^+ ions insertion/extraction resulting also in the capacity fade [25]. Fig. 2b shows the schematic view of SEI layer on Si before and after cycling. Another problem of Si is a low conductivity that limits the mobility of electrons which sometimes cannot reach the opposite terminal as shown schematically in Fig. 2c.

Amorphous and crystalline Si (a-Si and c-Si) can be both used as anode materials. However, the crystalline structure has been reported to be inactive until becoming amorphous after the first alloying with Li^+ ions. One of the first clarifying works on c-Si was carried using X-ray diffraction where it was determined its conversion to a partially lithiated a-Si during the first discharge, followed by a sudden crystallization of a-Si into $Li_{15}Si_4$ below 50 mV, which is the fully lithiated phase [26]. This phase is associated with high internal stresses with particle cracking, poor electrical contact, and capacity fading. The authors suggested restricting cycling in the ranges that are above 50 mV. The a-Si showed the higher initial reversible

specific capacity of 2500 mAh g^{-1}, meanwhile, nanocrystalline Si exhibited a reversible capacity of 1000 mAh g^{-1} that was explained by the fact that c-Si has a slow activation rate via the transformation of the material from a crystalline to an amorphous phase [27]. In addition, c-Si provides fewer pathways for Li^+ ions insertion and possesses nonuniform expansion in contrast with a-Si. Therefore, the amorphous phase of Si is able to provide a higher specific capacity and longer cycle life than c-Si [9,25,28,29].

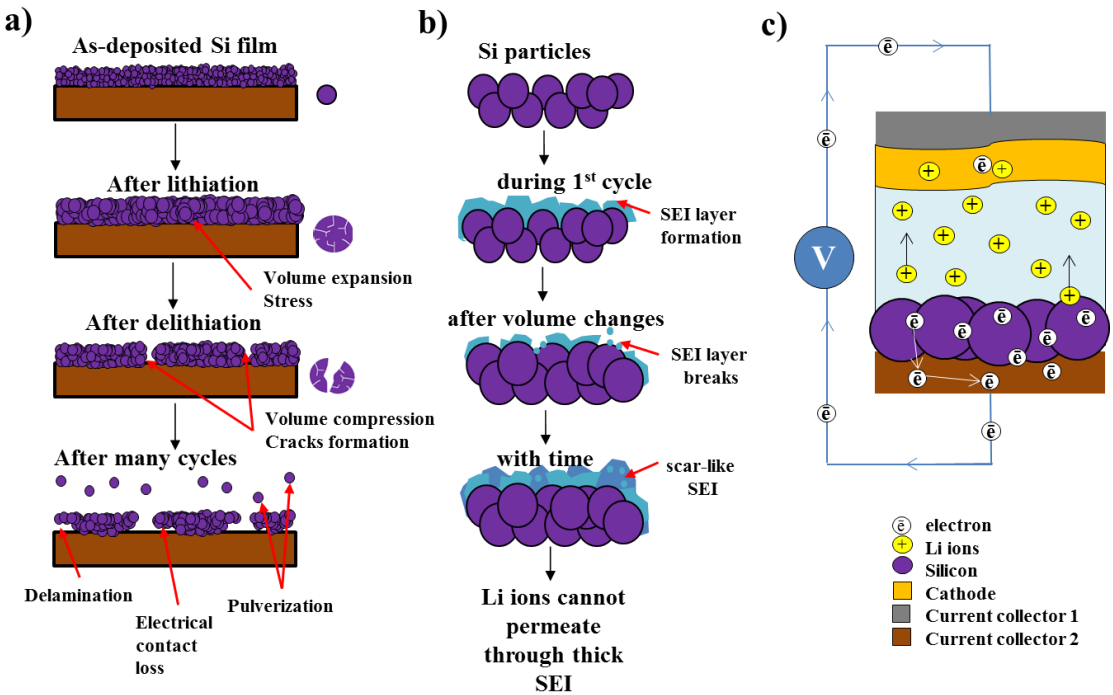

Fig. 2 The problems of Si thin film anodes during operation in LIBs.

Moving from macro- to nanoscale structures can result in the improvement of Si-based anodes. Many researchers have proven that nanosized Si particles are exposed to less degradation due to high surface energy as well as provide more active sites due to the high surface area [30]. Various strategies have been used to improve capacity retention [23, 29]. As mentioned above in §1.3, Si in the shape of a thin film is a promising development direction in the field of LIMBs technology

[2,11]. The disadvantages of Si thin film, such as fast material degradation and low electrical conductivity have an opportunity to be effectively solved at the nanoscale.

During the last two decades, a growing number of research works have been devoted to designing Si thin film anode for the future applications [13,32]; however, the problems with volume variation and rapid capacity fading still demand a practical solution. Researchers have investigated Si-based thin film performance depending on various properties and parameters such as phase (amorphous, crystalline), film thickness, substrate surface condition, Si microstructure and composition, doping, voltage range, electrolyte type, and its composition and other characteristics.

2.2 Lithiation mechanism and stresses in Si thin film

In general, the lithiation process of Si thin films, investigated with the help of conventional electrochemical testing methods and advanced *in situ* optical and structural techniques is similar to that determined for other types of the Si electrode material. The electrochemical reactions in a cell start from SEI formation on the surface of Si film that usually occurs around 0.4 – 0.5 V at the first lithiation. An alloying mechanism in Si thin films has been found to have a stepwise behavior: lithiation reaction onset with LiSi formation at a potential of ~0.4 V and further lithiation with formation of $Li_{1.7}Si$ at the potential of approximately 0.3 V, $Li_{3.25}Si$ at around 0.2 V, Li_xSi (x=3.75, 4.2, 4.4) at the potentials lower than 0.1 V [8, 32–37]. However, the lithiated regions can form in Si thin films differently. Fig. 3 schematically shows the highly lithiated phase between Si and Cu current collector, non-lithiated Si regions, and fast-diffusion paths filled by Li^+ ions formed at the beginning of the lithiation induced by Si deposition defects. Supposedly, Li^+ insertion can be originated by two sides: from an electrolyte and from a fast diffusion path in a direction parallel to the current collector [36].

The apparent coefficients of Li^+ ions diffusion in Si thin films, evaluated by several researchers, are summarized in Table 1 below. According to the data reported in works [38–40], it can be supposed that the coefficient value increases with the

thickness of the film. Besides, it was found that the effect of ionic diffusivity on the cell performance is insignificant at low C-rates and becomes remarkable with the higher C-rates (>C/10), so that, the Li^+ ion capacity of the electrode drops faster for low diffusion coefficients rather than for the high ones. Moreover, the effect of standard rate constant was also observed and, in this case, the low values of diffusion coefficient resulted in the adverse effect on the capacities even at the low C-rates [42]. Li^+ ion permeation through thin Li_xSi layers in a multilayer structure between isotopically modulated $LiNbO_3$ layers, serving as tracer reservoirs, was investigated using neutron reflectometry with rapid thermal annealing instruments. It was found that Li^+ ions permeability with x=0.1 at 255 °C was $P = (3.3\pm0.9)\cdot10^{-21}$ m^2s^{-1} which is identical to that for pure a-Si. Authors suggested that diffusion more likely occurs in pure a-Si domains rather than along the Li-Si-rich percolation paths [43].

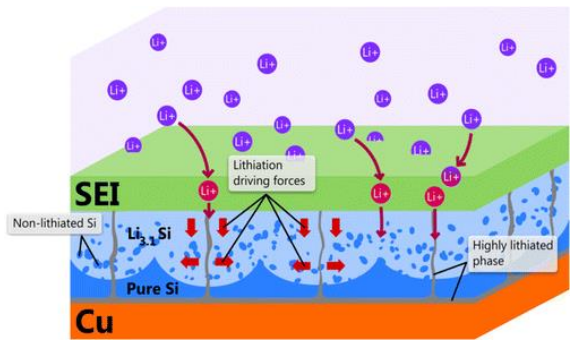

Fig. 3 Schematic view of lithiation mechanism in Si thin film [36].

The stresses in thin film accompanying lithiation are going through sequential steps depending on the Li_xSi alloying level: slight increase of compressive stress (0.3 V), high stresses (0.3 – 0.1 V) and large stresses because of three-four time volume expansion at potential of around 0 V. Consequently, cutting off the low voltage to 0.1 V was suggested in order to improve the cyclability of the a-Si film [44]. The multi-scale model developed for the Si electrochemical and mechanical behavior prediction showed that the compressive stress induced by the volumetric strain enlarges the migration energy barrier, thus causing accumulation of Li^+ near

the thin film surface, which results in a potential drop. Though, with further lithiation, the mixing enthalpy increases the chemical potential leading to uniform Li^+ concentration profile [45]. Another attempt to simulate Si thin film mechanical behavior during Li^+ ions insertion and extraction showed that the stresses appeared in film and substrate during a huge volume changes of Si play a crucial role in mechanical fracture and delamination of Si film leading to electrode failure [47–50]. The analysis of relative volume change for lithiation of 40 and 140 nm a-Si thin films made by *in operando* neutron reflectometry revealed the linear increase in volume as a function of lithiation time and lithium content independent of current density and the initial film thickness [50]. Although, the SEI formation may contribute up to 60% of the electrode volume changes [51], no effect of Si thin film anode thickness was noticed on the thickness of SEI layer. The SEI layer growth, together with Li atoms trapping in the bulk of electrode can limit the Li^+ ionic transport [52].

Table 1 – Summary of Li^+ ions diffusion coefficients for Si thin films.

Name	Thickness, nm	Diffusion coefficient, cm^2/s	Ref.
Si undoped (CVD)	50 – 14 000	$10^{-10} – 10^{-13}$	[39]
a-Si *n*-type (MS)	275	$(1.47 – 2.16)\cdot10^{-9}$	[38]
a-Si:H (GD)	250 – 700	$4\cdot10^{-9} – 10^{-13}$	[40,41]
a-Si (PLD)	120	10^{-13}	[53]
Si fullerene coated	NA	$\sim 4\times10^{-9}$	[54]

2.3 Pure Si thin film anodes

Bourderau, Brousse, and Schleich made the first steps in the development of Si thin film anodes for LIBs [28], though, their initial results demonstrated poor performance of the anode resulted in only 20% capacity retention after 20 cycles. It has been observed later that the cutting the low voltage limit to 0.2 V can significantly affect capacity retention of a-Si thin film improving its cycling performance. However, at the same, a practical capacity that can be delivered at chosen potential range constituted only 400 mAh g^{-1} during 400 cycles [54, 55].

The first deep research of Si thin film was done by Maranchi et al. [9]. Reprinted Fig. 4 shows the cross view of as-deposited thin film and its SEM top image after cycling. The dependency of cyclability and reversible capacity on the film thickness was reported. Significant degradation of the a-Si thin film was noticed by SEM (see Fig. 4b). The islands occurred after the 1st cycle and the gaps between tended to expand with time. The formation of islands is supposedly caused by plastic deformation of the Cu foil serving as a substrate. Electrochemical volume expansion/contraction induced incremental plastic strain (ratcheting) results in widening gaps between islands during cycling. Delamination of the compressively stressed film from Cu has resulted from the interface imperfection. TEM and EDX analysis showed that atomic intermixing has occurred between the film and substrate, with the interfacial region expanding from 26 nm (as-deposited) to 275 nm (after 30 cycles). The possible nucleation of a lithium copper silicide (Cu_2LiSi) crystalline phase weakens the interfacial region between Si and Cu, leading to the loss of electrical contact [57].

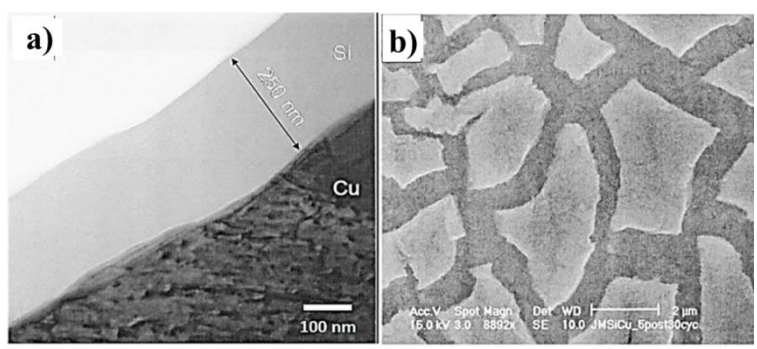

Fig. 4 (a) Cross-sectional TEM bright field image of as-deposited 250 nm Si film on Cu; (b) SEM morphology of Si film on Cu after 30th charge at a C/2.5 rate [9].

The regularity that the decrease of Si thin film thickness positively affects the cyclability has been observed later by numerous experimental works and confirmed by computational works as well [40, 57–61]. The best performance was reported by Ohara et al. for the 50 nm thick Si film that retained a specific capacity of around 3100 mAh g^{-1} after 1000 cycles at 12 C rate with a coulombic efficiency of 100% [17,

62, 63]. In addition, in the same work the doping effect has been investigated (intrinsic, *p*-type and *n*-type), where *n*-type doped Si showed the better electrochemical performance due to higher electrical conductivity and reduced charge transfer resistance on the surface of the doped Si electrodes [65]. However, the performance deteriorated in the full-cell tests, and the *n*-type doped 100 nm a-Si thin film coupled with lithium cobalt oxide ($LiCoO_2$) cathode exhibited only 57% of initial capacity in the 30th cycle (~ 1100 mAh g^{-1}) [66]. Another full cell with the 330 nm thick a-Si thin film and carbon(C)-coated lithium iron phosphate ($LiFePO_4$) cathode delivered a discharge capacity of 120 mAh g^{-1} in the 100th cycle [67].

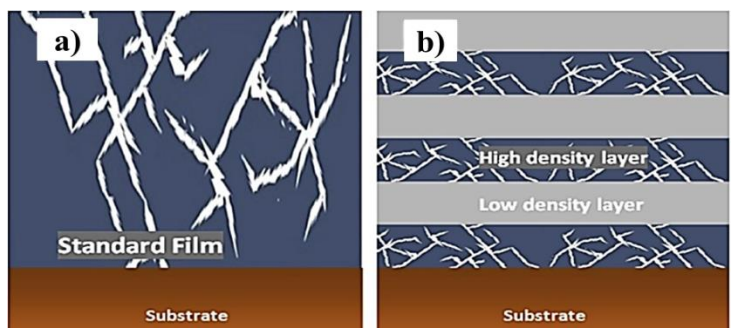

Fig. 5 Demonstration of the crack propagation in (a) standard high density Si thin films and (b) density modulated multilayer Si thin films [68].

Modification of substrate surface prior to Si film deposition was found to be crucial for attaining prolonged cycling stability. Roughening the surface of Cu foil with sandpaper in order to expand the contact area with deposited a-Si film, helped the film to accommodate the volume changes [67, 68]. Etching a substrate in $FeCl_3$ was proposed with the same goal and showed an improved capacity even for the thicker Si thin film (1 μm, 3.6 μm) [17, 69]. Another original route, a treatment of a substrate by plasma immersion lanthanum ion implantation, afforded Si thin film anode to achieve capacity retention of 93% at 80th cycle [59]. Electrodepositing used to get the rough surface of Cu foil was intended to improve the performance of a 6 μm *n*-type doped a-Si, however, the anode demonstrated capacity retention of 42% after the 1st discharge only [72]. Annealing the as-prepared anodes at 300 °C prior to

battery cell assembly was also reported to improve adhesion strength between Si and Cu, and, consequently, achieve better electrochemical performance [38].

Another successful strategy to overcome the material degradation from repetitive volume changes were offered via the design of the density modulated multilayer *p*-type doped a-Si thin film anodes (see Fig. 5). The low dense layers served as a buffer for expansion between the high dense layers preventing the crack propagation in the film [68,73].

In order to dynamically simulate the cracking in the electrode materials during delithiation, the simulation based on spring-block model, usually used in the mechanics, was applied [62]. It has been demonstrated that the capacity fading due to the crack formation during lithiation/delithiation can be reduced by optimization of the characteristic size of the thin film and average cracked area (island surface area). Two routes can be employed to design the stable anode: patterning electrode with the pattern size smaller than the average cracked size for specific film thickness and mentioned above reducing a film thickness to less than the critical thickness (depending on a thickness of the current collector) [62]. The various patterns and structures were employed to improve the electrochemical properties. The lozenge-shaped tiles (Fig. 6a,b,c), which was obtained by masking a substrate during deposition, allowed to retain 91% of capacity after 100 cycles owing to the excellent stress suppression effect during lithiation/delithiation due to the space between Si tiles (Fig. 7), a good adhesion and the enhanced mechanical stability of patterned Si thin film anode [74,75]. Besides, the decrease of pattern's size (7–10 μm) showed the higher structural stability of the film without its delamination from a substrate [76]. The design of the anode system with the trenches prepared by etching an ink-coated Cu foil and covered by Si thin film, shown in Fig. 8, also resulted in the improvement of electrochemical performance and exhibited 60% capacity retention after 100 cycles [77,78]. Fig. 9a,b illustrates a structure externally similar to the previous, but different in its concept. The developed anode system with Si ribbons on the soft elastomeric substrate (poly(dimethylsiloxane), PDMS) had the stretchable

nature that helped to levitate strain stress in Si during the volume changes at Li^+ ions extraction/insertion [79].

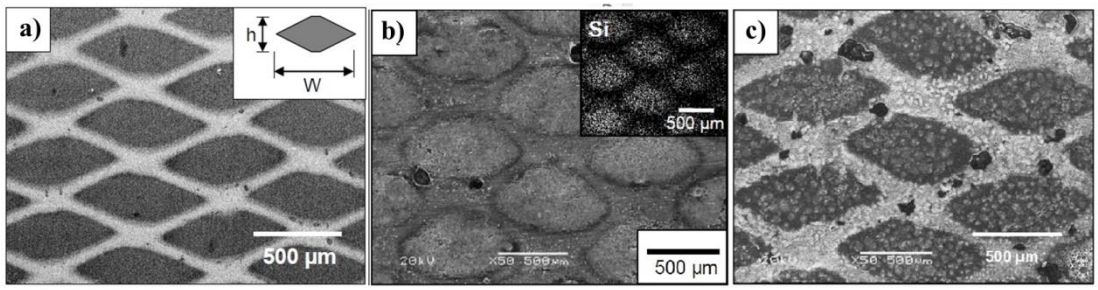

Fig. 6 SEM images of Si thin film with lozenge-patterned holes (a) flat before cycling and (b) flat after 10 cycles[74], (c) rough after 50 cycles [75].

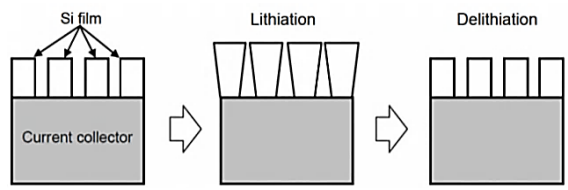

Fig. 7 Schematic diagrams of the structural change in patterned Si film electrodes during the charge-discharge (lithiation/delithiation) process [75].

The investigation and comparison of the planar and shaped Si nanostructures clearly demonstrated the priority of a three dimensional (3D) structured electrode, which was able to achieve high surface area, increased current density and provide an improved mechanical stability. For example, the low densely packed nanopillars, prepared from the *n*-type monolithic doped a-Si by etching, showed an excellent cycling performance during 50 cycles with almost no capacity loss [61]. A honeycomb-structure of a P-doped a-Si (Fig. 10a) was designed using lithography technique for etching. The Fig. 10b shows the recorded voltage profile of prepared anode with the inserts of SEM images corresponding to various lithiation contents (in %). The mechanical deformation of honeycomb walls resulted from the occurring internal stress during lithiation and tended to gradual conversion back during delithiation to the nearly original hexagonal structure upon 50 cycles [80]. Si

nanowires perform superior electrochemical properties and long cycle life attributed to the high porosity and electron conductivity of the anode [80–82]. Mathematical model simulation confirmed that the porosity and larger pore size provide the stabilized structure during charge/discharge process [83].

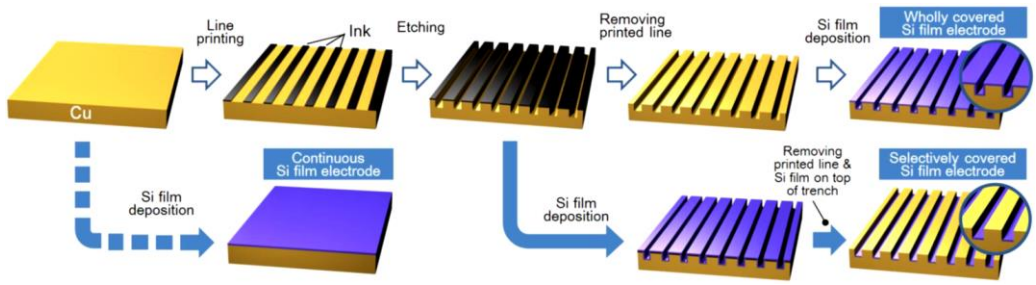

Fig. 8 The surface morphology of continuous, wholly covered Si thin film electrode and selectively covered Si thin film electrode [77].

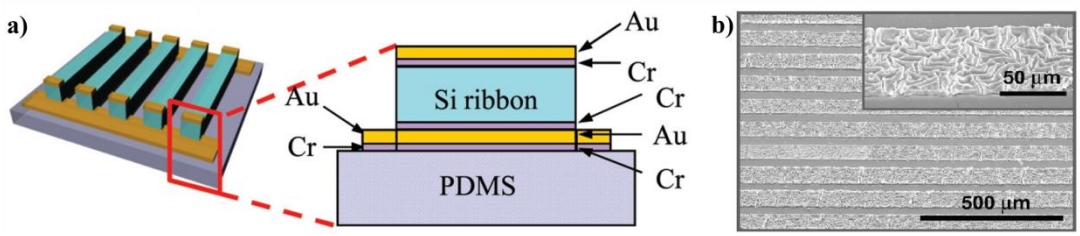

Fig. 9 (a) Si anode on poly(dimethylsiloxane) PDMS substrate, (b) SEM images show the buckled Si after lithiation, after six cycles charge/discharge under the charge rate of 1C[79].

The use of a 3D structured substrate for thin film deposition was demonstrated as one of the most effective ways to achieve a stable Si anode cycling. The strengthened conductive framework, made from synthesized Cu nanowires with the enhanced electrical connection by ‘tight-contact’ deposition was applied as a substrate for a-Si film. The capacity retention constituted around 90% after 60 cycles [84]. Si thin film, deposited on a Cu foam [85] and porous Cu foil obtained by etching in an ammonia solution [86], resulted in a high mass loading and very good cycling stability. The connected conductive network allows the Si film to facilitate the charge collection and avoids severe pulverization and cracking of the material

caused by the volume change. Another 3D current collector – a cobalt nanosheet arrays (Fig. 11), helped to hold 82% of the initial reversible capacity delivered by Si thin film after 100 cycles [87].

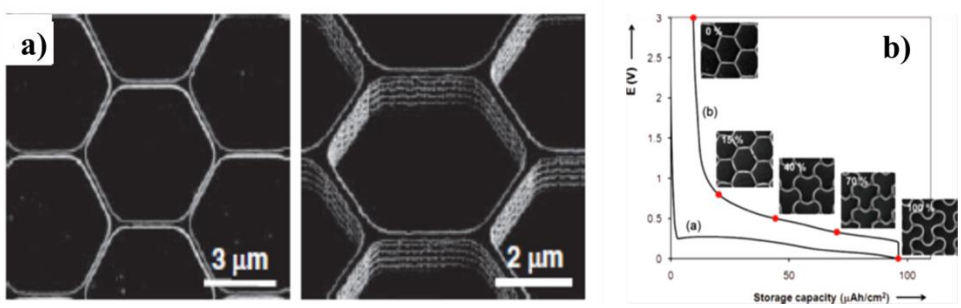

Fig. 10 (a) SEM top and tilted view photographs of as-prepared Si honeycombs, (b) morphological changes of the Si honeycomb structure [80].

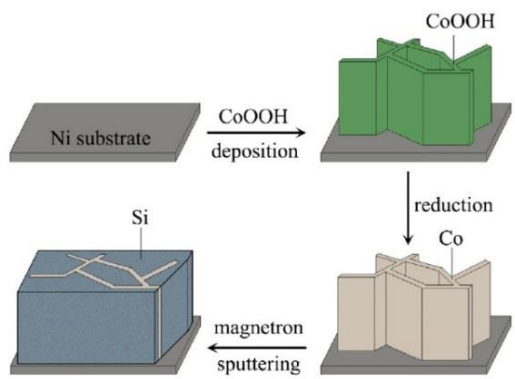

Fig. 11 Schematic diagram of the preparation process of cobalt nanosheet arrays supported Si film [87].

Fig. 12a,b shows SEM top-view of the Si anode on Tobacco mosaic virus covered by nickel (TMV1sys/Ni) and TEM image of a single Si coated conductive nanowire, respectively. In order to reduce the irreversible capacity, the authors carried out annealing at 350 °C and coating of the electrode by polyacrylonitrile (PAN) with consequent carbonization at 500 °C in Ar. The prepared 3D Si electrode demonstrated a reversible capacity of 2300 mAh g^{-1} and a capacity of 1200 mAh g^{-1} at the 173th cycle. In spite of the capacity fading, the 3D patterned Si film electrode showed a good rate capability with a capacity decrease from 1818 to 985 mAh g^{-1} at the C-rate increase from 0.25 C to 4 C [88].

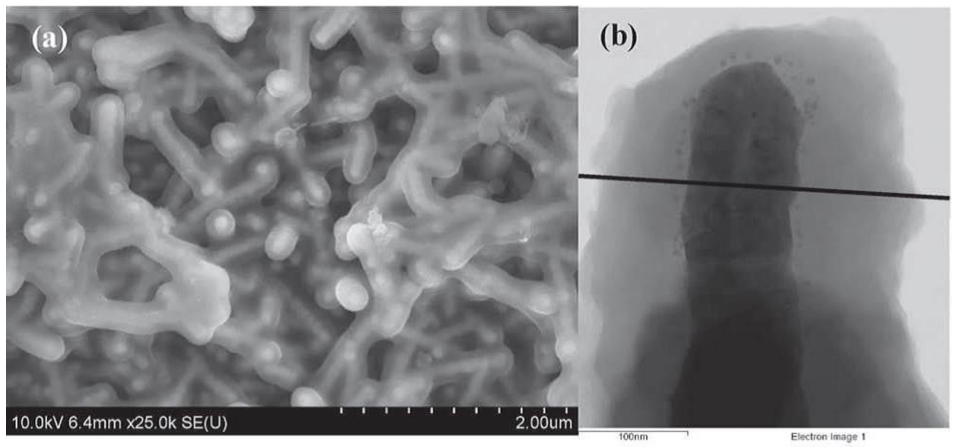

Fig. 12 (a) SEM image of the prepared 3D Si anode and (b) TEM image of a single nickel-Si core-shell nanowire [88].

2.4 Si-based thin film composites and alloys

Development of Si-based composites and alloys is a predictable approach towards a stable electrode with a specific capacity higher than that of conventional graphite anode. Similar to a micro-scale powder-based electrode technology, a mixture of materials can be easily employed at the nanoscale. For last decade, there were many studies on the combinations of active Si with various components like [88–90], Mo [92], Fe [92, 93], Al [95], B [96], Y [97], Ti [98], as well as electrochemically active carbon nanomaterials.

The formation of metal silicide (Si-Mo, Si-Cu, Si-B, Si-Ti) film was reported to reduce electrical resistance and improve the mechanical properties due to the existence of additional chemical bonding [88–91, 95, 98, 99]. The coatings such as Cu [101], Cu_2O [102], C [102–105], silicon nitride (SiN) [107] on the surface of Si thin film are used as a protecting top layer, which in contact with the electrolyte resulted in the mechanical stability with forming stable SEI as well as an enhanced access for the Li^+ ions diffusion, improved surface electronic conductivity and suppression of an electrical contact loss. For example, a-Si thin film with carbon coating, containing some amount of Cu particles (Fig. 13), did not show a trace of damage after 1000 cycles [106]. Si thin film coated by the 100 nm layer of fullerene

showed the remarkable improvement of the electrochemical impedance of thin film [108]. SiN-coated Si anode demonstrated an enhanced electrochemical performance with a higher capacity due to the formation of a Li_3N film, which resulted in increased ionic conductivity. The low charge transfer resistance in such layers allowed the cycles at high rates up to 10 C. Besides, the thinner layer of SiN_x was observed to be more effective since the inert nature of SiN may prevent Li^+ ions transport and reduce the capacity [107].

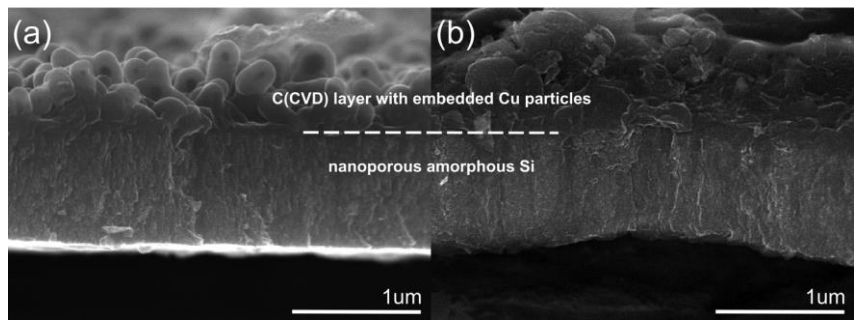

Fig. 13 SEM image of sample Si+C (a) before and (b) after cycling (compare to Fig. 2(f)). The C layer covers the porous amorphous Si (1 mm thick) in a conformal way, without breaking the film continuity [106].

Multilayer structured anode with Si thin film and Fe [69, 70], Al [95], Y [97], Ti [98], Ta [109], C [42,103,104,110] interlayers, which can act as conductive components as well as mechanical buffers during volume changes, illustrated an enhanced cycle life of the electrode. In contrast with planar multilayer electrodes, 3D nanostructured multilayer Si-Al film (Fig. 14) [95], the 3D system Si-Cu-Ti thin film with Cu_3Si nanowires [111], Si on TiO_2 nanotubes [112] could effectively accommodate the volume changes and improve the electronic conductivity, enhancing the electrochemical performance. Multilayered Au-Ti/Si/LiPON/SnO_2 anode system prepared by sputtering demonstrated a slightly alternating capacity; however, no visible capacity loss was observed during 200 cycles. This was explained by the LiPON/SnO_2 layer acting as a stable porous SEI layer [113]. The challenge for multilayered Si-based thin film anodes is that the thickness, density and amount of layers should be optimized accurately to provide enough mass of active Si

and positive influence on Li^+ ions diffusion kinetic property and coulombic efficiency.

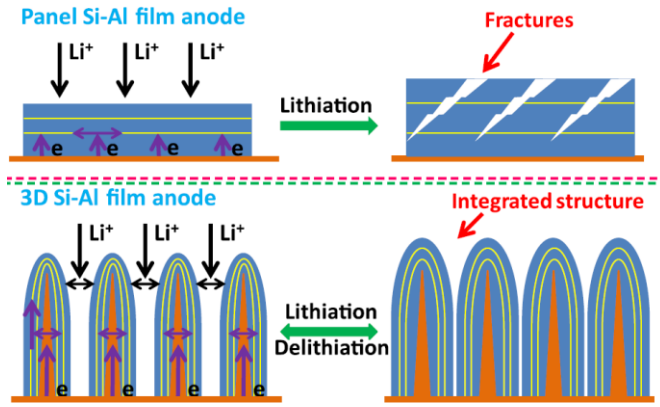

Fig. 14 Schematic illustration of the mechanism of 3D Si-Al electrode for improving the electrochemical performance [95].

Similarly to the conventional Si/C-based composite anodes for LIBs, the incorporation of carbon-based materials into Si thin film is a widespread concept to construct high-performance electrodes [44, 104, 113–117]. Taking into account that C materials can be intercalating by Li^+ ions, they are able to contribute to the total capacity of the thin film significantly. Graphene (GF) and carbon nanotubes (CNT) can reach the capacity as high as two times more than conventional graphite [118–120]. Moreover, pure graphene-based anodes were reported to achieve the capacity up to 1116 mAh g^{-1} when Li^+ ions occupy the adjacent sites of graphene sheets and where LiC_2 intercalates are formed [121]. In addition, the SEI layer on carbon nanomaterial is more stable compared to that on pure Si, and therefore, the combination of Si and C can be beneficial and provide high capacity and energy. For example, multilayer graphene deposited on the nickel foam, acting as a substrate for Si thin film, displayed a stable capacity of ~2400 mAh g^{-1} with the capacity retention of 75% after 45 cycles [114]. The effect of graphene on the cycling stability improvement was observed due to the enhanced adhesion at the Si-graphene interface [114,116,118].

2.4.1 SiC thin film

Silicon carbide (SiC) is an amazing material well-known for its resistance to high-temperatures, radiation, corrosive, abrasive and erosive media [122,123]. SiC is widely used in the electronics industry and draws significant attention as an emerging energy storage technology due to its outstanding thermal and physical properties [124,125]. For a long time SiC was considered inert towards Li^+ ions; however, there are some works that report SiC as a very promising anode material with the ability to store Li^+ ions (a theoretical capacity is 2638 mAh g^{-1}) [15,126–128]. In contrast with Si anode, which suffers from rapid degradation due to the volume changes upon lithiation/delithiation cycles, a cubic polytype SiC (3C-SiC) can serve as a host matrix for Li^+ ions intercalation, which is able to reduce the detrimental impact of expansion/contraction scenario [16]. Shiratani et al. showed that SiC thin film having 4000 mAh g^{-1} in the first cycle can save 85% of the initial capacity up to 10^{th} cycle [126]. However, the structural studies of SiC thin film were not shown in his paper. Introduction of the dopants to thin film surface layer is a crucial technique to improve electrical properties of the 3C-SiC/Si anode, which is extremely important to enable high rate Li^+ ions diffusion and charge transfer processes in the electrode [18, 128].

2.5 Electrolytes for Si thin film anodes

2.5.1 Liquid electrolytes

The SEI layer formation plays a key role in the cycle life of the Si electrode. The morphology of the SEI layer is important for the long cycle life and can be dependent on the anode surface condition, especially the Si particle size. In case of remarkable expansion of micro-sized Si particles, the extensive fractures are observed on the SEI layer surface. These fractures overgrow with the newly occurring electrolyte decomposition on the Si surface, forming a ‘scar tissue’ like structure which delays the Li^+ ion transport into anode resulting in deteriorating of rate capability and capacity decrease at high rates [25,130]. On the other hand, the

uncontrollable growth of SEI layer uses up large amounts of Li^+ ions and electrolyte and leads to an increase in the cell resistance, thus resulting in a capacity fade and an unstable electrochemical performance [131]. The initial capacity loss due to SEI layer formation directly relates to the initial content of oxygen on the Si film surface. The oxygen atoms react with the liquid electrolyte and become a part of the molecules constituting the SEI layer. Removal the oxide before battery assembling leads to the decrease of the irreversible capacity as well as an enhancement of electrode cycling stability [61].

SEI layer on Si is usually a compound of several chemical components emerging during liquid electrolyte decomposition on the Si-based electrode surface. Fig. 15a,b shows the molecular composition of the SEI layer forming in case of the liquid electrolyte 1 M lithium hexafluorophosphate (LPF_6) in ethylene carbonate (EC) : diethyl carbonate (DEC) (1:1, v/v) at various charged and discharged states determined by high-resolution X-ray photoelectron spectroscopy (XPS) analysis. It can be seen in Fig. 15a that Si signal disappeared at the first charge around 0.1 V, meaning the SEI layer thickness becomes thicker than XPS penetration depth (~10 nm). In course of time, Li carbonate tends to prevail as the amount of the rest products decreases [132].

The comparison of the lithium bis(oxalato) borate (LiBOB) and $LiPF_6$ electrolytes with the same solvent EC:DEC (3:7, v/v) showed the remarkable improvement of discharge capacity retention in case of the first electrolyte. This was ascribed to the formation of the SEI layer with a less-porous structure. The 1 M LiBOB electrolyte was able to increase the conductivity of the a-Si electrode by approximately 3.5 orders of magnitude, which attributed to the formation of LiSi alloy, possessing metallic properties [133]. The investigation of the additive-free 1 M lithium bis(trifluoromethylsulphonyl)imide (LiTFSI) in N-methyl, N-propylpiperidinium bis(trifluoromethanesulfonyl)imide (MPPpTFSI) electrolyte showed that the high anodic stability of this ionic liquid may help to develop the very high energy density system [66].

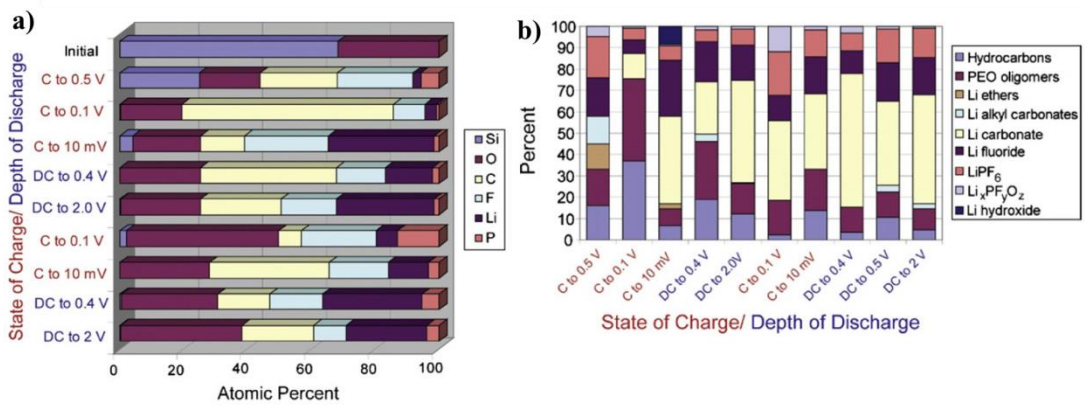

Fig. 15 Molecular species found on the surface of the Si at different potentials as determined from the XPS high-resolution scans [132].

The carbonate additives like fluoroethylene carbonate (FEC), vinylene carbonate (VC) and propylene carbonate (PC) were reported to improve SEI layer morphology. FEC additive (3%) introduced into an EC:DEC (3:7, v/v) electrolyte in 1.3 M $LiPF_6$ is able to improve SEI layer structure making it smooth and more stable that provided the facilitated path to Si and led to the increase of the discharge capacity retention by 20.6% [134]. Similarly, the effect of FEC additive in a 1 M LiPF6 in FEC:dimethyl carbonate (DMC) (1:4, v/v) was studied in the full Li^+ cell composed from a-Si thin film anode and a high voltage lithium nickel manganese oxide ($LiNi_{0.5}Mn_{1.5}O_4$) spinel composite cathode. It was found that FEC resulted in stable cycling of Si/Li cells for more than 1500 cycles. The improved performance was explained by the good passivation of the Si anode surface and effective passivation of the surface of high voltage cathode [135]. In the works [66,101,132], FEC also was found to remarkably improve the long-term cycle performance of Si-based electrodes.

1% VC added into the electrolyte observed to assist the formation of a smooth and uniform SEI layer on Si film, which significantly improved the ionic conductivity, and a 150 nm thick *n*-type doped Si thin film retained 97% of initial capacity value in the 200^{th} cycle [136]. The electrochemical performance of 1M lithium perchlorate ($LiClO_4$) in PC solvent was compared with the same electrolyte

in a mixture of EC:DMC (1:1, v/v), where finally both solvents were found to have identical influence. However, it was recommended to use PC additive due to its low cost and an ability to work at low temperatures [63]. In another research, the combination of 2% VC and 10% FEC in the mixture of 1 M $LiPF_6$ and EC:DEC:ethyl methyl carbonate (EMC) (1:1:1, v/v/v) revealed the improved capacity retention [95]. The effect of the electrolyte composition on the irreversible capacity of the Si electrodes, in particular with PC-based and EC:DEC-based electrolytes, did not reveal a significant difference between them [137].

The effects of trimethoxymethyl silane (TMOS, $CH_3Si[OCH_3]_3$) additive (in 1 M $LiPF_6$ in EC:DEC (1:1, v/v) electrolyte) on SEI layer formation was studied for c-Si thin film electrode. It was detected that TMOS can effectively protect the Si surface, producing a stable SEI layer composed of organics with alkyl carbonate and carboxylic acid metal salt functionalities, and phosphorus and fluorine containing species, leading to stable cycling at 0.1 – 1.5 V vs. Li/Li^+ delivering 2400 mAh g^{-1} over 200 cycles. The authors reported that PF-containing species, obtained on the Si film surface after cycling without using TMOS, are responsible for the inefficient passivation of the Si surface, resulting in a rapid capacity fade [138].

Another study [139] investigated the effect of lithium salt solution electrolyte containing alkoxysilane additives. The significant overpotential growth and an aggravating capacity for the discharge/charge process were attributed to the sedimentation of electrolyte reduction product. Moreover, the additives of alkoxysilane acted as a passivation agent. In general, the presence of such additives prevented the mass accumulation to the Si electrode induced by irreversible electrolyte reductions, thus improving the electrode's cycle life.

2.5.2 Solid state electrolytes used in Si anode-based LIBs

SS electrolytes provide advantages in terms of simplicity of design and operational safety [140–142]. Solid electrolytes were proposed as a route to avoid dendrites formation in lithium batteries and for applications where elevated

temperatures persist [143]. SS electrolytes also can push towards a design of safe nontoxic lithium-ion batteries with improved cycling performance [144,145].

In the case of Si, it is essential to avoid the formation of nonuniform SEI layer and related capacity loss in the first cycle. Therefore, the capacity and cycling stability are expected to be improved. A 3D SS LIBs with 1 μm LiPON as a solid electrolyte (Fig. 16a) and 50 nm Si thin film exhibited the capacity of ~3500 mAh g^{-1} with no decrease upon cycling for 60 cycles unlike the cell with liquid electrolyte ($LiPF_6$ in EC:DEC, $LiClO_4$ in PC) that was assembled for comparison. SEM investigations did not reveal the SEI layer formation in the Si/LiPON interfacial region after cycling (Fig. 16b) [146].

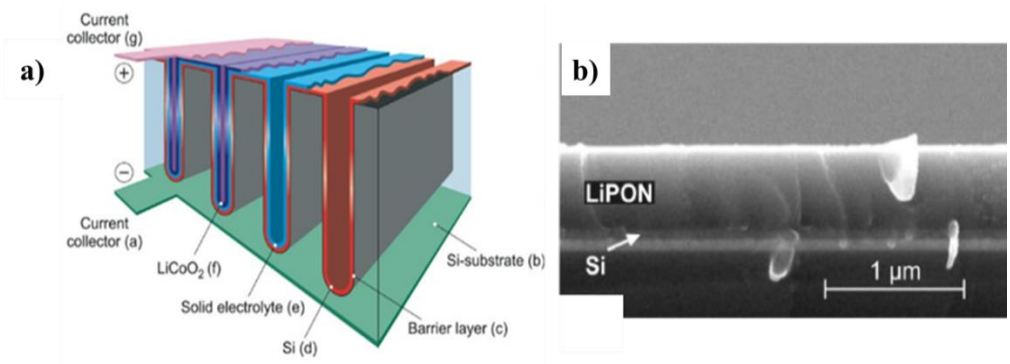

Fig. 16 (a) 3D integrated all-solid-state battery; (b) SEM image of the interface Si/LiPON after cycling [146].

The SS battery cell containing a-Si thin film anode (50–200 nm) with the LiPON electrolyte and a lithiated titanium oxysulfide ($Li_{1.2}TiO_{0.5}S_{2.1}$) cathode is shown in Fig. 17. Initially, testing a-Si thin film anode in a half-cell with solid electrolyte, the authors observed that the formation of $Li_{14}Si_4$ phase differs from that in liquid electrolyte systems, and this final reduction step occurs below 0 V at the low constant current or initiates only after 2 hours floating at 0 V. The test results of designed batteries assembled with the industrial tools and embedded in microelectronic packages demonstrates high cycle life (− 0.006% of capacity per cycle) and ultrafast charge (80% capacity in min) [147]. The incorporation of boron (B) into LiPON electrolyte (LiPONB) led to the enhanced chemical and thermal

stability. The Si thin film electrode with a prepared LiPONB demonstrated the excellent cycle life and coulombic efficiency with almost no loss during 1500 cycles. Besides, no cracks were observed in the film or at the electrode/electrolyte interface by SEM [148]. Investigation of the electrode-electrolyte interfacial region of the microbattery system 600 nm Cu – 50 nm Si – LiPON – $LiCoO_2$ did not reveal any accumulation of Li at the interface between anode and electrolyte, and alteration of electrical properties of Si-Cu layer upon cycling [149].

Fig. 17 FIB/SEM cross-section of a thin film encapsulated LIB comprising the $Li_{1.2}TiO_{0.5}S_{2.1}$/LiPON/Si active layers and titanium current collectors [147].

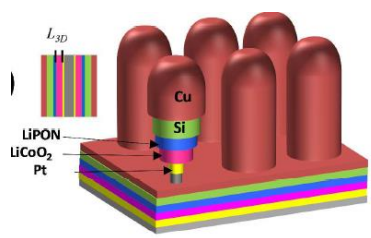

Fig. 18 Schematics of a 3D SSLIB [150].

The 3D all SS LIB with 500 nm thick LiPON electrolyte, shown in Fig. 18, was assembled by deposition of corresponding layers on the designed 3D template. The battery cell demonstrated the poor power performance that was explained by the structural inhomogeneity of the layers, coupled with the low ionic conductivity of SS electrolyte and diffusion rate in the cathode, led to a highly non-uniform internal current density distribution and poor cathode utilization [150].

In fact, there is a challenge with the deposition of SS electrolyte on the electrodes and assembling cell, especially if it is a 3D structure. SS electrolytes

derived by deposition demonstrated the ionic conductivities within 10^{-4} – 10^{-6} S cm^{-2} that is remarkably lower compared with liquid electrolytes [151,152]. Another question is related to the mechanical stress that emerges inevitably in the SS electrolyte when Si volumetric changes occur during the processes of lithiation/delithiation.

2.6 Si thin film preparation techniques

Various techniques have been tried so far for Si deposition such as electrodeposition, chemical vapor deposition, vacuum evaporation, electron beam evaporation, ballistic consolidation, magnetron sputtering, glow discharge, pulsed laser deposition. The preparation method and its conditions have a significant influence on the thin film microstructure, morphology, crystallinity, thin film-substrate interface/interphase purity, density, and other physicochemical properties.

2.6.1 Physical methods

Magnetron sputtering (MS) is related to physical vapor deposition and one of the most widespread processes employed for a thin film manufacturing. In the working chamber of MS, the plasma-derived gas ions accelerate between two electrodes in a low-pressure gas. The ions are directed towards the target surface where atoms of the latter are ejected from the material and flying on the substrate surface [153]. The benefits of MS are the easy control of film density, purity and thickness by varying power type (alternating current (radio frequency) – *rf*, direct current – *dc*), gas pressure, target material, rotation speed and deposition time, as well as an opportunity for the pre-sputtering cleaning of target and the further scale-up of the process. As a result, MS was quickly adapted for Si thin film preparation. A high purity disk-shaped Si is used as a target, and argon gas is used as a working gas. The sputtering power showed a significant effect on the value of irreversible capacity at the first cycle. The comparison of three power value - 30, 60, 85 W performed the initial specific capacity of 4200, 3800, 3060 mAh g^{-1}, respectively. So, the irreversible cycle capacity of anode increases as the power decreases. The reason was

found to be a different Si oxide content, where a larger amount of oxygen incorporated in the film at lower power, and then led to the initial capacity drop due to the elevated amount of Li_2O during SEI formation [61]. Heating of the substrate up to 200 °C is found to strengthen the adhesion at the interface due to the interdiffusion of Si and Cu layers that finally resulted in the improved cyclability of the Si anode [59]. Among the other approaches: a substrate rotation option was added for better thickness uniformity, and deposition of Cr or Cu layer to improve attaching Si film to the substrate [68].

Ion-beam deposition (IBD) is quite similar to MS apart from some differences. There is no bias applied and no plasma occurs between the target and the substrate in IBD. So due to that, conducting and non-conducting targets and substrates and even sensitive substrates can be applied. Finally, IBD operates at a much lower pressure (< 0,013 Pa) than standard MS, so the inclusion of sputter gas atoms in the film is a lesser problem [43,99,132,136,154].

Unlike MS, in *plasma laser deposition* (PLD) technique the laser is used with high power pulses up to ~10^8 W cm^{-2} in order to melt, evaporate and ionize material from the target surface. A highly luminous plasma plume is produced and expanded away towards the substrate, on the surface of which the volatilized material deposits as a thin film [155]. The preparation of amorphous Si thin film by PLD was reported in several works [53,60,104,138]. Different deposition pressures were exploited in order to evaluate the influence of this process parameter on the morphological/electrochemical characteristics of the resulting nanostructures. The sample prepared at lower deposition pressure, having porosity featured by larger average pore size and lower surface area, showed better cycling performance.

Vacuum evaporation (VE) is another effective method to prepare a-Si thin films [19,63,64,71]. Si powder or crushed pieces put in a tungsten heating boat usually serves as a source. Inside a work chamber, kept under a vacuum of around 10^{-4} – 10^{-5} Pa, an electric current is passed on the tungsten boat to heat the Si source

up to a melting point, at which Si evaporates and deposits on the proper set metallic substrate.

Electron beam evaporation (EBE) differs from the previous method only in the way the source is heated – the electron beam gun is applied for this aim. This method was used to prepare monolithic Si films and Si/Fe multilayer thin films in the works [93,94,133,134].

Ballistic consolidation (BC) and *gas-phase condensation* techniques were reported for Si films preparation. In the first process, the Si source was heated in a tungsten basket and evaporated into the gaseous atmosphere. In the gas, the Si atoms were cooled rapidly, and nanocrystals were nucleated as the atoms collide. Moving by Brownian motion in the gas, the nanocrystals formed the agglomerates. The gas was supplied through a nozzle, approaching the sound velocity, and the Si thin film formed from the ballistically consolidated nanocrystals when they hit the substrate at high speed. The atmosphere was a mixture of N_2 + H_2 and the pressure 2.6×10^{-2} Pa. The second process, GC, described in the paper was similar to VE [27].

2.6.2 Chemical methods

Electrodeposition (ED) is a convenient and economically viable method for Si films deposition [156]. ED of Si films is carried out on the basis of conventional ED procedure. The electrolyte usually contents a high purity silicon tetrachloride ($SiCl_4$) in PC solvent. PC provides a good environment for solubilizing the halide salts of silicon due to a high dielectric constant [157]. The electrodeposition technique was used and the effect of different frequencies (0, 500, 1000, 5000 Hz) was studied. The analysis showed that the higher frequencies result in better stability and performance. So, that the Si thin films electrodeposited at 5000 Hz pulse current frequency demonstrated the stable capacity of 805 mAh g^{-1} with a fade ~0.056% capacity loss per cycle upon 500 cycles. However, the high first cycle irreversible loss as the result of the loss of Li^+ ions due to the oxygen presence and the change in mechanical integrity due to volumetric expansion remained as the main problem [85,157–159].

The structure of the electrodeposited Si film may vary from amorphous to a nanocrystalline structure. In contrast with the above methods, ED allows the internal surfaces of complicated 3D structures to be covered easily with a relatively good uniformity [85,88].

Chemical vapor deposition (CVD) [28] and its modifications like reduces pressure CVD (RPCVD) [55] and plasma enhanced (PECVD) [80,89,160,161], are based on a chemical decomposition of Si-containing gas like SiH_4 or disilane (Si_2H_6) at the high temperatures following by the adsorption of the released atoms or molecules on the substrate surface. The main drawbacks of conventional CVD are purity and uniformity of materials that can be successfully solved using RPCVD or PECVD. Reduced pressures mitigate undesirable gas-phase reactions and improve film uniformity across the substrate.

For the Si film anode obtained by PECVD Si thin film anode, the effect of the substrate temperature on the electrochemical characteristics of the anode was observed by Song et al. [89]. It was found that during the deposition on Cu substrate under the elevated temperature above 400 °C, the reaction between Si radicals and diffused Cu ions took place with the formation of Cu silicide particles with the granular shape. The thin film anode exhibited an improved cyclability thanks to the formed phase mitigated a volume change owing to the existence of additional chemical bonding and reduced electrical resistance.

Glow discharge (GD) plasma deposition of Si thin films is a mixed physicochemical process. Plasma is generated when a voltage is applied between two oppositely charged metal electrodes and electric current is passed through a low-pressure gas. The hydrogenated a-Si films (a-Si:H) is obtained by the decomposition of silane (SiH_4) gas in a glow discharge plasma at the high temperatures. The increase of the synthesis temperature has been found to decrease the residual hydrogen content in the films. The density of the material observed to be lower at the lower deposition temperature. The a-Si:H thin films obtained at the higher

temperature (100 °C vs. 250 °C) showed the improved electrochemical performance [40,41,137].

For an ease comparison of the various deposition methods, their advantages and disadvantages are summarized in the Table 2 below.

Table 2 – The advantages and disadvantages of the methods used for the Si thin film deposition

Method	Advantages	Disadvantages	Ref.
MS	High deposition rates, ease of sputtering; High-purity films; High adhesion of films; Excellent coverage of steps and small features; Heat-sensitive substrates.	Nonuniform thickness of films; Ineffective for complicated 3D substrates; Low cost.	[68]
IBD	High purity of film; conducting/non-conducting targets and sensitive substrates can be applied.	High cost.	[43]
PLD	Low temperature; Combinatorial film growth; Exact transfer of complicated materials; Control of growth.	Uneven coverage; Not well suited for large-scale film growth.	[155]
VE	High-purity films; Low cost	Unevenness and inaccurate deposition; Short-term source material; High heat loads within deposition system.	[71]
EBE	Controllable deposition rate; High material utilization efficiency; Structural and morphological control of films.	At low evaporation pressures: line-of-sight deposition process and dissociation of compounds.	[134]
ED	Simplicity; Control of mechanical properties and thickness.	Non-uniform plating; Time consuming; Contamination from solution; Disposal of the electroplating solution.	[156]
CVD	Relatively low operating cost, no vacuum needed.	Poor purity and uniformity of deposited layer; Gas flow dynamics hard to control	[28]
RPCVD	Lower reaction temperatures; Good step coverage and uniformity; Less dependence on gas flow dynamics	Increased cost; Possible downstream depletion in horizontal design.	[55]
PECVD	Better uniformity.	More process variables to control; High cost.	[89]
GD	Simple; Easy to obtain stoichiometric alloys and compounds coatings; Low temperature; High uniformity over complex and large areas	Relatively low kinetic energy; Deep recesses.	[137]

2.6.3 Summary

Thus, in this dissertation, two main directions to design and study of Si-based materials have been chosen. The epitaxial 3C-SiC will be studied as a novel material in order to deeply investigate the possibility of its electrochemical interaction with Li^+ ions and estimation of the achievable capacity. The high crystallinity of 3C-SiC material can help to avoid/decrease possible trapping of Li ions into defects usually existing in a polycrystalline material.

The second object of research is the pure amorphous Si thin film which will be deposited on a metallic substrate. On the base of the literature review, the most optimal route to accommodate volume changes and decrease the material degradation is the deposition Si thin film on 3D substrate. Therefore, 3D substrate will be prepared and Si with the thickness of no more than 400 nm will be deposited. In addition, the incorporation of dopants will improve electrochemical performance. Besides, one of the most promising electrolyte additives, (vinylene carbonate), will be used for stabilization of SEI layer. Finally, the design of a novel anode, Si film on graphene coated 3D metallic network will be performed and the anode will be electrochemically assessed.

Considering all preparation methods, MS is more preferable for the preparation of amorphous Si thin film due to its simplicity and proven methodology. For the preparation of the monocrystalline 3C-SiC, the CVD at a reduced pressure has been chosen because it is more efficient and a low-cost route to synthesize the film with the higher crystallinity and uniformity

3 GENERAL EXPERIMENTAL METHODS

3.1 Characterization and equipment

This chapter describes the common methodology for the physical and electrochemical characterization of the electrode materials under the study, including cell assembling procedure, and equipment used. Various characterization methods were used to determine the physicochemical properties of the investigated materials.

Electrochemical testing. BioLogic Science Instruments (France), Neware Technology Ltd. (China), BT-2000 Arbin Instruments (USA), and a portable potentiostat WaveNow[xv] (USA) were used for the electrochemical test and analysis.

Scanning electron microscopy (SEM). Characterization of the microstructure and morphology of samples were carried out on JSM-7500F SEM apparatus of JEOL Ltd (Japan). Another SEM Crossbeam 540 from Zeiss (Germany) was also used with the focused ion beam (FIB) option to observe the cross-section of the samples before and after cycling for a-Si thin film anodes.

*Energy dispersive spectroscopy (EDS).*The uniformity of GF layer on Ni was studied using SEM combined with energy dispersive spectroscope EDS TM3030 (Hitachi). The morphology and elemental composition of SiC thin film were studied using a Quanta 3D 200i, EDAX from Thermo Fisher Scientific scanning electron microscope (USA).

Atomic force microscopy (AFM). The morphology of samples' surface and the thickness of the Si films was performed using atomic force microscopy (AFM) on a C3M SmartSPM-1000 (AIST-HT) in a tapping mode with an Al reflective side cantilever (NSG30 SS by TipsNano) measuring 125 mm in length and with a resonant frequency of 200–440 kHz. The samples for AFM were prepared on a polished glass with the marker line drawn on its surface prior to sputtering, which was then easily removed with acetone.

Raman spectroscopy. The structural features of the samples were examined by Raman spectroscopy on a LabRAM HR Evolution spectrometer (HORIBA Scientific, Japan) using Ar^+ ion excitation laser. The spectra of the films were obtained at the wavelengths of 532 nm or 633 nm, at magnifications of x10, x50 or x100, laser power of 25-100%.

Furrier Transform Infra-Red Spectroscopy (FTIR). FTIR, Nicolet iS (Thermofisher) was used to examine the graphene sheets synthesized on liquid gallium surface and for SiC thin film investigation after heat treatment with lithium metal.

*X-ray diffractometry (*XRD). The crystal structures of the investigated Si samples were analyzed using X-ray diffraction (SmartLab, Rigaku Co., Japan, Cu Kα radiation) over a 2θ range from 20 to 80°. X-ray Panalytical diffractometer was used for the samples heat-treated with Li metal.

X-ray photoelectron spectroscopy (XPS) is a surface-sensitive quantitative spectroscopic technique that measures the elemental composition at the parts per thousand range, empirical formula, chemical state and electronic state of the elements that exist within a material. XPS was used in this work for post-mortem analysis of 3C-SiC film.

Transmission electron microscopy was used for structural investigations employing JEM-2100 (JEOL Ltd., Japan).

The electrical properties of a-Si thin films was obtained by Hall effect measurement system (HMS5500/AHT55T5 Ecopia Co., South Korea). The thin film was deposited on the glass (1 cm^2) and the properties were registered at the current of 5 mA. The mean number of measurements was around 20 for each type of samples.

Porosimetry (Autosorb-iQ, Quantachrome Inst., USA) was used for the estimation of the porosity of prepared Cu substrates.

The mass increment of samples was controlled using weighting by an ultra-microbalance MSE2.7S-000-DM (Sartorius, Germany).

Preparation of pristine and cycled samples for characterization. The thin film deposition techniques for SiC and Si are described in the beginning of the corresponding sections in Chapter 4 and Chapter 6, respectively.

The as-prepared samples of SiC and Si did not require any special preparation procedures for characterization.

Characterization of SiC and Si samples after cycling required the thorough cleaning of the surfaces. The electrodes from disassembled cells were rinsed with DMC to remove the carbonate components of SEI layer. 3C-SiC additionally was immersed into the mixture of nitric acid (69 wt%) and hydrochloric acid (37 wt%) diluted by deionized water (DIW) with the volumetric ratio 1:3:50 (HNO_3:HCl:H_2O) for 10 min to remove oligomers, Li fluorides and hexafluorophosphates followed by careful rinsing in DIW and drying. However, Si samples used for study of SEI layer formation were not rinsed as explained above in order to save the layer.

3.2 Electrochemical testing

3.2.1 Cell assembling

For an evaluation of the electrochemical properties, the various cells were constructed inside an Ar-filled glovebox (MBRAUN, LABmaster Pro Glovebox, <0.1 ppm H_2O and O_2). A 1 M $LiPF_6$ EC: DEC: EMC (1:1:1, volume ratio) was used as an electrolyte; a microporous polypropylene film (Celgard 2400) was used as a separator, and metallic Li foil was used as both a counter and reference electrodes.

For long term galvanostatic cycling tests, coin-type CR2032 cells (Fig. 19) were used.

For the *in situ* Raman spectroscopic measurements, a hole was drilled in the cell and an optically transparent glass window was placed onto it (Fig. 20). To carry out *in situ/in operando* optical studies, a test cell was designed based on a flat cell (flat cell, Hohsen Corp., Japan). This cell was ideally suited for the planned work, since the assembly could be reused. The scheme of this cell is shown in Fig. 20.

Tightness is achieved using O-rings and springs, which can be easily assembled or disassembled [22].

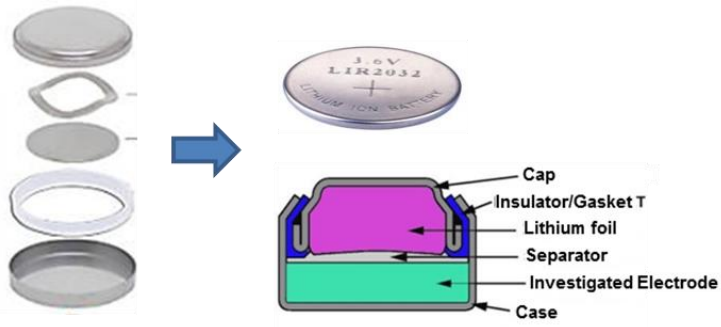

Fig. 19 Schematic view of battery parts, battery assembled using Coin 2032 type cell.

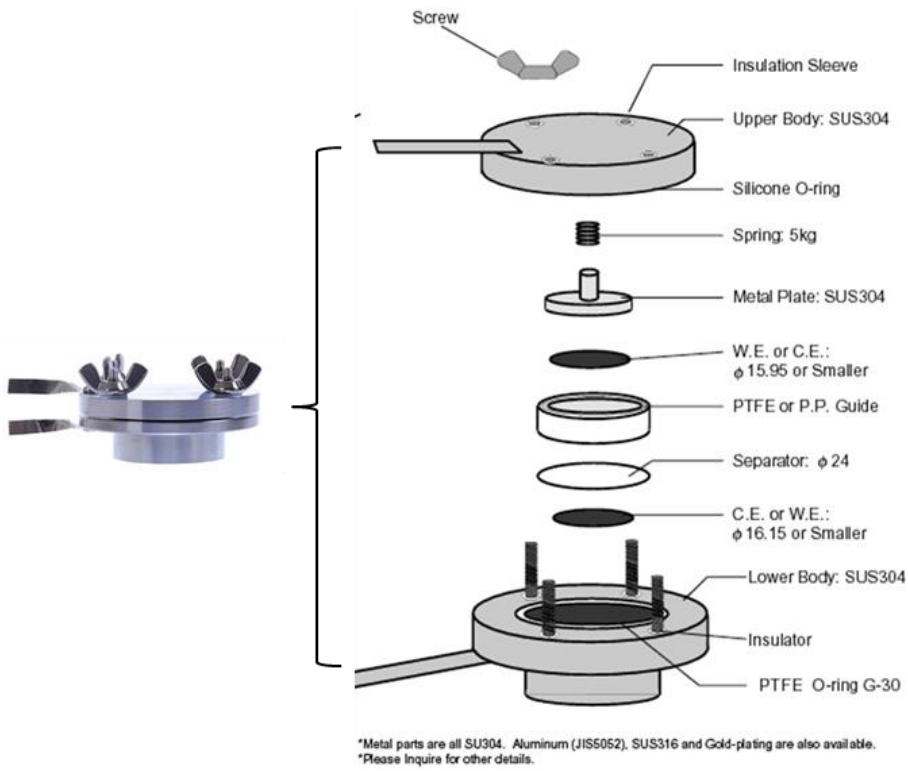

Fig. 20 Scheme of the flat cell.

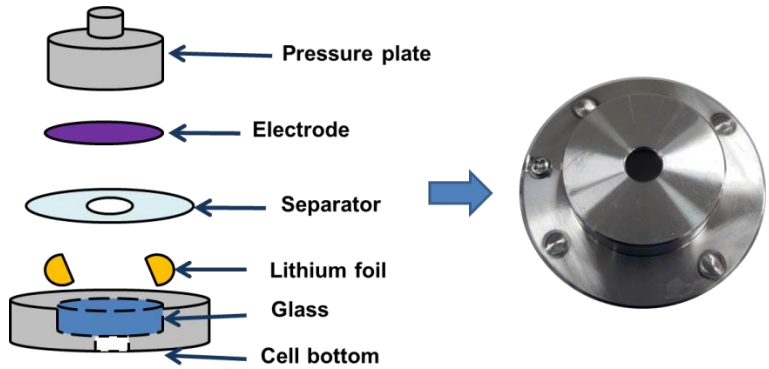

Fig. 21 Schematic view of battery parts and assembled battery of flat type cell modified for *in situ/in operando* measurements.

In order for a beam to pass freely and focus on the surface of the sample, it is necessary to make an appropriate optical window. Therefore, the original cell was modified. In particular, a hole was made in the lower part of the cell (Fig. 21). To fix the attached glass, a hole and a notch were made in the bottom of the cell. The sealing between the glass and the cell was performed using a Ni paste; the gaps between the edges of the glass and the cell body were filled with a PVDF polymer dissolved in a NMP solvent.

3.2.2 Electrochemical test methods

Various electrochemical methods such as cyclic voltammetry (CV) galvanostatic charge/discharge cycling (GC), electrochemical impedance spectroscopy (EIS) were used to retrieve a piece of information regarding the interaction of Li^+ ions with the investigated electrode materials. All the potentials given in the work are referred to the Li/Li^+ electrode potential.

Linear sweep voltammetry, one of the CV methods, is a useful tool to identify the best operation conditions for novel electrode materials [162]. After the set potential is reached in the CV experiment, the working electrode's potential is ramped in the opposite direction to return to the initial potential. The experimental setup for linear sweep voltammetry utilizes a potentiostat and a three-electrode setup to apply a potential to a solution and monitor the relevant electric current change.

The three-electrode setup consists of a working electrode, an auxiliary electrode, and a reference electrode. These cycles of ramps in potential may be repeated as many times as needed. The current at the working electrode is plotted versus the applied voltage (I/E) (that is, the working electrode's potential) to give the cyclic voltammogram trace. Fig. 22a illustrates a typical voltammogram of Si anode.

GC is a type of the chronopotentiometry methods, in which the constant current is applied to the electrode, and the potential changes to a value, at which the flux of the electroactive species is sufficient to supply the applied current. GC usually provides useful data on the formation of new phases when the plateaus on potential profiles occur at certain potentials. The capacity and cycling performance are the most important characteristics of the electrode materials for batteries. For instance, Fig. 22b demonstrates typical potential profiles for the $Li_4Ti_5O_{12}$ anode material; Fig. 22c shows a cycling performance for ZFO-C/LFP-CNT full-cell, which is plotted as capacity versus cycle number [163].

Rate capability is another type of cycling performance test, which has always been an important factor in the design of lithium-ion batteries. The rate of charge or discharge measures how fast the battery can be charged and discharged, typically called C-rate. At 1 C, the battery is fully discharged releasing maximum possible capacity in 1 h. A variation of the C-rate during the GC, the data on the capacity delivery after the significant current changes can be obtained. For example, Fig. 22d illustrates the graph for TiO_2-nanotube half-cell where the C-rate was changed within a range of C/5 – 5C [164].

EIS is widely used to characterize the charge carrier transfer and charge storage process. Electrochemical impedance is the response of an electrochemical system (cell) to an applied potential, and the frequency dependence of this impedance can reveal underlying chemical processes. EIS serves for two purposes: for diagnostics, to characterize changes at a surface under specific system parameters; and for application, to tailor system parameters in order to obtain a desirable effect on a surface. To describe the interface properties, the graphical spectrum, Nyquist plot, is

fitted by the most suitable equivalent circuit. For example, Fig. 22e shows the experimental data and the equivalent circuit used to fit the EIS [165].

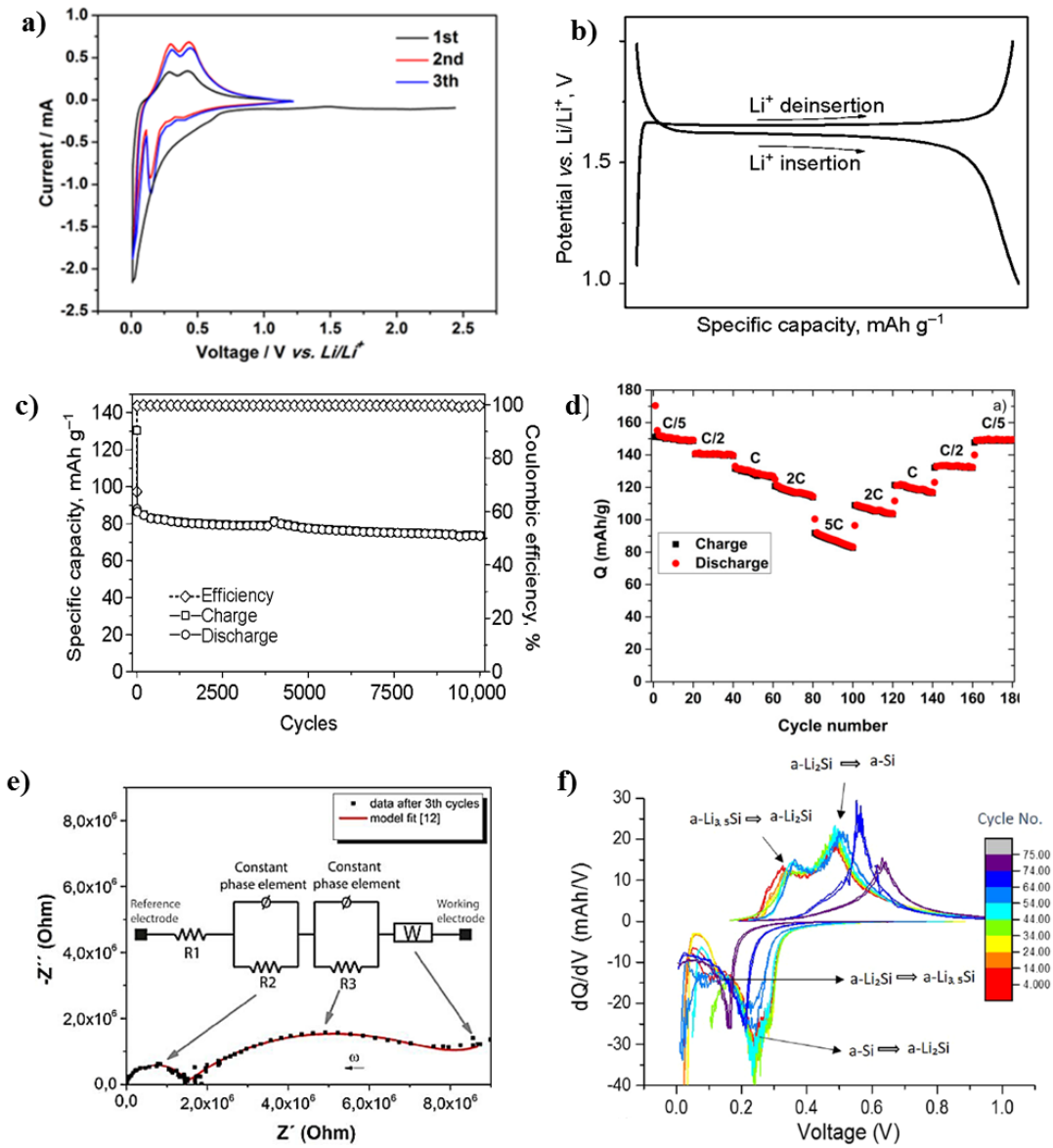

Fig. 22 The examples of (a) voltammogram, (b) potential profile and (c) cycling performance, (d) rate capability, (e) EIS spectrum, (f) differential capacity plots.

Differential capacity is a graphical analysis of the cell cycle life taken from the GC data. The differential capacity plots, which built on the base of differential capacity (dQ/dV) versus potential, show the changes of charge and discharge curves

and give information regarding both the underlying kinetics and thermodynamics of the system. Studying the changes in the cell's electrochemical performance through the differential capacity allows predicting its failure [26,166,167]. Fig. 22f demonstrates the example of dQ/dV graph for Si material.

In this work, CV results of Si, GF, NiO, Cu, and SiC were recorded by cycling the assembled cells with the investigated electrodes at various potential ranges, mostly within 0.01 – 3 V vs. Li/Li^+, and at the different scan rates in the range of 0.1 – 0.3 mV s^{-1}. EIS were recorded before and after galvanostatic cycling at 5 mV amplitude signal in the frequency range of 0.1 Hz to 1 MHz. GC tests were carried out in a potential range of 0.01 – 3 V, and at the current densities chosen within 1 – 100 μA cm^{-2} for all materials, investigated in the research.

3.2.3 *Ex situ* / *in situ* / *in operando* characterization methods

When developing rechargeable LIBs, it is extremely important to develop electrodes with high electrochemical characteristics and to understand the nature of the processes occurring in materials during operation. The direct monitoring of these processes is capable to retrieve information about the electrochemical characteristics of the electrodes. *In situ* research allows controlling complex chemical and physical processes in the electrodes during the charge and discharge processes, and thus, offers the ability to directly link these processes to the electrochemical response of the battery [168].

The Latin expression "*in situ*" literally means "in position", and in battery research, this refers to measurements that are performed on materials in their original position inside the sealed device, i.e. without it disassembling. This allows characterizing materials under more realistic conditions, contrary to *ex situ* measurements. *Ex situ* measurements can furthermore be disturbed as a result of contamination during sample preparation and handling between battery use and characterization. *In operando* characterization represents a special case of *in situ* research, where the battery is in operation, i.e. is being (dis)charged during

characterization, allowing measurements of non-equilibrated states that cannot be disclosed with *ex situ* characterization [169]. In order to conduct *in situ* experiments, batteries must be fully operational under the circumstances imposed by the diagnostic tool, which often demands specially designed devices and measurement setups, thereby hindering the straightforward application of *in situ* techniques. Fortunately, *in situ* methods to characterize LIBs recently experienced a rapid development, which is evident from the increasing amount of publications on this topic.

4 SILICON CARBIDE THIN FILM ANODE

4.1 Introduction

This chapter comprises the results on the study of new monocrystalline 3C-SiC as an anode for LIBs. The general information on the reasons and aims of this research were given in the literature review (Chapter 2, §2.4). The various techniques and approaches were applied for multifaceted investigation of 3C-SiC. Here, the results of the electrochemical behavior upon Li^+ ions insertion are presented. The effect of heat treatment of the samples with lithium at elevated temperatures on their physical properties and stability is discussed.

4.2 Silicon carbide thin film preparation

CVD is widely used to deposit thin film materials on various substrates made from solid non-volatile materials. Epitaxial growth of films is a non-equilibrium kinetic process. The reaction gases must be of high purity to reduce the degree of contamination of the grown film. This method is widely used in semiconductor technology to deposit single-crystal, polycrystalline and amorphous films, for example, silicon, silicon nitride, and others. CVD method consists of several steps, including preliminary mixing of the reagent gases and inert carrier gas and introduction of this mixture into the chamber; supplying the gas mixture to the substrate; formation of growth species by chemical reaction in gas phase and/or adsorption of the species/reagents on the substrate surface; formation of a solid thin film on the substrate surface; and removal of gaseous reaction by-products from the chamber [170–172]. The scheme of the equipment with process is shown in Fig. 23a.

SiC thin film was epitaxially grown on an on-axis, 10 cm, 525 μm thick Si (001) wafer by Reduced Pressure CVD (RP-CVD) in an LPE ACIS M8 reactor using trichlorosilane ($SiHCl_3$), ethylene (C_2H_4) and hydrogen (H_2) as the Si precursor, carbon precursor and gas carrier, respectively. An initial carbonization step was done at 1140 °C followed by growth of the SiC layer at 1350 °C [173,174]. The image of the final SiC thin film on Si wafer is shown in Fig. 23b.

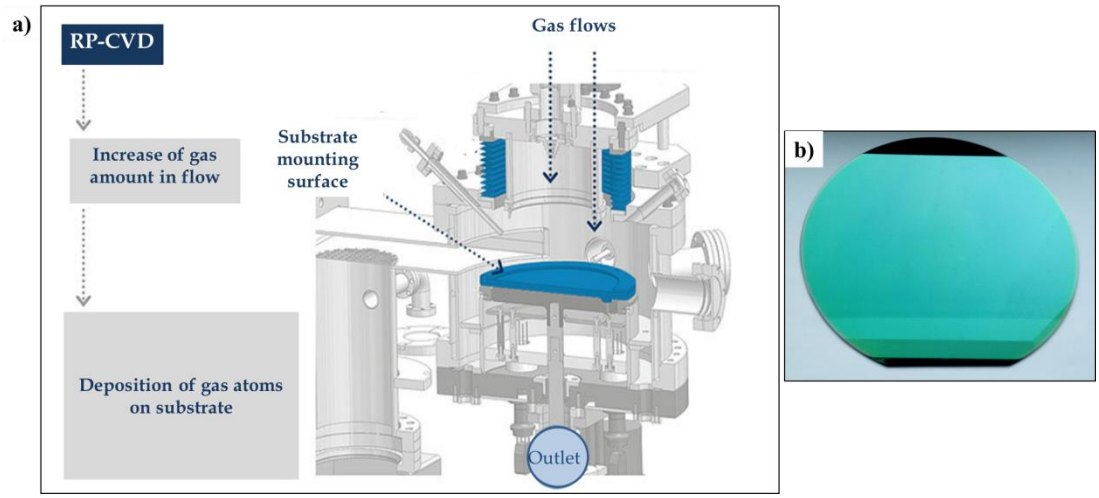

Fig. 23 (a) Scheme of equipment and process of RP-CVD technique and (b) SiC film on Si wafer.

4.3 Characterization of SiC thin film

The multifaceted characterization has been performed in order to analyze the SiC material properties such as crystallinity, morphology, and topology using various available methods.

The XRD spectrum of SiC thin film on Si wafer is shown in Fig. 24a, where three intensive peaks can be observed. The one with the highest intensity is located around 34.56° 2θ which is the typical for Si and arises from the substrate the film was grown on. Two peaks with a slightly lower intensity are are observed at 21° and 45°. These peaks are related to SiC(002) and SiC(004) with a cubic lattice (3C-SiC) [175,176]. No any other peaks were observed confirming that a monocrystalline and high quality SiC film was prepared.

Fig. 24b shows the obtained Raman spectrum, which was fitted by Gauss function (see Fig. 25). One can see that the left peak consists of three bands at 766, 794 and 812 cm^{-1}. The peak on the right side also comprises three bands located at the shifts of 943, 965 and 987 cm^{-1}. The last one is related to the second-order Raman scattering on Si. The peaks appeared around 794 and 965 cm^{-1} correspond to

a transverse optical (TO) and longitude optical (LO) modes of the cubic lattice, respectively [177–179]. Thus, Raman and XRD analysis showed that 3C-SiC grown on Si(004) is a high-quality monocrystal.

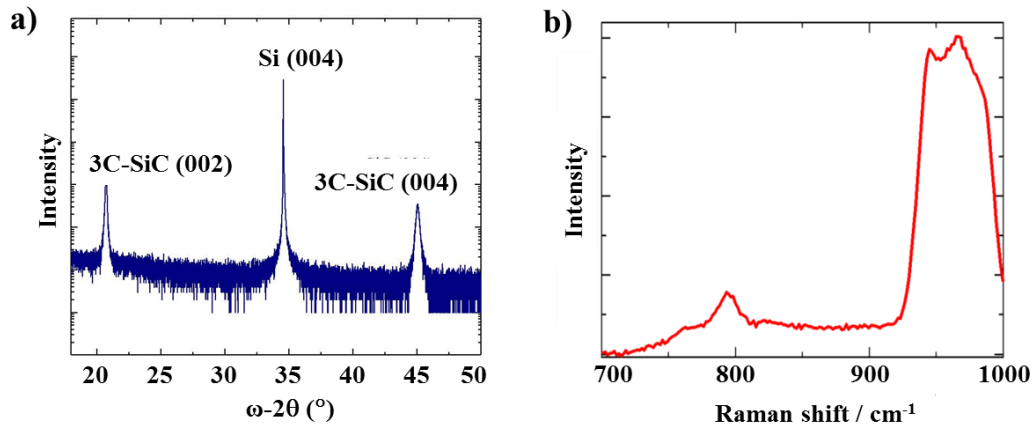

Fig. 24 (a) XRD spectrum of 3C-SiC and (b) Raman spectrum of 3C-SiC.

In order to investigate topology of 3C-SiC samples AFM studies in the tapping mode were performed. Fig. 26a represents the measurement in height (topography) imaging. Considering the results, it can be summarized that the sample's surface is nonuniform with the longitudinal areas with elevated and lowered heights occurring alternately with the step of 20-30 nm. Fig. 3b shows the AFM image taken from a cantilever's amplitude modulation. The height difference cannot be observed here; however, the surface is seen more clearly than in the previous image. One can see that 3C-SiC thin film does not possess an absolutely flat surface. There is a slight roughness with a presence of hemispherical growths with the dimension no more than 150 nm.

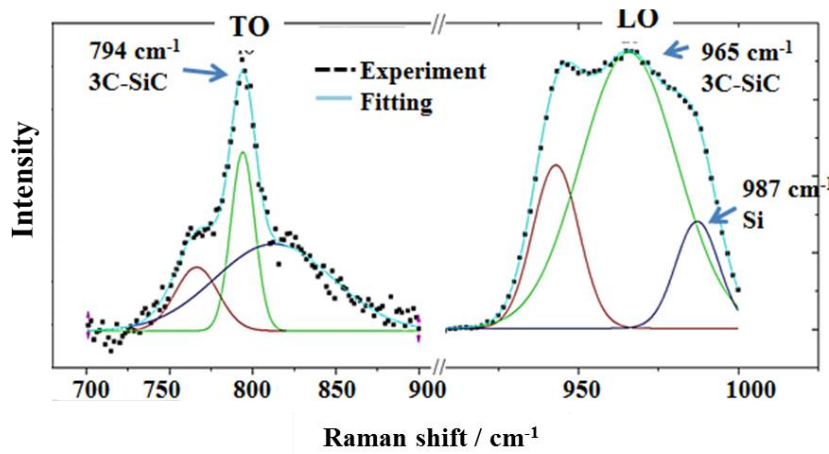

Fig. 25 The fitting results of Raman spectrum of 3C-SiC film.

From Fig. 27, the EDS elemental mapping showed the uniform distribution of Si and C. A small peak at 0.3 keV in Fig. 27a corresponds to carbon, while the intense peak at 1.7 keV is a signal from silicon.

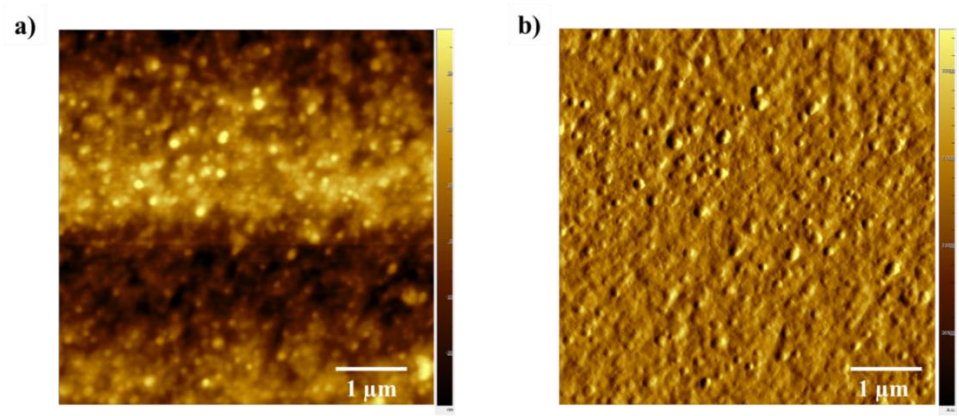

Fig. 26 AFM images of 3C-SiC thin film surface (a) high mode, (b) amplitude modulation mode.

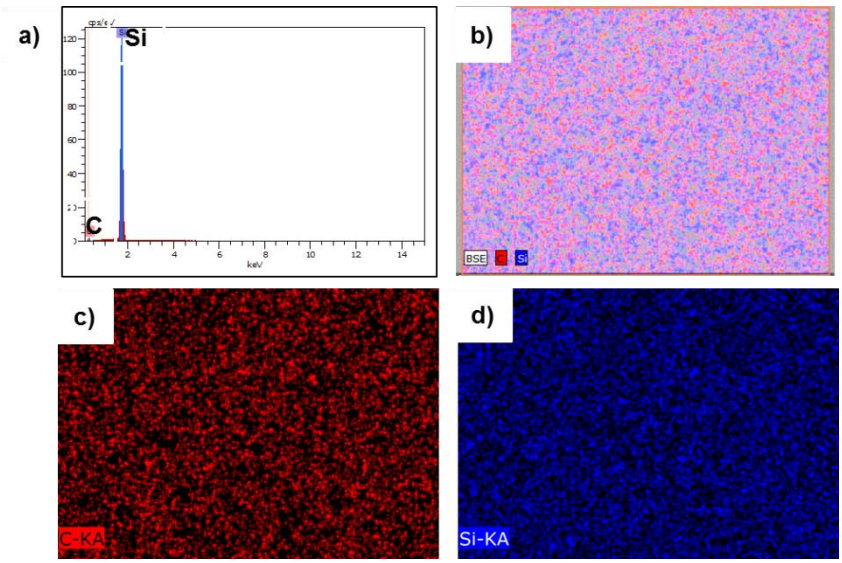

Fig. 27 EDS of 3C-SiC on Si wafer.

For a further detailed study of samples morphology, SEM investigation has been performed. Fig. 28 demonstrates the surface image of 3C-SiC at low and high magnifications. It can be seen from Fig. 28b-d that the surface does not have only hemispherical growths which were detected previously by AFM but also there are thin straight grooves with the length around 100 nm. In fact, the hemispherical growths are SiC crystals grown slightly above a film surface. It was proposed that such areas served as nucleation sites [180,181]. During the growth, the crystals from adjacent ‘seeds’ formed a common boundary resulted in a propagating grooves [182]. Usually, such defects annihilate with time; however, taking into account the low thickness of the 3C-SiC film; thus, the defects did not have a chance to disappear. Fig. 28e,f shows the cross-sectional images. The best view of 3C-SiC can be found at the higher magnification as a top thin layer on the sample. The thickness of 3C-SiC was estimated from the SEM images to be about 330-360 nm. Thus, the performed investigation of SiC allowed determining the cubic lattice of the thin film and its morphology features.

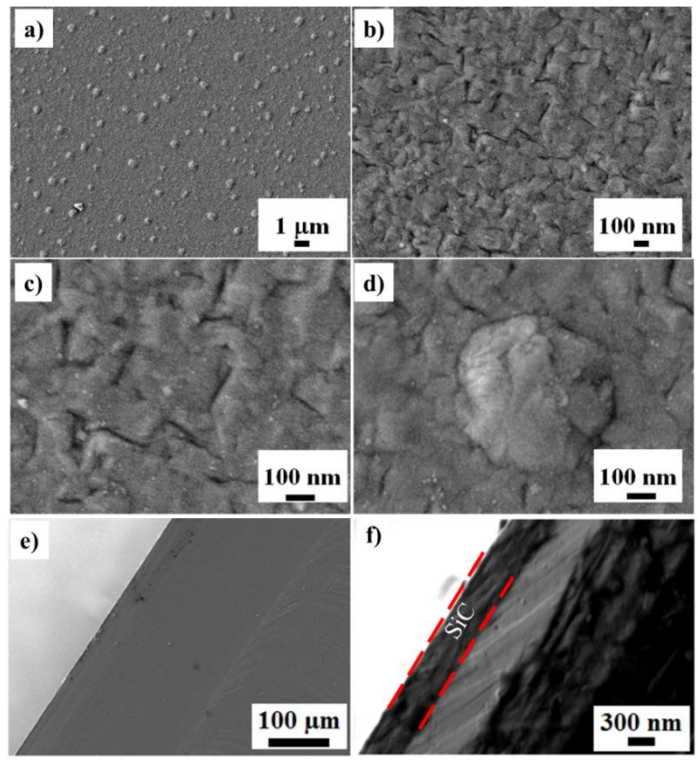

Fig. 28 SEM images of pristine 3C-SiC (a,b,c,d) at different magnification and (e,f) cross-section of the samples.

4.4 *Ex situ* thermal studies of SiC–Li interaction at various temperatures

The thermal experiments were conducted in order to investigate the interaction of 3C-SiC with Li metal at various temperatures from 25 to 300 °C and possible alloying of these two components. It is known, that Si material experiences fast degradation upon the continuous cycling, i.e. lithiation/delithiation reactions, due to the material volume variation upon alloying and dealloying with Li. Finding the new materials, which can be stable and durable upon cycling, is one of the main aims of scientists in the field of LIBs. Taking into account outstanding mechanical stability of 3C-SiC and possibility of Li intercalation into its structure, upon its successful development, such anode could be used in batteries for a wide range of applications.

The idea of conducting this kind of research has come due to the fact that at this moment very little data available on the mechanism of lithiation of 3C-SiC.

When performing these preliminary studies, the data was ambiguous and difficult to analyze. It was obvious that the possible mechanism of 3C-SiC interaction with Li should be confirmed or rejected. Elevated temperatures could help to accelerate such interaction. Monocrystalline Si(001) wafer has been taken for the comparison due to its alloying with Li is beyond doubt.

4.4.1 Preparation for an *ex situ* thermal studies of SiC–Li interaction

For the heating experiments, the cell was adapted from a split cell (EQ-STC, MTI Corp.) by removing all plastic parts (Fig. 29). The samples were preliminary cleaned with ethanol in an ultrasonic bath and dried. Then, pure metallic Li foil chips (Li, 99.9 %, MTI corp.) were placed and slightly pressed on the top of the samples as illustrated in Fig. 29b. The cells with samples were tightened in an argon-filled glove box (99.99 %, H_2O < 0.1 ppm, O_2 < 3 ppm). The experiment was carried out as follows. The sealed cell was heated up to a certain temperature for 60 min in a muffle oven ELF 11/14 from Carbolite Gero (Fig. 29a). Then, the cell was disassembled and Li metal was taken off from the sample surface. Fig. 29c shows the appearance of Si wafer after heating at 150 °C. Several samples were prepared for each type of heating conditions.

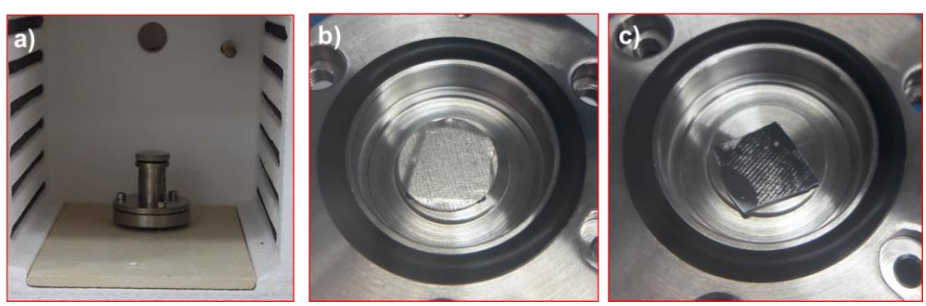

Fig. 29 Images of sample a) heating cell, b) sample with covered metallic Li and (c) without it after heating.

4.4.2 Results and discussion of *ex situ* thermal studies

As it was mentioned above, the possibility of temperature-induced alloying of monocrystalline Si and 3C-SiC with metallic Li was investigated at the elevated temperatures up to 300 °C. Fig. 30 demonstrates the images of the samples on which the changes can be observed after their heat treatment with Li metal from room temperature to 300 °C. One can see from Fig. 30 that the samples look differently at various temperatures. The first line in Fig. 30 shows that Li loses a gloss and almost disappears after 225 °C. This is due to its melting at 180.5 °C. Here, in the experiments, Li melted at the temperatures above 200 °C which could be resulted from non-uniform heat distribution over the heating cell, i.e. the temperature was lower in the center of the cell comparing to its case. The surfaces of Si samples altered in areas where they touched with the Li metal. At the temperatures above 225 °C, the Si samples crumbled. For 3C-SiC (line 3 in Fig. 30), the deterioration of the surface occurred at a higher temperature above 250 °C. At a closer view, it can be seen that the unchanged islands of SiC still remain after heating at 250 - 300 °C. Besides, the mechanical stability of all 3-SiC samples was much better after heating in contrast with Si samples, which tended to crush.

Fig. 31 shows the XRD coupled scans of Si and SiC. The plots in the upper part of Fig. 31a,b demonstrate the overall XRD spectra measured within a range from 15° to 55°, while the lower part of Fig. 31c,d presents the magnified peaks to demonstrated their detailed features. From Fig. 31 a,b, the presence of an intensive peak around 35° can be observed, which is related to Si and was discussed in the previous paragraph. It can be seen that the Si peak shapes are different for the differently annealed samples, and the peak shape changes with the emergence of a new shoulder above 100 °C followed by splitting into two peaks after 250 °C. Such changes could be related to an obvious degradation of the Si crystal structure upon heating to higher temperatures. New peaks start to appear upon annealing in the patterns for Si wafer, at 41° (from 100°C) and 39° (from 200°C). It can be observed that the intensities of these peaks are higher for the samples annealed at the higher

temperatures. Fig. 31c,d shows the XRD patterns of the 3C-SiC thin film on Si wafer. The magnification of the peaks revealed that there is no rearrangement of the Si and C atoms in SiC happening during the reaction with metallic Li. This indicates that, in contrast with Si, 3C-SiC does not react with Li, which cannot permeate through the 3C-SiC crystal lattice. However, after annealing samples above 225 °C, the SiC signal disappeared.

Fig. 32 displays the RSMs of the samples measured after annealing with metallic Li at 100, 200, and 300 °C. Fig. 32a shows the results for Si wafer, Fig. 32b,c shows the results for 3C-SiC on Si wafer. On the first row (Fig. 32a), one can see a reflection from the Si (004) wafer at 0.737 $A^{-1}(Q_z)$, which changes from a typical circular form to a diamond-shaped reflection with a lateral elongation. This indicates the deformation of the Si crystal. From the last two rows (Fig. 32b,c), for the 3C-SiC epitaxial film, the relaxation was observed at around 0.920 $A^{-1}(Q_z)$. We can see that 3C-SiC persisted on Si wafer after all heating experiments. However, the reflection of SiC was found to be much weaker for the samples annealed with Li at 300 °C.

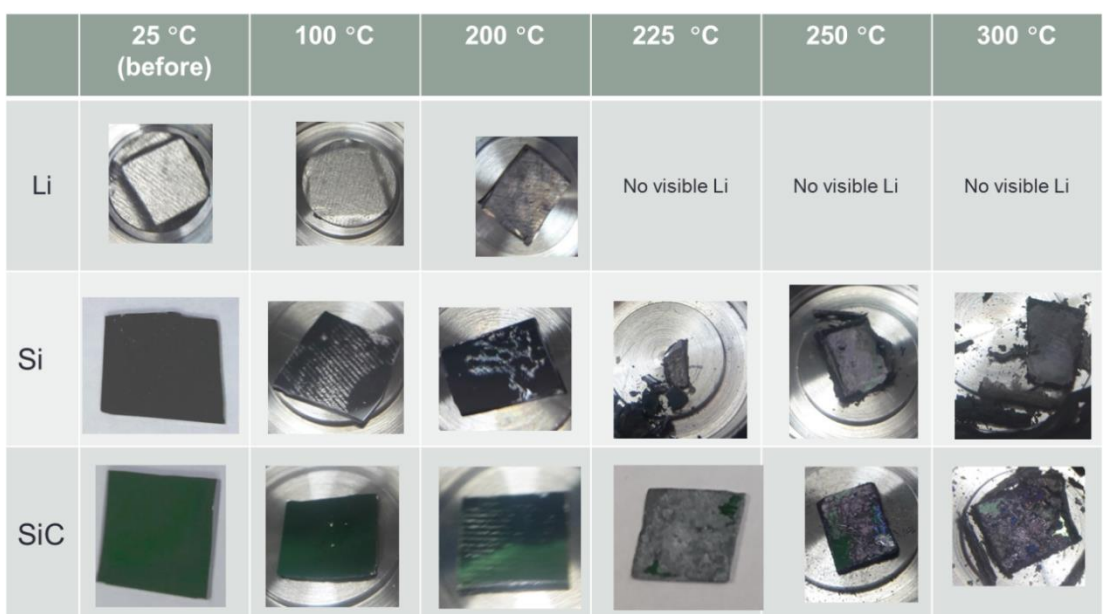

Fig. 30 Images of Si and SiC samples upon heating at various temperatures.

Fig. 33 shows the FTIR spectra of the investigated samples. From Fig. 33a, it can be noted that Si does not absorb at the wavelengths above 2000 cm^{-1}. The peaks appearing around 3000 cm^{-1} are due to C-H symmetrical stretches and those appearing around 3600 cm^{-1} are due to O-H stretching. These peaks might appear because all Li left on the sample surface after removal of the Li foil reacted with air and oxidized forming LiOH, Li_2O and, reacting with CO_2 of air, the carbohydrate residuals. As the temperature of plating with Li increases, it can be observed that these peaks intensify around 225 °C and cease a bit upon the further temperature increase. This might indicate that Si reacts with Li even more at this temperature. For the frequencies below 2000 cm^{-1}, some peaks appear around 1108, 866, 740, 1425, 610 cm^{-1}, and can be seen for Si (Fig. 33b) with no Li plating. This could be an indication that these peaks are not due to Si, but due to the background spectra. SiC exhibits an intense Si-C stretch at around 800 cm^{-1} as can be seen from the spectra for the bare SiC (Fig. 33c). However, with a further temperature increase to 225 °C, this peak disappears completely. As for Si, this could reflect the reaction of Si and Li. The fact that we observe C-H absorption for the bare SiC can be explained by the impurities of hydrogen in the material.

The morphology of the samples was investigated by SEM. Fig. 34 illustrates the series of the SEM images of the samples' surface after heat treatment with Li at five temperatures: 100, 200, 225, 250 and 300 °C. The insets in each picture show a magnified view of a corresponding image. The first column of Fig. 34 is related to the Si samples, the second column shows the SEM images of the 3C-SiC. Each row corresponds to the certain temperature which is pointed in the left side. For the Si, we can notice the residuals of metallic Li attached to the Si surface. Si had the changes near Li flakes possibly indicating the formation of another phase at those places. With the increase of the temperature, the surface formations become more isolated. For the last Si sample (300 °C), the cracks on the surface were observed that are most likely resulted from the difference of stresses appeared in the Si near-surface regions during the formation of new alloys. SEM images of the SiC samples revealed the

different morphology. Reviewing the SiC microimages (second column), the residual Li stay on the 3C-SiC surface and no spots around them can be detected. However, for other 3C-SiC samples annealed with Li above 225 °C, the absence of the SiC-Li reaction is not that obvious. Moreover, from the SEM image of the last SiC sample heat-treated at 300 °C, it was revealed that the near-surface region of the sample was broken, and some fragments were on its surface after the heat treatment at this temperature. We suppose that Li could penetrate into the near-surface region 3C-SiC through diffusion near the defects or through crystal boundaries without the intense chemical reaction. The stresses occurred in the material could result in its fracture in the near-surface region.

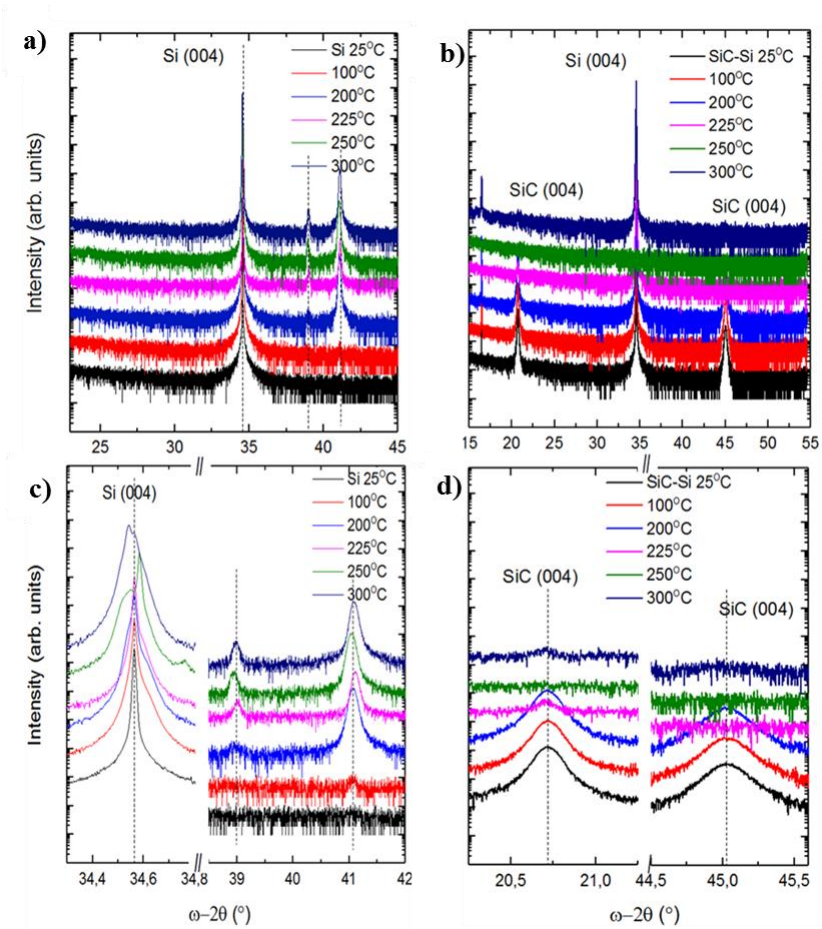

Fig. 31 High-resolution XRD (004) plane ω/2θ curve for (a, b) Si wafer and (c, d) 3C-SiC on Si wafer after heat treatment with metallic Li.

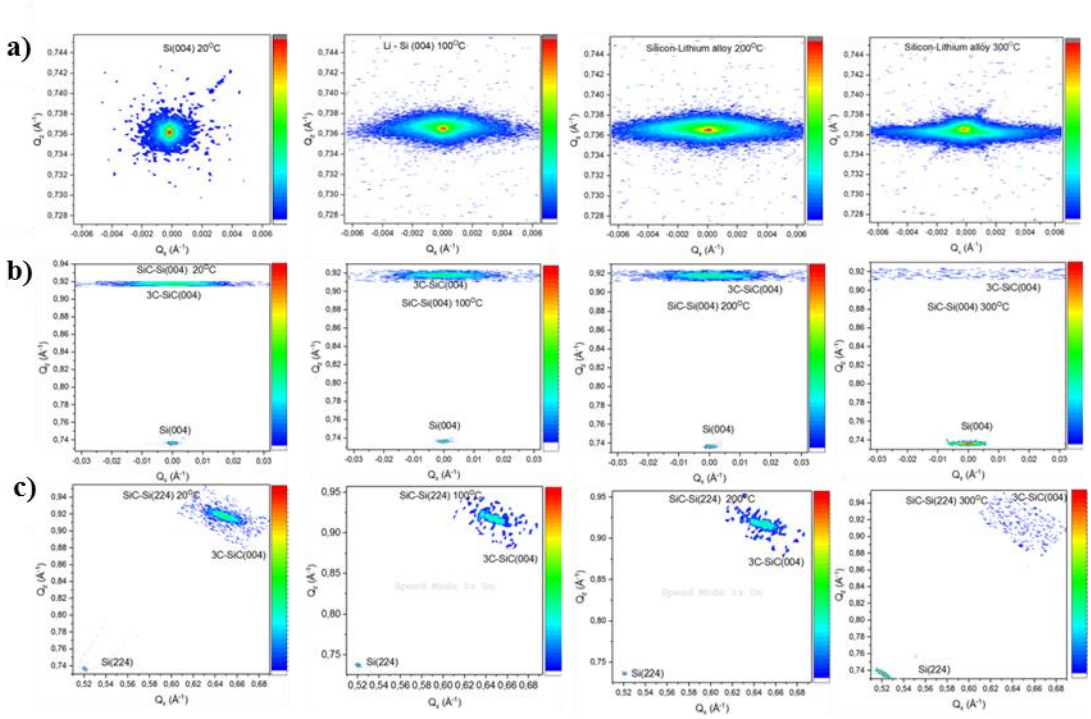

Fig. 32 RSM maps of untreated samples (25 °C) and heat treated with metallic Li at various temperatures (100, 200, 300 °C): (a) Si and (b, c) 3C-SiC.

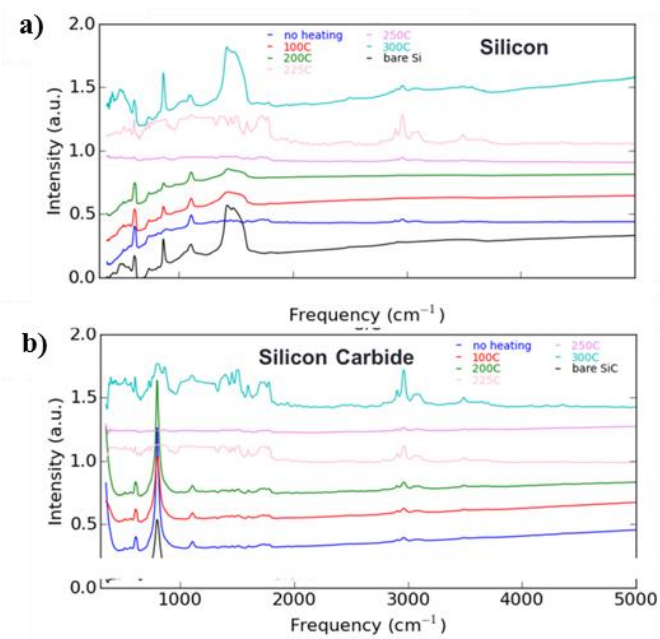

Fig. 33 FTIR spectra of (a) Si, (b) SiC at various heat treatment temperatures with metallic Li.

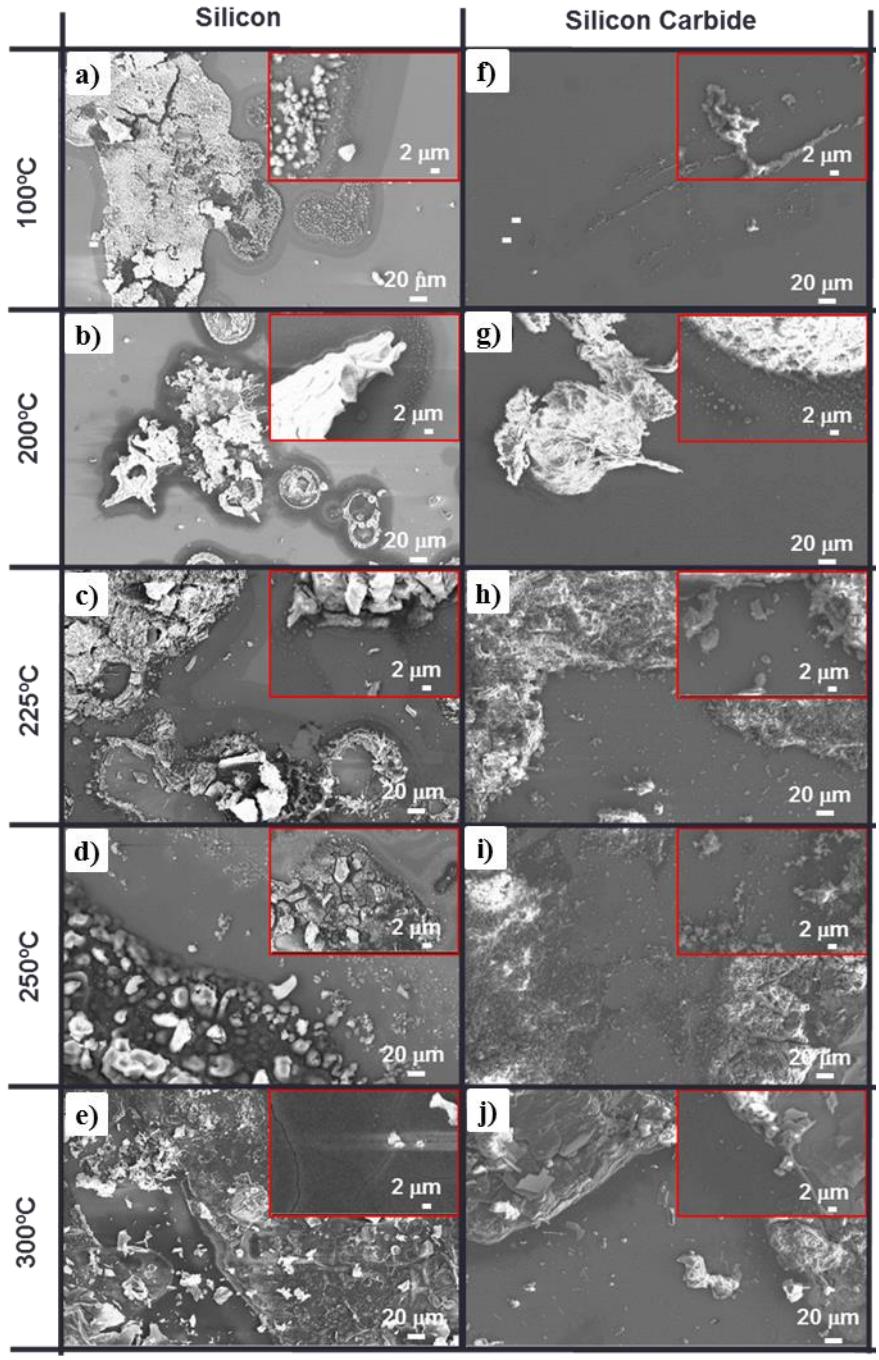

Fig. 34 SEM images of samples after heat treatment with metallic Li at different temperatures (a-e) Si and (fj) 3C-SiC.

4.5 Study on the SiC by ‘single’ particle measurement

A “single” particle (SP) measurement is one of the advanced methods which allows investigating the intrinsic electrochemical properties of single particles of electrode materials for LIBs. The measurement allows the evaluation of electrochemical properties of a single particle of material without other supporting additives such as conducting agents or polymer binders, which ensure excluding an effect of any side processes on the results of the measurements [183]. Along with the electrochemical properties, the expansion of single particles can be estimated as well. The study is usually carried out in the Ar-filled glovebox in order to avoid the oxidation reactions. Fig. 35 shows the scheme of experimental set-up on the left and the process of tip landing on the surface of the 3C-SiC sheet on the right. The microscope, manipulator and portable potentiostat were used to control and perform the electrochemical measurements. The tip landing is a sophisticated process which requires the attention and caution.

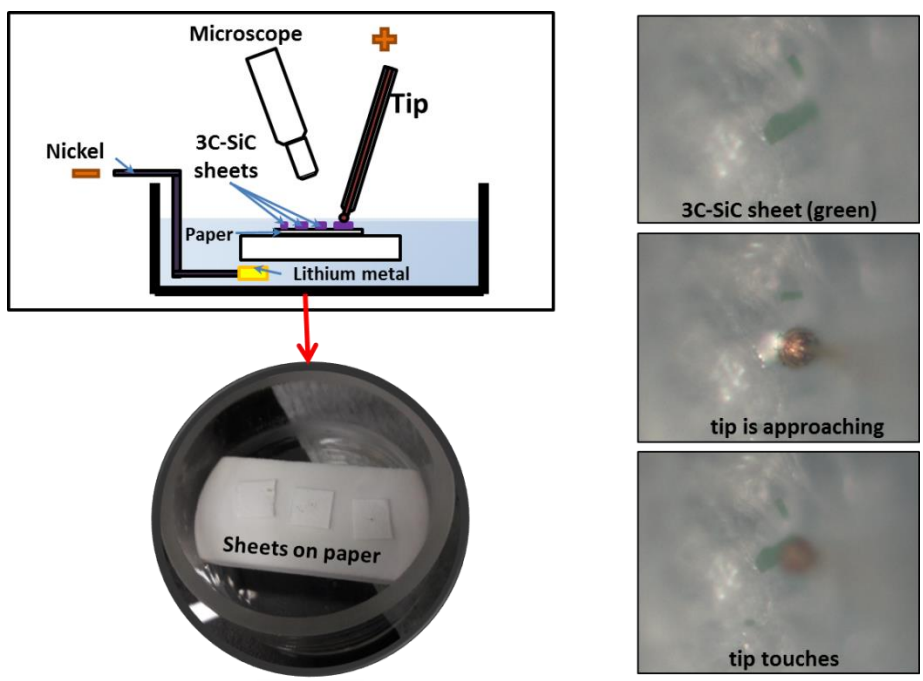

Fig. 35 (a) Image and (b) scheme of SP measurement system.

This outstanding SP method was used to deeply investigate the Li^+ ions insertion/extraction properties of monocrystalline 3C-SiC. For these measurements, ~1 µm thick sheets of 3C-SiC thin film with dimensions of around 10 – 20 µm were used. The 3C-SiC sheets were separated from Si wafer using a conventional lithography procedure described elsewhere [173]. CV of the 3C-SiC using SP method was obtained for the first time.

The CV plot of the initial three cycles of the 3C-SiC thin film is shown in Fig. 36a. The CV plot showed the following positions of the peaks: four redox peaks at 0.6, 1.1, 1.5, and 1.7 V and two oxidation peaks at 2.0 and 2.4 V (shoulder). The lithiation peak at 1.8 V (Fig. 36c) shifted to 1.86 V in the second cycle. This can be related to the increase of surface resistance due to a SEI layer formation. The reversible redox peaks are due to the lithiation/delithiation reactions in the 3C-SiC electrode when Li^+ ions permeated/extracted into/from the material. It can be seen that the shape of first delithiation peak of the 3C-SiC thin film increased acutely. Such sharpness of the lithiation/delithiation CV peaks might be the sign of the intercalation mechanism of Li^+ ions insertion into the material [184,185].

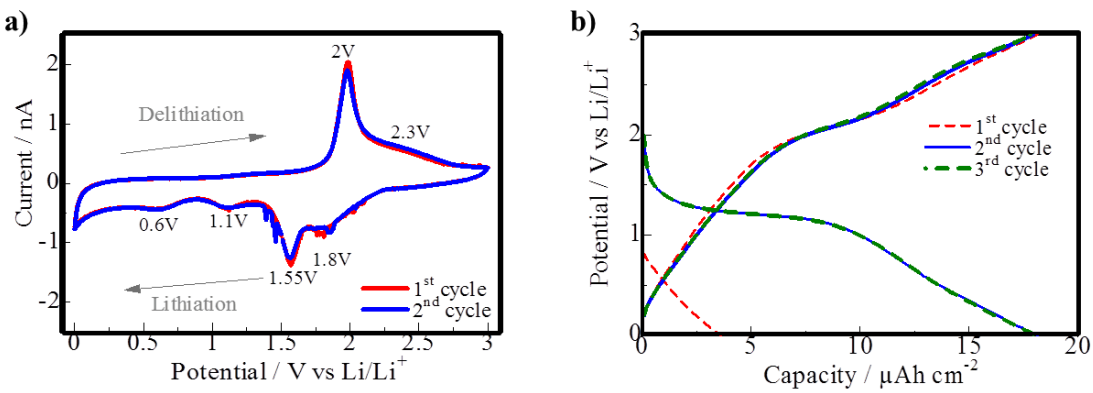

Fig. 36 Results of the SP measurements of 3C-SiC (a) CV, and (b) potential profiles.

The CV curves and peak positions recorded for 3C-SiC film absolutely differ from that of Si [186] but are slightly similar to that of $Li_4Ti_5O_{12}$ (LTO) [187]. This suggests that investigated 3C-SiC can be used as a negative electrode coupled with

the high potential electrodes or as a positive electrode with the low potential electrode materials.

Fig. 36b shows the potential profiles for 3C-SiC samples measured using GC. The plateaus can be noticed within 1.5 – 1.3 V during discharge (lithium insertion) and around 2 V during charge (lithium extraction).

In the usual case of SP measurements, the spherical particles of material are used, the volume and mass of which can be easily estimated. In our case, the 3C-SiC's shape was the sheet with the uneven edges (Fig. 35), that limited the ability to accurately calculate the sample's mass and, subsequently, to get a specific capacity. Thus, using SP method for this particular material, the exact specific capacity of 3C-SiC could not be assessed.

4.6 Electrochemical test of 3C-SiC thin film

4.6.1 Electrode preparation

Before battery assembling, careful cleaning of the 3C-SiC sample surface is mandatory in order to avoid the side reactions on the sample surface during the electrochemical tests. The 3C-SiC samples were cleaned by sonication in ethanol for 1 h in order to remove organic impurities; then, the samples were immersed into the mixture of hydrofluoric acid and nitric acid with a volumetric ratio 1:3:50 (HNO_3:HF:H_2O) for 5 min to remove the rest of contaminations and native oxide layer on the Si wafer. After this, the samples were rinsed with distilled water and dried.

The schematic view of the ~ 350 nm 3C-SiC sample is illustrated in Fig. 37a. In the initial experiments, a metal holder, prepared from a 100 μm thick single piece of stainless steel foil, was used as a current collector. The holder was wrapped around the sample. Since the open sides of a low-conductive Si substrate could directly affect the electrochemical performance, they were coated by an isolative epoxy. However, it has been found that despite an epoxy coating, the Si substrate

could react with Li^+ ions and contribute to the overall capacity. In order to avoid this process, the Si substrate was removed by etching with HF acid, and separated 3C-SiC was glued to a steel disk by PVDF-based conductive glue. Fig. 37b shows the sample without the Si substrate, which was used for the rest of the electrochemical experiments.

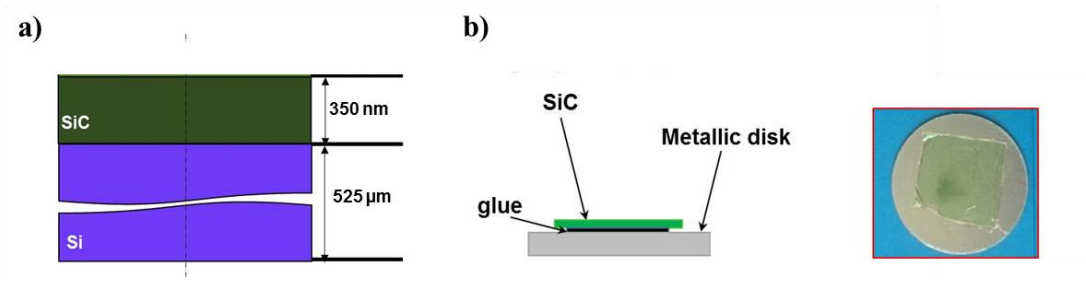

Fig. 37 Schematic view of (a) 3C-SiC thin film on Si substrate and (b) 3C-SiC thin film on a metallic substrate.

4.6.2 Electrochemical test results and discussion

The investigation of 3C-SiC was carried out using CV and GC. Fig. 38a shows the CV scans registered under 0.1 mV s^{-1} conditions in a potential range 0 – 3 V. It can be seen that the first cycle data represent a less ordered character than that of the others cycles. Most likely, this is due to the loss of Li^+ ions during the formation of SEI on the surface of the electrode. The main anodic peaks are around 1.4 , 0.7 and 0.02 V; the cathodic peaks appear at the potentials of about 1.17 V and 2.13 V. It is worth noting that some electrochemical similarities with the CV scans obtained by SP method have been preserved, in particular, the same peaks in the regions of 1.3 – 1.5 V and 0.5 – 0.7 V upon lithiathion and 2 V when lithium is extracted. However, the overall shape of the hysteresis changed, and new cathodic peaks appeared at 0.13, 0.32 and 1.17 V, the latter of which is more intensive. It can be suggested that these peaks could be due to the other reactions of Li^+ ions with 3C-SiC. Probably, during the film transfer, the structure of 3C-SiC was damaged in some regions and defects could occur, which in turn could participate in the Li^+ ions adsorption and release.

Fig. 38b shows potential profiles of 3C-SiC, measured at a current of 10 µA

cm^{-2} in a potential range of 0.01 – 3 V. The observed potential plateau situation corresponds to peaks on the CV scan for this sample. From Fig. 38b,c, it can be seen that the capacity of the electrode in the first discharge cycle reached 34 µAh cm^{-2}, and then dropped to 14 µAh cm^{-2}. However, considering the charge profiles in Fig. 38b, one can see that the capacity on the 5th cycle becomes greater than the capacity of the second cycle. Over time, the capacity of the electrode continues to increase gradually, reaching 24.3 µAh cm^{-2} and 25.7 µAh cm^{-2} in the 36th discharge and charge, respectively. The coulombic efficiency of the samples throughout the cycling was in the range of 80 – 96 %, which indicates the loss of Li^+ ions during the cell operation of the cell. Unfortunately, the electrochemical tests obtained in the coin cell showed a very low areal capacity of the electrode.

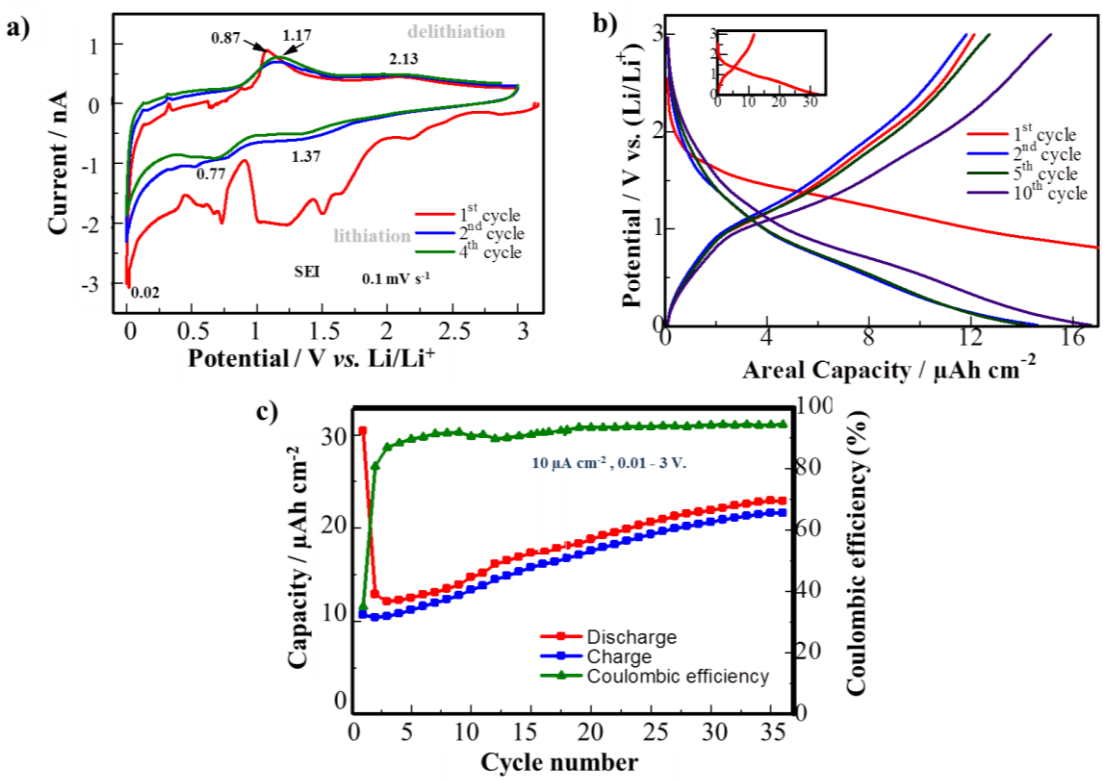

Fig. 38 Results of electrochemical tests of 3C-SiC in coin cell: (a) CV, (b) potential profiles, and (c) cycling performance.

Considering the results of the 'SP' measurements, it has been suggested that

the Li^+ ions insertion can goes via their intercalation into 3C-SiC. However, after the electrochemical test in the coin cell, it was suggested that such behavior of the 3C-SiC can be also caused by a Nonfaradaic, or capacitive, reaction [188,189]. Such process is a case where no redox reaction happens at all, or the redox reaction at the electrode involves some atoms in the electrode structure, or when the reacting species is oxidized/ reduced at the electrode, but then stays there. In order to make a final decision on the observed reactions, the study of the electrochemical interaction of 3C-SiC with Li^+ ions has to be continued.

4.6.3 Post-mortem analysis of 3C-SiC

After the electrochemical test, the post-cycling or so-called post-mortem analysis has been performed. The study of alterations in the electrode material during its continuous testing is an important step for obtaining information on degradation rate, mechanical strength of a material, properties of its crystal structure. This data can be used for lifetime predictions. To obtain new data on the properties of 3C-SiC samples after cycling, the post-mortem analysis was carried out using the methods such as Raman, SEM, XRD, and XPS.

The *ex situ* study of 3C-SiC anode was carried out using Raman spectroscopy (details are provided in Chapter 3, §3.2.3). The investigation of samples during several initial cycles did not reveal the change of crystal structure. Therefore, it was decided to register the spectra with a larger cycle number step. Fig. 39 shows Raman spectra of 3C-SiC before cycling, after 20^{th} and 200^{th} cycle (in the delithiated state). Starting from the 20^{th} cycle it was found, that the peaks around 965 cm^{-1} and 987 cm^{-1} become more intensive. Taking into account that the peak at 987 cm^{-1} is related to the second order scattering of Si (see Fig. 25), the increase in intensity can be explained by changes in Si wafer upon the interaction with Li^+ ions. However, the reason for intensity increase of the peak at 965 cm^{-1} requires further studies. We suppose that it could be related to reaction which caused the fracture of SiC heated with lithium above 225 ˚C (Fig. 34).

SEM was used to study the morphology of the surface and cross sections of the 3C-SiC thin-film electrode before and after electrochemical cycling (delithiated after 200 cycles). Fig. 40a,b show the morphology of the 3C-SiC surface at various magnifications after charge-discharge cycling. Comparing with the SEM images of the pristine samples shown in Fig. 28, it can be noted that, in general, the appearance of the surface did not change much after cycling (Fig. 40a, b).

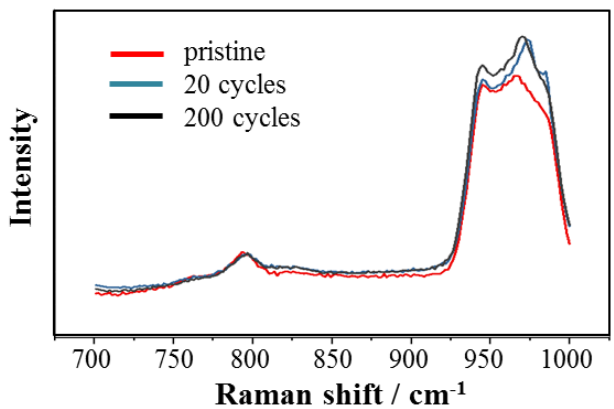

Fig. 39 Raman spectra of 3C-SiC before cycling, and after 20th and 200th cycle.

From Fig. 40a,b the hemispherical formations and straightly elongated grooves still can be observed on the surface. No mechanical failure or delamination of the thin film can be notice. Fig. 40c shows the cross-section of a cycled sample taken at the center of the 3C-SiC anode. It can be seen that the 3C-SiC thin film remained almost intact after the many cycles of lithiation and delithiation. Fig. 40d shows the cross-section image taken at the edge of the cycled sample where the significant damage of Si substrate with ubiquitous cracks can be observed, while SiC film remained almost unharmed. The cracking of Si wafer from the edge can be explained by its intensive reaction with the Li^+ ions.

Fig. 41 illustrates the XRD spectra of 3C-SiC thin film on Si substrate before and after 200 cycles (delithiated). In the right side insets, the crystal restructuring was not observed in the 3C-SiC film. On the contrary, Si had a peak shift to the right side indicating the changes happened in its crystal lattice after electrochemical

cycling. Considering the XRD results for Si presented in Fig. 31c, it can be detected that the changes during thermal alloying and electrochemical cycling have the same trend; in particular, the occurrence of new peak looking like a shoulder can be seen in Fig. 31c.

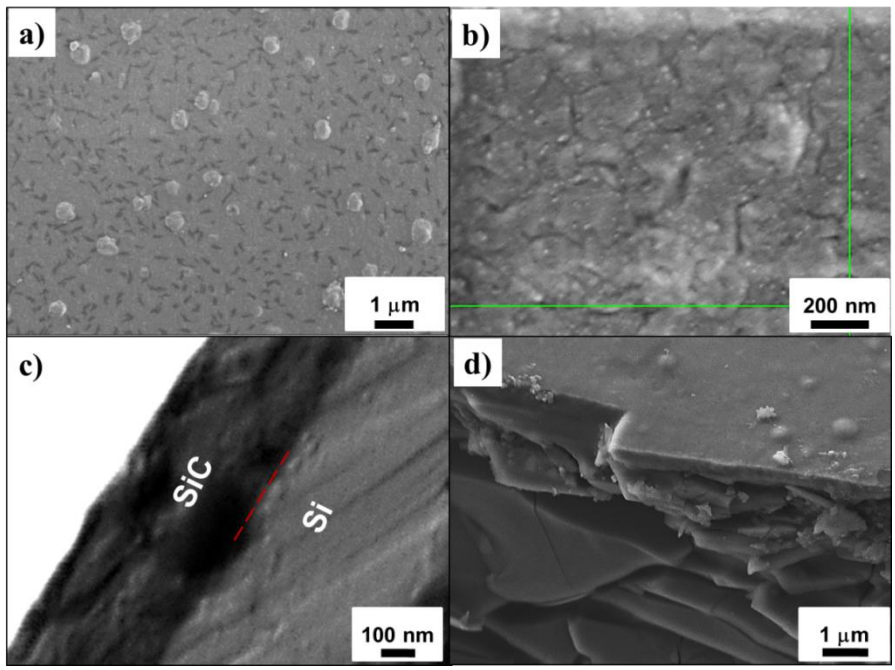

Fig. 40 SEM images of 3C-SiC after cycling (a,b) top surface and (c) cross-section in the middle of sample; (d) the edge of sample.

Fig. 42 presents the results of XPS study of 3C-SiC samples after cycling. The investigation focused on measuring the Li content on the 3C-SiC surface after the 1st lithiation implemented at a slow current density of 10 μA cm^{-2}. Among other things, the presence of a large number of other diverse elements was observed on the scans, which is a result of the presence of traces from the SEI layer. The significant Li peak on the sample surface after lithiation was observed at 56.5 eV; however, after milling the sample, it became relatively weak. This observation indicates that Li is more concentrated on the surface than in the bulk of the material, in spite of the fact that the dimensions of Li^+ ions (radius R= 0.74 Å) is less than both in-plane (a||) and out-of-plane (a⊥) lattice parameters for 3C-SiC (a|| = 4.3639 Å and a⊥ = 4.3555 Å).

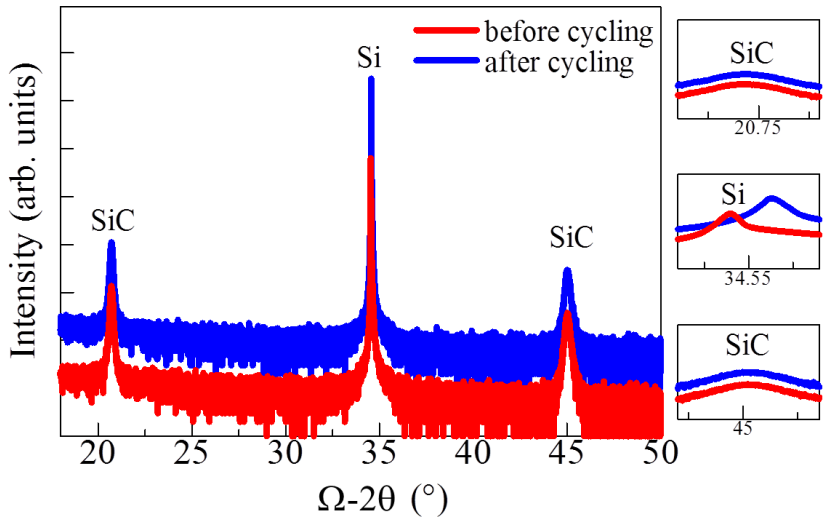

Fig. 41 XRD spectra of 3C-SiC before and after cycling.

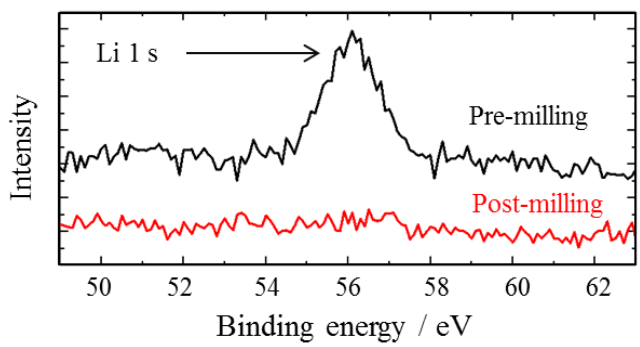

Fig. 42 XPS spectra of 3C-SiC after cycling before and after milling.

4.7 Summary

In this chapter, the study on the ability of 3C-SiC to interact with lithium was presented. The "single" particle results showed the electrochemical activity of 3C-SiC in this case. SEM and TEM analysis revealed mechanical stability after electrochemical cycling. XRD and Raman confirmed that there are no significant structural changes of 3C-SiC after the heat-treatment with lithium and during electrochemical lithiation and delithiation. XPS of samples after full lithiation showed that Li^+ ions were concentrated in the near-surface layers of 3C-SiC.

This can be explained by the two possible reasons. Firstly, the observed activity of the 3C-SiC can occur as a result of the Li^+ ion in the near-surface layers. From the other hand, such behavior can also be due to the capacitance when there is no charge transfer in the material. In both case, the further study are requires. The capacity values obtained for 3C-SiC are rather low and comparable to the capacities achieved by commercially successful anodes based on graphitic materials. Besides, even this fact cannot make 3C-SiC to be competitive with conventional anode materials in LIBs to power the energy-consuming portable electronic devices and electric vehicles.

However, the use of 3C-SiC can be quite convenient and commercially rational in microbatteries that do not require significant energy. Moreover, epitaxial growth of 3C-SiC directly on Si substrate can be easily integrated with the processing technology of electronic microdevices due to the fact that the processes of creating electronics have been already scaled and automated.

5 PREPARATION OF SUBSTRATES FOR SI THIN FILM ANODE

5.1 Introduction

Substrate for LIB electrodes plays an essential role due to it has to collect and conduct electrons released during the reactions, therefore, the electrode's substrate is called current collector (CC). Another requirement to CC is a provision a good adhesion for electrode materials. In the case of alloying anode materials such as thin film, the problem appears when Si expands several times after lithiation leading to the loss of the bonding with CC following by the delamination of active material. That is why the design and preparation of the substrate is an important step in the improvement of the anode performance.

As it was noticed in the Introduction (Chapter 2), the appropriately chosen and/or designed substrate can improve the mechanical and electrochemical stability of Si thin film anode. The substrates roughened prior to Si deposition was reported to enhance adhesion of Si film as well as increase the surface of the film which resulted in the rise of the current rate delivered by battery cell. For this reason, within a framework of the dissertation, the preparation of the porous Cu substrate has been performed.

Another alternative approach was performed for the preparation of large surface graphene sheets. GF can be used as an active anode material with a low discharge potential and a high theoretical specific capacity that was mentioned in Chapter 2 (§2.4). Inspired by previously reported works [190], we made the attempts to grow GF as a substrate playing the role of the electrical conductor for Si thin film and the electrochemically active anode material simultaneously. Besides, GF experiences an intercalation mechanism of Li^+ ions insertion meaning that it can act as a buffer stress suppressor for Si film during the volume change of the latter. Finally, a growth of GF on a 3D substrate was performed in order to develop compositional Si-GF electrode.

5.2 Preparation of porous substrates for Si thin film

As it was noticed in the Introduction chapter (Chapter 2), the appropriately chosen and/or designed substrate can improve the mechanical and electrochemical stability of Si thin film anode. The substrates roughened prior to Si deposition was reported to enhance adhesion of Si film as well as increase the surface of the film which resulted in the rise of the current rate delivered by battery cell. For this reason, within a framework of the dissertation, the preparation of the porous Cu substrate has been performed.

A commercial Cu foil with a thickness of 9 μm and 99.99% purity (MTI corp.) was used as reference planar and rough substrates for thin film deposition since one side of the foil is polished, and the other side is rough.

A porous substrate was prepared from the same Cu foil (polished side) using the procedure based on an etching by ammonia solution. This method was utilized for the growth of Cu nanowires on 25 μm thick Cu surface by Yang et al. [191]. In order to obtain a desirable porous structure, some modifications were made into a procedure since Cu foil used in our work was thinner and tended to be destroyed at the longer etching times.

The preparation of the porous substrate is shown schematically in Fig. 43. The Cu foil was cleaned in the acids mixture HNO_3+HF+H_2O and rinsed by deionized water (DIW). Then the Cu foil was immersed into an ammonia solution (5%) for 23 hours. As a result of a chemical reaction, the copper hydroxide was formed on the foil surface. After the etching, the foil was thermally treated in a tubular furnace STF 1200 (Across International, USA). The sample annealing was carried out in two steps: dehydration at 180 °C and reduction at 300 °C. The Ar + H_2 (5%) gas flow was kept at a constant level of 150 cm^3min^{-1}. Finally, the residues of the etching products were easily removed from the surface and pores by ultrasonication for 10 min followed by rinsing in DIW and drying for 60 min at 60 °C [86].

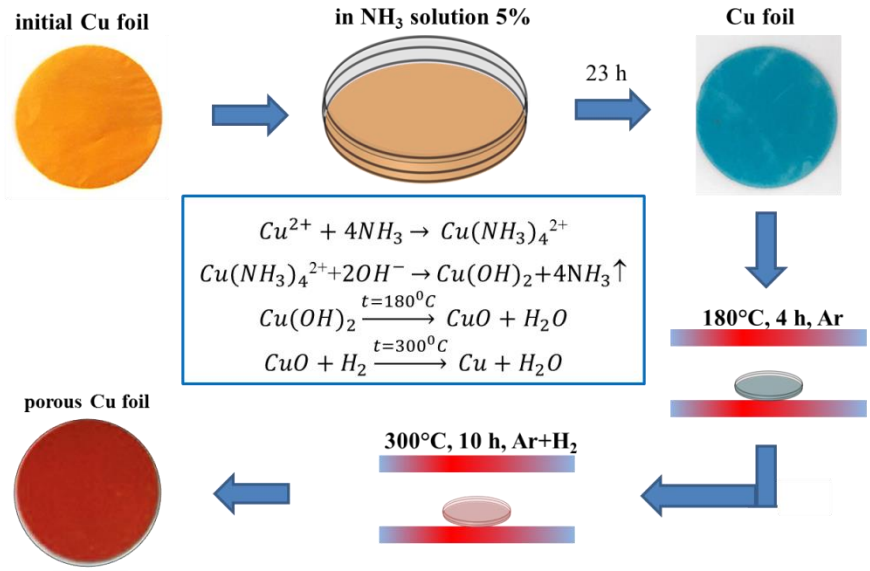

Fig. 43 Schematic procedure for porous Cu foil preparation.

SEM images below describe the morphology and structure of the Cu substrates. Fig. 44 illustrates the top-view images of Cu substrates with different surface conditions. The smooth surface for the flat Cu foil (Fig. 44a) and hill-like formations on a surface of the rough foil (Fig. 44b) can be observed. Fig. 44c demonstrates the porous-like structure of the obtained CC. This resulting network with the microscale ledges and caves is caused by the reaction between Cu and ammonia solution within the original solid structure; a slightly rough surface of the sample can be detected on the inserted image at higher magnification. The dimension of ledges of the substrate's surface are is within 1-5 μm, while the caves have a bit wider sizes. The analysis of porosity of the as-prepared porous samples showed the average size of pores of around 3 nm, which indicates that the main porosity does not locate in a deep bulk but mostly on the visible surface.

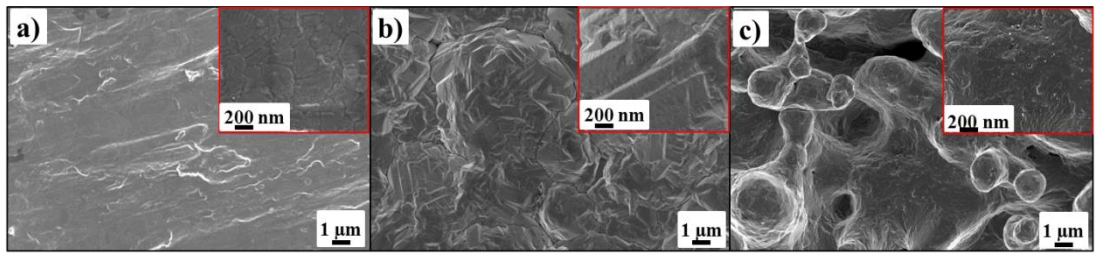

Fig. 44 SEM images of (a) flat, (b) rough and (c) porous substrates.

5.3 Growth of graphene on the surface of liquid gallium

50 g of pure liquid Ga was placed into a crucible inside a glove box filled with argon. The surface of Ga was covered by a thin layer of cyclohexane (C_6H_{12}) to protect its top layer from oxidation during the transportation into the furnace. C_6H_{12} evaporated during heating at 100 °C and flew away with argon. Since C_6H_{12} is also a carbon-contained substance, the first experiments were carried out to investigate its role as a carbon precursor. The second batch of the experiments was done with methane (CH_4) as a precursor, and the third experimental series was to investigate the capability to the secondary use of pre-treated Ga without precursors.

A high temperature split tube furnace was used as a reactor to GF synthesis. A detailed sequence of the experiments was as follows: the crucible with catalyst was placed in the middle of the furnace which was first heated to 200 °C and annealed for 30 min to remove all gas residues. Then the furnace was heated to 1000 °C with a heating rate of 10 °C min^{-1}. For the experiments with methane, the mixture of the gases Ar + CH_4 (7%) was supplied into the furnace for 30 min at this temperature. The flow rate of gas mixture was 100 cm^3min^{-1} throughout the experiments. The cooling occurred naturally. The technical conditions of experiments with cyclohexane and pre-treated Ga were identical to the procedures described above, but without methane supply in both cases. The dark film was formed on the surface of pure Ga with cyclohexane and methane as well as on the surface of the pre-treated Ga after experiments as it can be seen from Fig. 45 below.

Fig. 45 Catalyzed carbon film on the surface of pure liquid Ga.

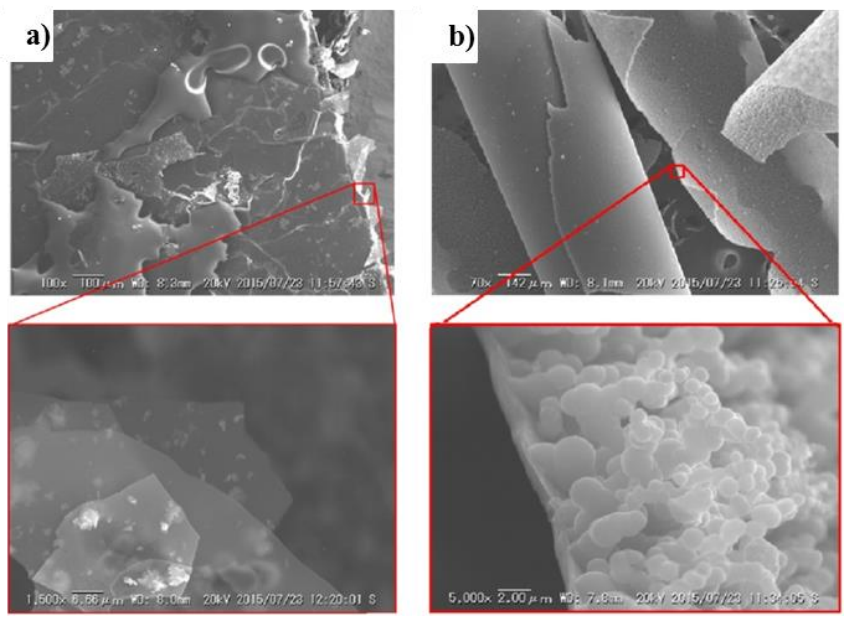

Fig. 46 SEM images of (a) the graphene from the surface of a catalyst;
(b) carbon from the crucible wall.

The transfer of the GF was slightly modified in comparison with that described in the literature mentioned above. The top layer of GF was protected from breaking with the capping of the carbon film surface by polymethyl methacrylate (PMMA, 5%). Before application of the PMMA coating on the surface of the carbon film, Ga was frozen in a refrigerator at -30 °C for several hours to avoid rupture of the carbon film during operation and to obtain carbon film with a greater surface area. After drying of the PMMA layer in an oven ELF 11/14 at 60 °C for 5 h and gradual

thawing of catalyst, the detachment of the film from the Ga surface was done mechanically with its careful transfer on the glass substrate. Then, the film with PMMA coating was again placed in the oven for 2 hours vertically to let the rest of Ga droplets to roll off the surface. Then, the residual amount of Ga was etched in HCl solution (18%) for 2 hours. PMMA layer was removed carefully with hot acetone (80 °C). Eventually, GF was rinsed in distilled and DIW [192].

At the initial stage, SEM investigation of the samples obtained with C_6H_{12} and collected from the surface of Ga and from the surface of crucible were made with the purpose to see the difference between their structures. The results are shown in Fig. 46. One can see that morphology of the sample from Ga surface and the sample from the surface of crucible had significant differences. In Fig. 46a the distinct transparent layers with some inclusions can be observed. The thickness of the layers is a few nanometers only. The image (Fig. 46b) demonstrates that the sample collected from the surface of a crucible is a layer with much higher thickness, which is more than several hundreds of nanometers. This film has a non-homogeneous structure and comprised of many connected spherical particles. These data allow a suggestion that Ga exhibits catalytic properties and provides an opportunity to obtain a very thin carbon material on its surface.

Raman spectroscopy is one of the most effective methods for determination and characterization of carbon materials. There are the typical peaks of graphene, the so-called G band, appearing at 1582 cm^{-1} and the 2D band at about 2700 cm^{-1}. If the graphene sample has disorders or laser focuses on its edge, the D-band occurs at about half of the frequency of the 2D band (around 1350 cm^{-1}) [193]. From Raman spectra shown in Fig. 47, for the graphene samples obtained on the surface of pure Ga with methane supply (the internal side of the carbon film faced to the catalytic surface) the spectrum of the Raman shift (Fig. 47a) shows the presence of the D band at 1350 cm^{-1}, the G band at 1580 cm^{-1}, 2D band at 2700 cm^{-1}. Actually, for graphite, there are two bands ($2D_1$ and $2D_2$) near the Raman shift of 2700 cm^{-1}, while in our spectrum single 2D peak persists. The presence and high intensity of the D band points on the disorder of structure and/or the presence of defects in the sample. For

single and bi-layer graphene a ratio of the intensities of the 2D to G bands is more than 3 in accordance with literature data [194]. Our obtained spectrum has the 2D/G ratio of around 0.5. An estimation of the exact layer number based on the calculation of this ratio is argued. Anyway, the ratio lower than that mentioned above for single and bi-layer graphene can help to suppose that we have obtained multilayered graphene. The full-width half maximum (FWHM) of the G band for single layer graphene is within 20-30 cm^{-1}, while the FWHM of the same band for four- and five-layer graphene is over 70 cm^{-1} [195]. In our spectrum, the magnitude of FWHM equals 91 cm^{-1}. Thus, the analysis of the D, G, 2D bands' features in Raman spectra of the carbon film, synthesized on the Ga surface, allows supposing that the samples are multilayered graphene with disorders. Raman spectrum on the internal side of pre-treated Ga is identical to the spectrum in Fig. 47a. The top side of the samples (external side) was also investigated by Raman spectroscopy, and the spectrum shown in Fig. 47b. Existing of shifted G band and a very wide 2D band points on the amorphous phase of the top side [196].

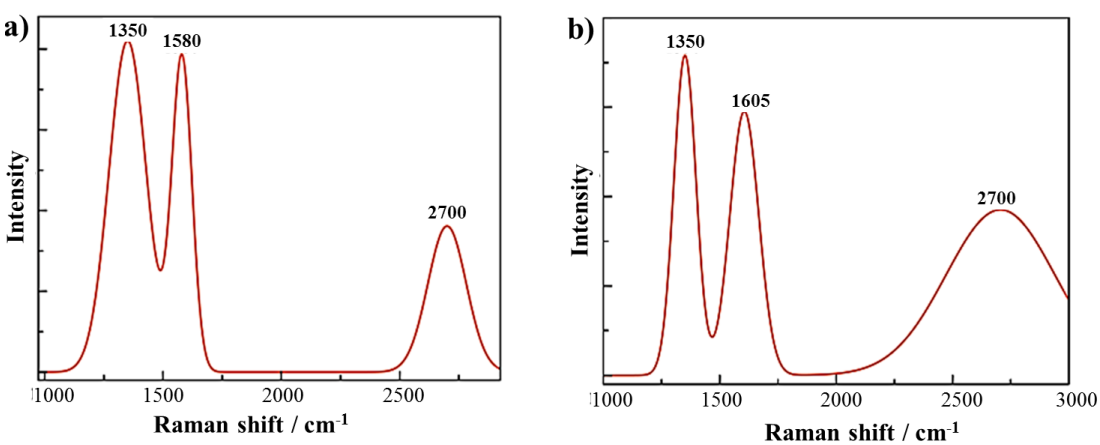

Fig. 47 (a) Raman spectrum of the internal surface of the carbon film (faced to Ga); (b) Raman spectra of the external surface of the carbon film.

TEM was used to investigate graphene microstructure. The TEM image of the sample from the Ga surface is shown in Fig. 48. It can be seen that the synthesis resulted in a thin layered structure with several hundred nanometers dimensions.

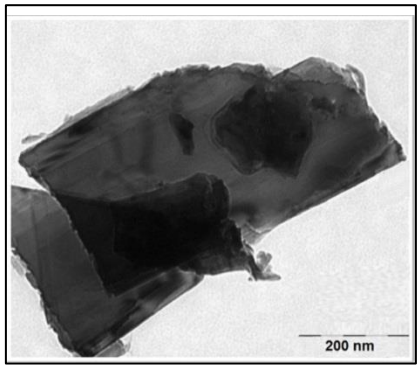

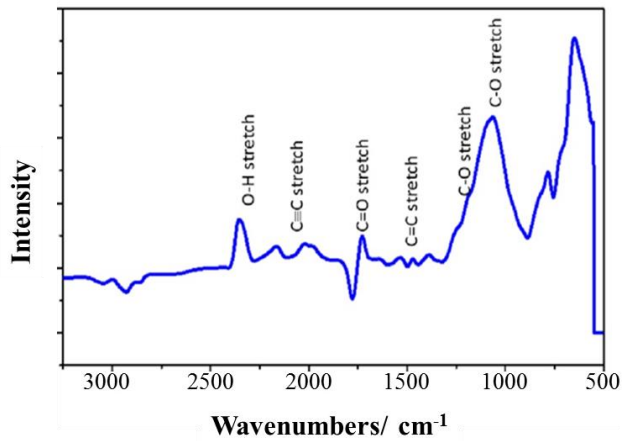

Fig. 48 TEM image of graphene.

Fig. 49 FTIR spectra of the carbon film.

FTIR spectroscopy is the method for the material analysis, in particular for identification of chemical bonds. Usually not graphene, but graphene oxide is investigated by this technique. On the other hand, this technique can give an opportunity to control the purity of synthesized material. In the FTIR spectrum of the graphene sample growth on the Ga surface (internal) (Fig. 49) the following peaks are taking place: C=C peaks around 1600 cm^{-1}, C=O stretching of carboxylic and/or carbonyl moiety functional groups at 1730 cm^{-1} and 1630 cm^{-1} respectively, the C–O stretching vibrations at 1226 cm^{-1} [197,198]. As can be understood a significant amount of oxygen persists in our sample. Its presence describes the disorder of graphene that found a reflection in the high intensity of the D band in the Raman spectrum (Fig. 47

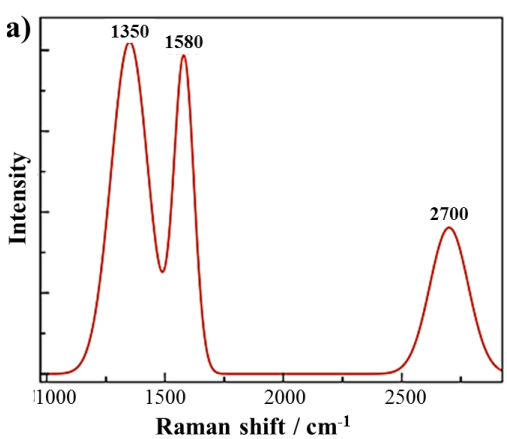

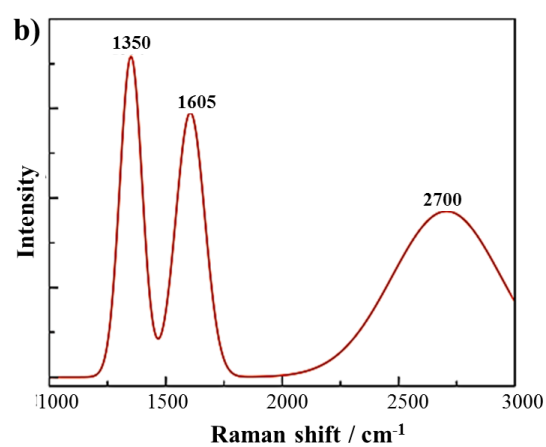

Fig. 47).

To sum up this part, the catalytic properties of Ga in respect to carbon atoms were demonstrated. Three different series of experiments were carried out. In all cases, the dark thin carbon films on the Ga surface during experiments formed. According to the features of the G, 2D, D bands in the Raman spectra, the internal sides of the carbon film samples, obtained on the Ga surface with CH_4 as a precursor and on the surface of pre-treated Ga, have a hexagonal structure with sp^2-hybridization related to the multilayered graphene. The intensive D band corresponds to the disorder and/or the presence of impurities. Particularly, FTIR characterization has approved this, showing the significant presence of oxygen in samples. The obtained graphene film on the pure and pre-treated Ga surface appeared to be identical according to Raman spectra. Besides, the top side of carbon film (external) appeared to be amorphous. It can be supposed that graphene growth on the Ga surface limited by several layers after that the amorphous phase starts to form. Microscopic investigations by SEM, TEM have demonstrated the layered structure with disorders. Therefore, further experimental investigations will be aimed at the improvement of the morphology and purity of graphene.

The secondary use of the catalyst is important in the point of view of the rationalization of the synthesis process in the future. Regarding the evaporation of Ga atoms, the significant mass loss was not observed after experiments. Most likely, the GF film protects the Ga atoms on the surface from evaporation. Thus, liquid Ga can be used and recycled many times. Unfortunately, a use such GF substrate for Si thin film was not found to be applicable due to the small amounts and low surface of GF sheets.

5.4 Preparation of graphene coated Ni foam

Ni foam served as a 3D substrate for the GF growth and for the Si film deposition. Ni foam was purchased from Goodfellow Inc. and had the following parameters: the thickness of foam was 1.6 mm, the porosity of more than 95% with

the mean hole diameter of 0.22 mm.

The CVD growth of GF was implemented onto Ni foam, a 3D interconnected substrate. Ni is known for its catalytic activity towards carbon atoms facilitating them to arrange into a hexagonal lattice in the spaces between Ni atoms [199]. Ni foam is able to produce defect-free GF layers as it was reported before [190] with an increased surface area of the sheets. Prior to CVD, heat treatment of Ni foam was carried out in the STF1200 furnace in a mixture of Ar and H_2 (5%) with preheating at 200 °C during 30 min to remove the moisture from the catalyst surface and further at 1020 °C to remove the rest of contaminations and to reduce the native NiO layer to Ni. After this, the precursor gas, a methane-containing gas mixture Ar + CH_4 (7%), was injected into the furnace. In order to obtain a few layer GF, the inlet of gas lasted for 5 min at the ambient pressure. Carbon atoms precipitated at the surface of Ni and segregated during cooling forming a high quality few layer GF [200]. The experimental conditions are summarized in Table 3. The mass increment of samples was controlled using weighting by an ultra-microbalance and constituted around 0.41 ± 0.02 mg cm^{-2} and almost equal for all samples. Prior to CVD and magnetron sputtering all Ni foam samples were cleaned by diluted HCl (1:1, v/v), followed by rinsing with DIW.

Table 3 – Technical conditions of CVD processes of graphene growth.

Gas	Gas flow	Precursor	Steps			Cooling
			Annealing	Annealing	Deposition	
$Ar + H_2$ (5%+ 95%)	100 cm^3min^{-1}	CH_4 + Ar (7%+93%)	200ºC, 60 min	1020 ºC, 60 min, 300 cm^3min^{-1} ($Ar+H_2$)	1020 ºC, 5min, 220 cm^3min^{-1} ($Ar+CH_4$)+300 cm^3min^{-1} ($Ar+H_2$)	Naturally

Fig. 50 shows the Raman spectra of the grown carbon film which was measured at different points of the sample. All three spectra display similar scattering

patterns presented by two peaks at around 1579 cm^{-1} and 2696 cm^{-1} assigned to the G and 2D bands of carbon materials, respectively. A missing D band (~ 1320 cm^{-1}) evidences a high purity and well-ordered structure of the synthesized GF. In order to determine the number of the graphene layers, the spectra were analyzed in the same way as in previous paragraph for GF sheets grown on Ga surface.

The records of scattering response from three different points on GF on Ni foam have resulted in various intensities consequently leading to various 2D/G ratio from 0.75 to 3.2. As it was already mentioned above, for a monolayer of GF, a FWHM constitutes 20-30 cm^{-1}, while for four and five layered graphene this value is around 70 cm^{-1} [195]. The calculated FWHM for our sample is within a range of 20 – 80 cm^{-1}. Thus, according to Raman spectroscopy plots, we can suppose that the carbon film synthesized on Ni foam is a few layered GF with high purity and quality.

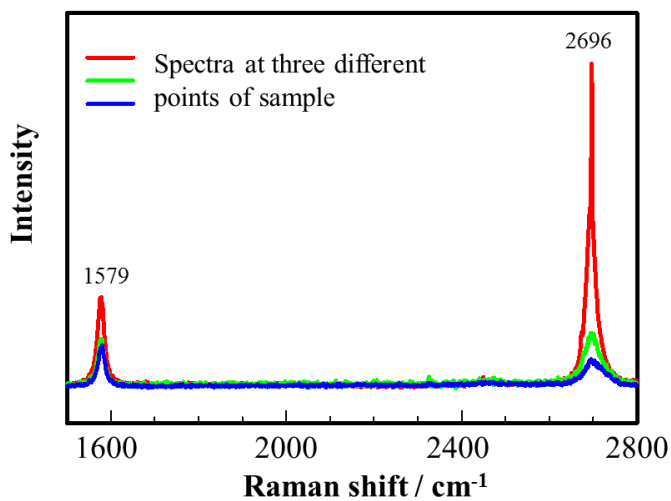

Fig. 50 Raman spectra of GF on Ni foam.

The microstructural morphologies of the as-prepared samples were revealed by SEM. The results of these studies are presented in Fig. 51, which demonstrates the surface of Ni foam and its cells walls/wires after cleaning with acetone. In higher resolution images, incorporated into Fig. 51a,b, one can see the distinguishable surface grain boundaries. Fig. 51c,d illustrates the sample after CVD, on which a

dark film, consisting of numerous GF sheets, can be detected on the Ni foam surface. GF layers replicate the shape of boundaries over the Ni foam surface.

The SEM/EDX scans demonstrate the surfaces of as-deposited GF-Ni samples and the C and Ni elements distribution map (Fig. 51e). It can be seen that carbon and nickel are uniformly distributed in the sample. In the EDX results, only C and Ni peaks could be recorded. From the distribution map of carbon, one can see some dark spots with no carbon, which might be an indication of delamination of GF sheets from the substrate within these spots.

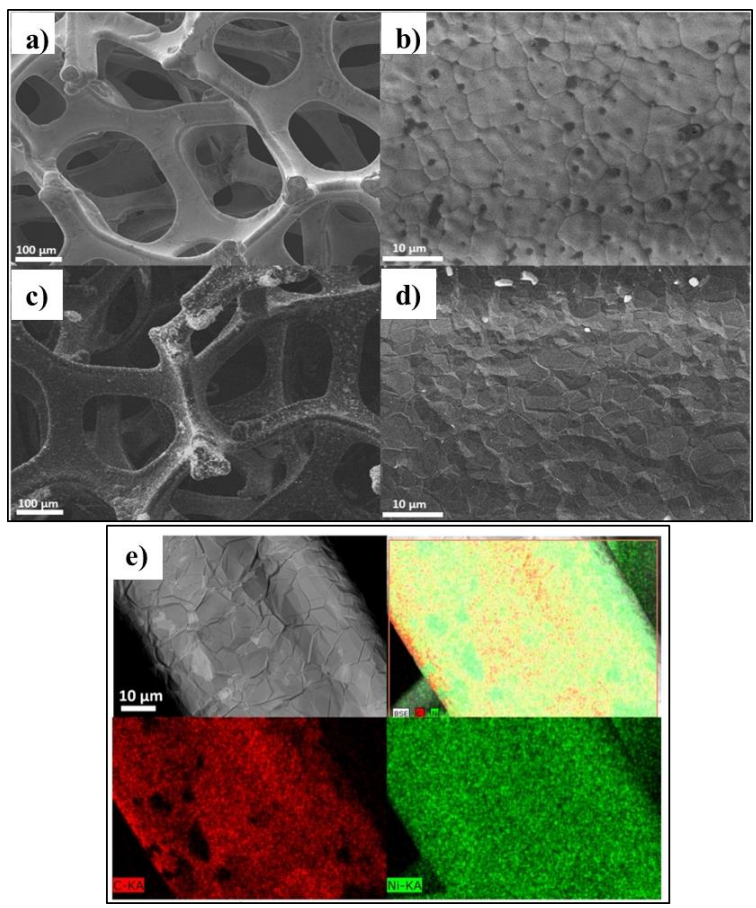

Fig. 51 SEM images of (a-b) Ni foam, (c-d) GF-Ni foam and (e) EDS of GF-Ni foam.

6 DESIGN OF SILICON THIN FILM ANODE

6.1 Introduction

This chapter comprises the results on design and study of amorphous Si thin film anode prepared by means of magnetron sputtering. The general information on the reasons and aims of this research were given in the literature review (Chapter 2, §2.4). The Si thin film was deposited on several types of current collectors in order to reach the energy increase and improve a battery cell performance. The effects of the surface condition, dopants incorporation, and the addition of electrolyte additive were investigated. Below, the results of studies are presented, including synthesis method, characterization results obtained by various techniques, analysis of electrochemical test data and discussion.

6.2 Silicon thin film deposition

Magnetron sputtering method was chosen for the deposition of Si onto the various substrates because this method allows for obtaining the amorphous phase Si. LAB-18 Magnetron Sputtering System (Kurt J. Lesker Inc.) was used. During sputtering, an undoped (>1 Ω·cm), *p*-type doped (0.005-0.020 Ω·cm), *n*-type doped (<0.1 Ω·cm) Si targets (99.999%, Kurt Lesker Inc.) were hit by Ar^+ plasma generated between two magnets. This process led to the emission of target atoms and their deposition on the substrate. The main advantage of MS is easiness of the process along with a capability to get an amorphous Si with high purity, as well as easy control of film thickness. The synthesis conditions were chosen based on the literature data. In particular, the power mode (*rf*) and magnitude of 80 W employed in this work were taken over from [61] where an optimal power to prepare Si thin film with the certain density and low oxygen content was optimized. The sputtering was carried out at the angle of 30° in order to ensure that the target atoms might be able to reach the innermost whisks of the porous substrates. The mass increment of Si was determined by weighing the samples before and after sputtering by an ultra-microbalance and constituted within 0.07 – 0.09 mg.

Table 4 – Technical conditions of MS processes for deposition of Si thin film.

Gas	Pressure&Temperature	Target	Power	Rotation	Time	Post-annealing
Ar 99%	5 mTorr, 25 ºC	Si (99.99 %), undoped, *p*-type, *n*-type,	*rf*, 80 W	5 rpm	60 min	150 ºC - 60 min, 300 ºC - 60 min, 150 cm^3min^{-1} ($Ar+H_2$)

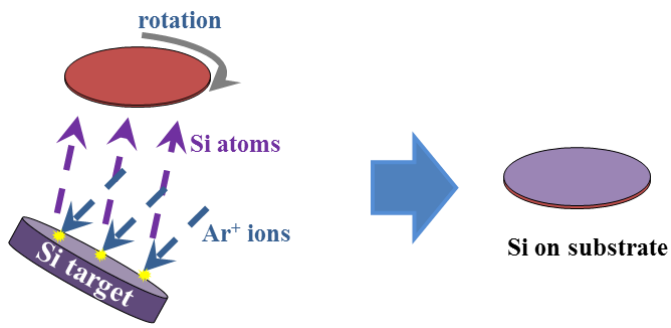

Fig. 52 Schematic view of Si thin film deposition process by MS.

Before assembling the cells, the materials were annealed in a mixture gas Ar + H_2 (5%) (the flow rate of 150 cm^3 min^{-1}) in a high temperature tubular furnace at 150 °C for 60 min in order to remove condensed moisture from the surface, and then at 300 °C for 60 min in order to remove oxides (see Table 3). It was reported [38] that such heat treatment strengthens the adhesion at the Si-substrate interface Si film that positively affects the performance of the batteries.

6.3 Characterization, electrochemical test results, and discussion

6.3.1 Study of the effect of surface condition on Si thin film cycling performance

Before the electrochemical cycling, the Si thin film was characterized by various techniques for the identification of the crystal structure, topological properties, and material morphology. The AFM imaging is shown in Fig. 53a-c. The

plot in Fig. 53a,b illustrates the 3D image of the film edge and the height profile of Si thin film deposited on the polished glass, respectively. The Si film thickness values were checked for several chosen points at the edge of Si thin film and found to be of around 350-400 nm. It worth to notice, that on the different substrates the thickness was not absolutely uniform and varied within 200 – 500 nm. On the base of AFM profiling, the average roughness of Si thin film surface also was estimated to be within ± 25 × 25 nm (width×height).

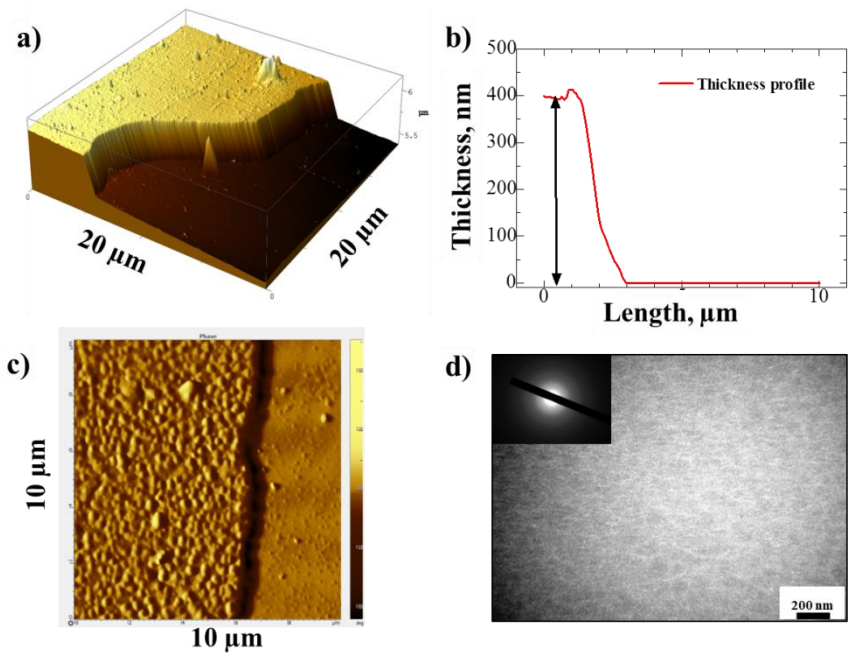

Fig. 53 (a) 3D AFM image of Si film (b) the AFM height profile, (c) AFM top-view image. (d) TEM image of Si thin film.

Fig. 53d shows the TEM results of the structural analysis of Si thin film; according to the image, the obtained Si thin film does not exhibit the crystal patterns indicating completely amorphous phase.

SEM was used to describe the morphology of the Si thin film. Fig. 54a-i illustrates the top-view images of Si thin films deposited on the various substrates acting as current collectors (CC). From the first view, it can be seen that the thin film

tends to repeat the substrate structure in each case. For the porous Si sample, the thin film fills the pores (see Fig. 54g-i). From the images at higher magnifications in Fig. 54c,f,i, the spherical shape of the Si particles with the particle size up to ~ 100 nm can be observed, besides each such particle is kind of a cluster built by many smaller particles.

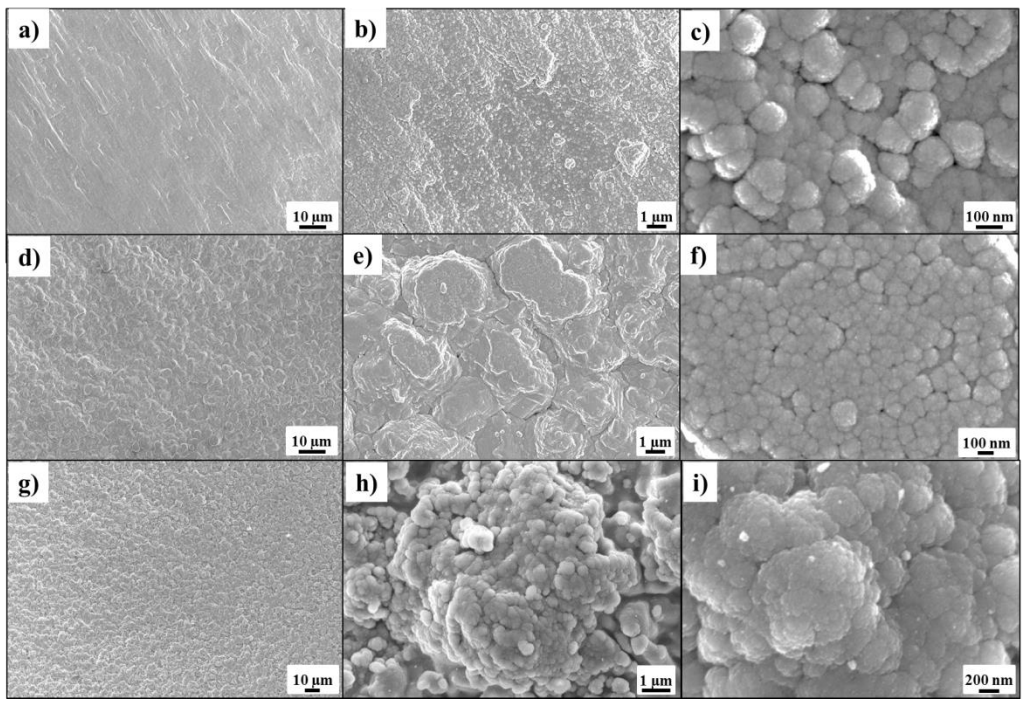

Fig. 54 SEM images of Si at different magnifications on: (a-c) flat CC, (d-f) rough CC, (g-i) porous Cu.

The responsible factor for spheroidal agglomerates originated from the force of Coulomb repulsion. Si particles, negatively charged, that able to overcome Coulomb repulsion, and minimize the surface free energy adopt the spherical shape. In other words, the particles grow by accretion, i.e., a collection of neutral or ionic species of atoms and molecules, leading to the growth of spherical particles. [201] Therefore, broccoli-like Si film comprises the separate clusters where the latter cannot accrete with the adjacent ones. The visible boundaries between the clusters probably can indicate the lowest surface free energy preventing further accretion. In fact, this observation differs from that for the 3C-SiC thin film, prepared by RP-CVD, where

crystallinity become more perfect due to neighboring grains can merge into a single crystal with time [180].

In order to evaluate the electrochemical performance of obtained Si thin film as the anode material, CV was used first at a scan rate of 0.1 mVs^{-1} in a potential range 0 and 3 V. As expected, all tested half cells with Si thin film anode demonstrated the similar lithiation/delithiation behavior on CV plots (Fig. 55a). Considering the first cycle scans, one can see that the initial electrochemical reaction happened at discharging potential of around $0.4 - 0.5$ V, which is usually ascribed to the decomposition of electrolyte on the Si electrode surface resulting in an SEI layer formation [202]. This process usually happens in the first initial cycles and then SEI layer remains on the surface being transparent for the Li^+ ions and simultaneously a barrier for electrons. The cathodic peaks at 0.1 V and 0.02 V indicate the first reversible lithiation reaction of Si and Li_xSi_y alloys formation. The corresponding delithiation reaction of Li_xSi_y back to Si takes place at the anodic peaks of 0.41 V and 0.53 V. Obtained peaks' positions are in a good agreement with the literature data for Si thin film anodes [33–35].

Fig. 55b-d illustrates the potential profiles of the investigated anodes recorded at a current density of 30 $\mu A\ cm^{-2}$ in the potential range of $0.1 - 1$ V. Observing the charge-discharge curves for the flat (see Fig. 55b) and rough (see Fig. 55c) Si thin films, we can detect the initial discharge capacities of around 1800 mAh g^{-1} and 2100 mAh g^{-1}, respectively. The SEI formation process and other irreversible reactions consumed the high amount of Li^+ ions in the first cycle. Therefore, the irreversible capacity loss constitutes around 500 mAh g^{-1} and 700 mAh g^{-1} for the flat and rough Si film anodes, respectively. From Fig. 55d for porous Si anode, we can observe that the initial discharge capacity increased up to 2200 mAh g^{-1}, and the irreversible capacity constituted around 800 mAh g^{-1}, which was the highest one within three tested investigated anodes. The increased irreversible capacity loss in the first cycle in case of the rough and porous could be due to an increased surface area of electrode. The extended surface area possibly contains a higher amount of Cu

oxide leading to the formation of higher amount of lithium oxide in the first lithiation that happens in parallel with the process of the SEI layer growth. This assumption can be confirmed by the noticeable plateau at 1.2 V (see inset in Fig. 55d), which corresponds to the reaction of Li^+ ions with Cu oxide with the reduction of CuO to Cu with the formation of Li_2O [203]. Considering Fig. 55b-d, one can observe that the charge capacity value is more close to discharge capacity for the porous Si thin film samples in contrast with two other indicating better capacity retention.

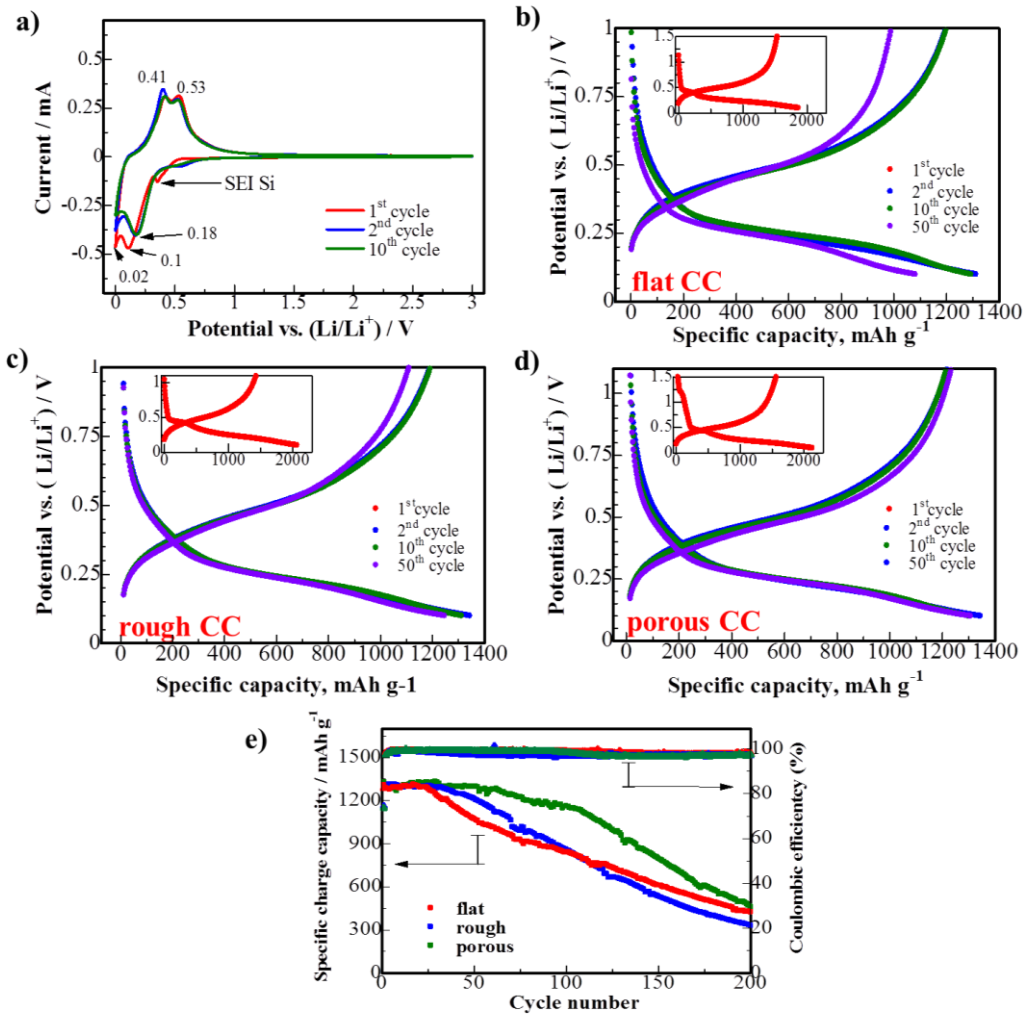

Fig. 55 Electrochemical test results (a) CV plot of Si thin film; (b-d) potential profiles of Si thin film anode (b) flat, (c) rough and (d) porous substrates; (e) cycling performance of the flat, rough and porous Si thin film anodes.

From Fig. 55e, the cycling performance of the investigated samples can be compared. The flat anode retained the stable charge capacity of around 1300 mAh g^{-1} during initial 25 cycles following by a gradual decrease up to 500 mAh g^{-1} in the 200^{th} cycle. The rough Si thin film showed the slightly better stability standing more or less constant up to 35^{th} cycle, after which the charge capacity also faded up to around 400 mAh g^{-1} in the final cycle. The a-Si film on a porous CC exhibited the obvious improvement in capacity retention. The designed porous Si anode retained the specific charge capacity within 1200-1300 mAh g^{-1} up to 110^{th} cycle and then had a slow climb down up to 500 mAh g^{-1} in the 200^{th} cycle. According to SEM images of Si on porous substrate (Fig. 44c), Si experienced the partial pulverization of the material. However, the remained Si film still can be noticed on the walls of ledges and caves indicating a good adhesion at the Si-substrate interface even after many cycles. The coulombic efficiency (CE) for the investigated Si thin film anodes is shown in the top part of Fig. 55e. CE values varied within 96.5 – 99.5% upon cycling for the samples.

Fig. 56a-c illustrates the post-cycling SEM images of the samples. The post-mortem investigations of the flat Si anode (Fig. 56a) revealed the extensive delamination of Si thin film from the flat substrate with the remained Si islands with the dimension of around 15 μm in length. One can see that the islands' edges do not touch the substrate indicating the electrical contact loss. From SEM images of the rough anode (Fig. 56b), it was detected that the sputtered Si thin film experienced the intensive cracking forming islands with approximately the same dimension as for Si on the flat substrate. However, the distances between islands are around a few microns and the edges of the islands were not spoiled in contrast with the first anode. The Si film deposited on the porous substrate shown in Fig. 56c did not exhibit the significant mechanical failure of the thin film. Despite the cracks and pulverization were noticed in the porous anode as well, no total delamination of film from the substrate was found for this type of anodes comparing to the flat and rough samples.

From the insets in Fig. 56c, Si particles can be noticed that Si is still on the walls of the ledges/caves indicating the improved adhesion at the film-substrate interface.

Thus, the increasing of the surface area of the substrate for Si thin film allowed enhancing significantly its performance in terms of cycle life with the improvement of the duration of stable cycling from 25 up to 110 cycles. That could happen owing to several reasons. First, the porous-structured substrate has accommodated the volume changes more effectively due to enough room for material 'breathing'. Secondly, the soft flexible structure of the porous substrate (~9 μm thick) allowed it bending together with the Si material during expansion/compression and, therefore, experienced less strain stress at the film-interphase region. Thirdly, the improved adhesion, formed due to the treated at nanoscale surface, mitigated the problem of the material delamination.

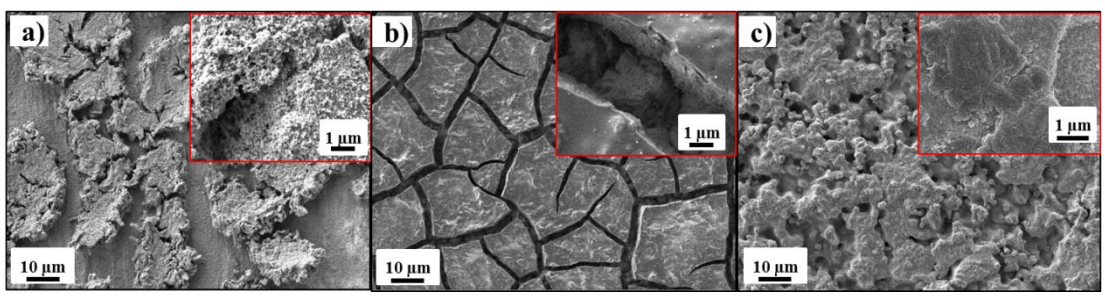

Fig. 56 SEM images of Si thin film anodes after cycling (a) on flat CC, (b) on rough CC and (c) porous CC.

6.3.2 Study of the doping effect on Si thin film cycling performance

The incorporation of dopants into the material can noticeably increase its electrical conductivity which is essential for the high mobility of the electrons in material bulk. It was reported in the literature that *n*-type Si thin film has a better cycling performance than *p*-type one [64]. Unfortunately, any graphical pieces of evidence or analysis of this fact were not provided. Therefore, this part of thesis research was devoted to the research of this phenomenon.

Three variously doped types of the Si thin film were sputtered on the porous CC, prepared as explained in Chapter 5, §5.2, and investigated by different characterization techniques before, during and after cycling.

Before electrochemical characterization, the investigation of electronic properties of Si thin film was performed (details Chapter 3, §3.1). Table 5 below provides the obtained data. From the table, it can be seen that the bulk and sheet carrier concentration is higher for doped samples, while the value for *p*-type Si is higher than that for *n*-type. It can be explained by the fact that the initial *p*-type target was doped up to higher levels (0.005-0.020 Ω cm) than *n*-type Si (<0.1 Ω cm). The results for resistivity, conductivity and mobility turned against the expectations. The resistivity was higher for the doped samples, while conductivity and mobility decreased. The strange behavior can be explained as follows. At low doping, the carrier concentration rises directly with doping concentration while the mobility reduces with doping hence the conductivity increases with the doping. At heavy doping, an increased fraction of the dopants does not experience ionization remaining inactive [204]. If the impurity content exceeds some limit, the dopants create the clusters in the material and the electron concentration stop to rise. These atoms do not behave as dopants (do not provide free electrons or holes) but as defects. This causes the additional scattering of electrons leading to a delay of mobility [205–207]. The obtained values of the conductivity in the Si thin film can be compared with the ones existing in the literature [208].

Table 5 – Electrical properties of the various doped Si thin film

Si type	Bulk concentration (cm^{-3})	Sheet concentration (cm^{-2})	Resistivity (Ω cm)	Conductivity $(\Omega\ cm)^{-1}$	Mobility ($cm^2V^{-1}s^{-1}$)
undoped	$3.5 \cdot 10^{18}$	$9.1 \cdot 10^{13}$	0.02	56.9	114.9
p-type	$6.5 \cdot 10^{18}$	$2.8E \cdot 10^{14}$	0.03	35.2	50.38
n-type	$4.9E \cdot 10^{18}$	$1.5 \cdot 10^{14}$	0.05	23.2	35.51

Fig. 57 below shows the results of the electrochemical test cycling of the undoped, *p*- and *n*-type Si thin film anodes on the prepared porous CC. The

galvanostatic cycling was performed within a potential range 0.01 – 1 V at the current density ~ 15 μA cm^{-2}. In order to check the ability of designed anode to deliver higher capacity, the lower cut off voltage was extended up to 0.01 V in a contrast with the test conditions of the results presented in the previous paragraph. Considering voltage profiles in Fig. 57a for undoped Si thin film, the main plateaus can be observed which corresponds to CV described in the previous section (Fig. 55a). The process of the SEI layer formation can be seen on the discharge curve as a slight tilt between the potentials 0.4 – 0.5 V. It also can be observed in the differential capacity plot (dQ/dV) (Fig. 57b) as a sharp looking down peak on 1st cycle curve positioned at 0.52 V indicating a new phase appearance at this potential. According to voltage profiles, undoped Si thin film anode delivered two times less capacity in the second cycle. It means that irreversible reactions in the first cycle consumed a high amount of Li^+ ions and electrons but did not return it back. The absence of the corresponding delithiation cathodic peak and no equivalent peak in the second cycle at 0.52 V in dQ/dV confirmed its irreversibility as well.

The rest of lithiation reactions can be seen as plateaus in the potential profiles and as down peaks in the differential plots at the around 0.25 V and 0.1 V with formation different Li_xSi_y alloys described in the Literature review (Chapter 2). During charging, the delithiation takes place when the formed alloys decompose onto lower ratio alloys and then separate Li and Si. The corresponding plateaus can be observed at around 0.3 V and 0.5 V in the cathodic (upper) part of dQ/dV plot (Fig. 57d). In fact, the potential profiles and the achieved capacity of around 1500 mAh g^{-1} are the same for undoped, *p*-type doped and *n*-type doped (Fig. 57a-c). The differences are in cycling performance which can be observed even up to 50th cycle in the potential profiles.

The capacity delivered by undoped Si anode is gradually decreasing up to 1402 mAh g^{-1} for the discharge and 1356 mAh g^{-1} for the charge in the 50th cycle. The *p*-type Si retained the capacities 1450 mAh g^{-1} and 1350 mAh g^{-1}, while the *n*-type Si exhibited 1510 mAh g^{-1} and 1482 mAh g^{-1} in the last cycle for charge and

discharge respectively. In other words, the initial capacity was almost the same for undoped and doped samples; however, the capacity retention behavior changed with time.

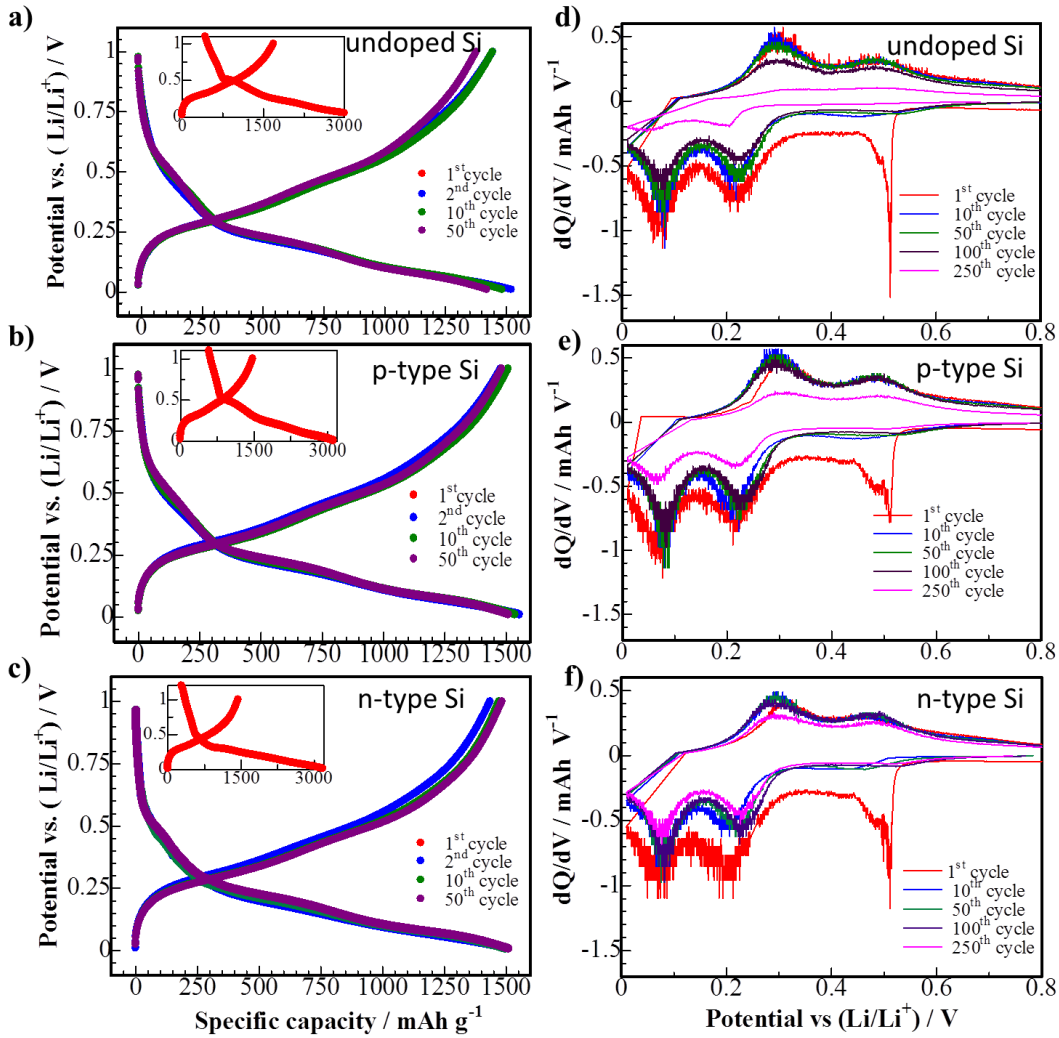

Fig. 57 (a-c) Potential profiles and (d-f) Differential capacity plots for variously doped Si thin film anode.

The same trend can be observed on dQ/dV plots (Fig. 57d-e) where the differential capacity for the undoped sample (Fig. 57d) significantly reduced in the 250th cycle indicating the weakening reaction and the low number of forming Li_xSi_y phase alloys. From Fig. 57e, the reaction still occurs in the 250th cycle for the *p*-type

doped Si, however, it is noticeably less than that in the 100th cycle. For the *n*-type doped Si thin film (Fig. 57f), the slight decrease in the differential capacity in the last cycle can be also observable but it is still high in contrast with two other samples.

Fig. 58 shows the performance of the samples upon the whole lithiation. From Fig. 58a, the better capacity retention can be seen for *n*-type doped as a consequence of the observed cycling features described above. The *n*-type doped Si anode exhibited stable capacity up to 170th cycle, after which it went down similarly to *p*-type and undoped samples.

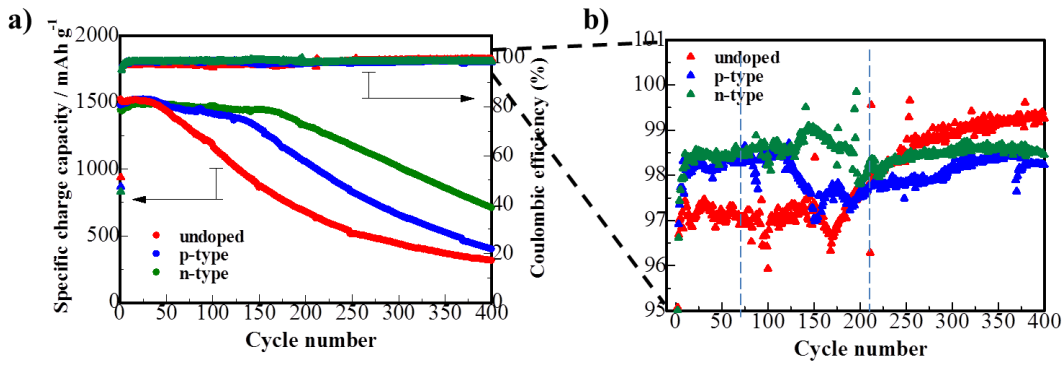

Fig. 58 (a) Cycling performance and (b) CE plot of variously doped Si thin film.

Considering the graph of the coulombic efficiencies (Fig. 58b), which is the percentage ratio of charge to discharge capacities, the *n*-type Si possesses the most stable CE and the highest value 98.5% up to 200th cycle. The CE of the *p*-type sample is similar with slightly lower values around 98.3%. However, the CE of the undoped sample had the lowest value of around 97.3%. After that, each material had the obvious CE fluctuations during the rapid capacity fading between 130-200 cycles. After that, the CE of the *n*-type sample returned to its initial average value; while *p*-type and undoped films exhibited the increasing of CE up to 400 cycles. The undoped Si thin film anode had the most significant increase of the CE up to 99.5% in the 400th cycle. It means that almost all Li^+ ions consumed in the discharge could be “recovered” during charging. Usually, the increase of CE over charge/discharge cycles is explained by the fact that SEI formation delays further parasitic reactions

and stabilizes electrode. Taking to account that speed of the capacity fading of undoped and *p*-type samples in the second half of cycling reduced (Fig. 58a), we can assume that CE significantly increased due to the material degradation 'finalization' and no new SEI formation occurred on freshly opened Si surfaces because of the material expansion.

Fig. 59 demonstrates the morphology of the samples after cycling. All of the samples experienced the significant capacity fading. On their surface, we can see the extensive net of cracks (Fig. 59a,c,e). From the magnified pictures (Fig. 59b,d,f), it can be seen that Si particles lost their initial spherical shape (see Fig. 54g-i) and the irregular morphology prevails in its bulk. Despite the post-mortem SEM images of variously doped Si films look nearly similar, the noticeable porosity can be observed in the both doped Si samples, while the undoped one does not show any porosity.

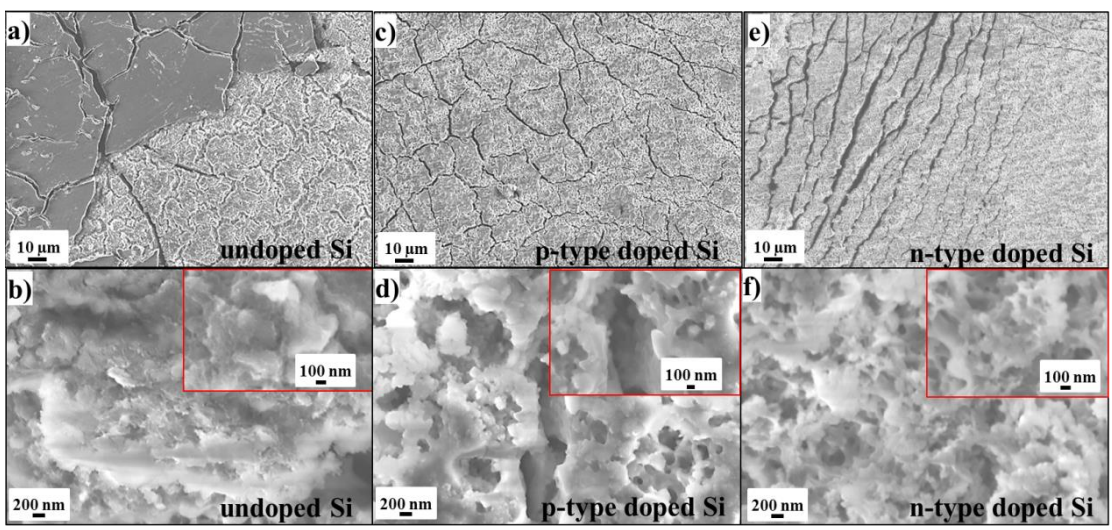

Fig. 59 Post-mortem SEM analysis of Si thin film after 400 cycles: (a,b) undoped, (c,d) *p*-type doped and (e,f) *n*-type doped.

Fig. 60 demonstrates the FIB/SEM images of *n*-type Si thin film before and after cycling. From the presented figures, Si expanded several times (Fig. 60c,d) from its original thickness (Fig. 60a,b). We can notice on the cross section the vertical cracks and a partial delamination of Si in the film-substrate interface after

cycling. In some places, the film is still well attached as shown, for example, in Fig. 60c (right part), while in other it was extensive detachment as can be seen in Fig. 60d. The images for the undoped and *p*-type film were registered to have absolutely the same features, therefore were not shown.

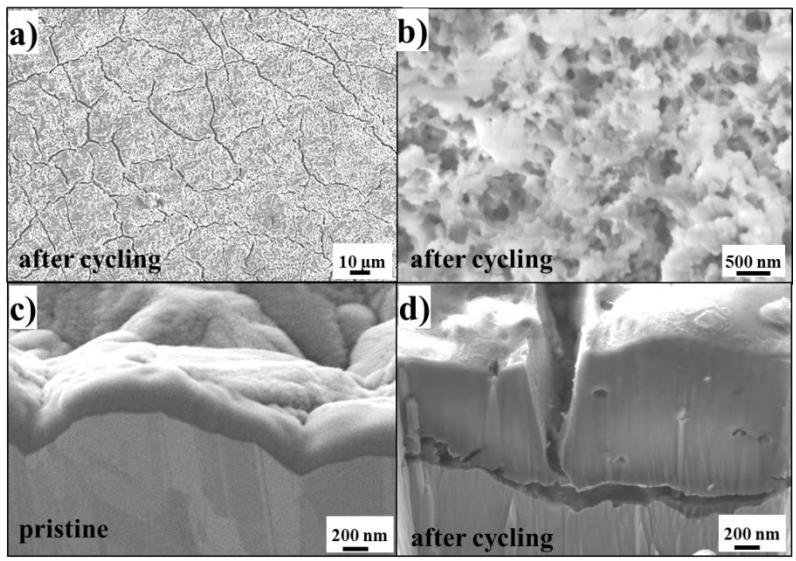

Fig. 60 FIB/SEM images of *n*-type Si thin film (a,b) before and (c,d) after cycling.

The Raman spectroscopy was used to characterize the samples before and after cycling. The scattering spectra of obtained Si thin films are shown in Fig. 61a. In general, the Raman spectra exhibits following peaks typically related to Si: the longitudinal optical (LO) mode of ~ 310 cm^{-1}, the longitudinal acoustic (LA) mode of ~400 cm^{-1}, the transverse optical (TO) mode at ~480 cm^{-1}, the overtone of the longitudinal and transverse phonons (2LA) at around ~630 cm^{-1}. The absence of the peak at 520 cm^{-1} and the broad shape of the main TO peak presence of these peaks allowed to conclude that the material sputtered on the porous substrate is pure amorphous Si [66].

From Fig. 61a (inset), slight differences in the sum Raman patterns were observed for undoped and doped Si films. To study the seemingly identical peaks in more detail, the Gaussian fitting was applied (Fig. 61b). One can see that the most scattering alterations in doped samples occurred at the LA, LO and 2LA bands. From

inset in Fig. 61b, we can observe the shift in the position of TO band of scattering for *n*-type doped Si to higher wavenumbers, while for *p*-type Si it shifted to the opposite direction. The LO and LA bands are also appeared to be shifted to the right side according to the fitting results for *n*-type Si. This can be explained by the presence of some amount of phosphorus dopant that usually has the most intensive scattering signal within a region 360 – 520 cm^{-1} [209]. The 2LA peak was registered to have wide left spreading for *p*-type doped Si film with the position at 634 cm^{-1} which is presumably due to the influence of the boron local vibrational peaks known to occur at the region of 550-680 cm^{-1} [210]. The similar features were recently observed by Yang et al. for pristine B- and P- doped crystalline Si nanowires [211], but for amorphous Si such analysis carried out for the first time.

Fig. 61c,d shows the equivalent spectra for the lithiated Si thin films which were distracted from the lithium cell after 2.5 cycles in lithiated state. Fig. 61c demonstrates the change of the sum curve, where it can be noticed that the curve above LA and LO bands of undoped and *p*-type Si experienced more significant variances. From Fig. 61d, after fitting of the spectra, we can see that almost TO, LO and LA vibrations modes were shifted to the higher wavenumbers and also an intensity ratio of the peaks changed in respect to each other. More probably, such behavior is caused by the formation of lithium silicates and lithium oxides the sign of which are usually seen at higher shifts [212–214]. The 2LA peak position, in the opposite, was moved in the back direction that is also due to the bands of lithium silicates at around 610 cm^{-2} [212]. The presence of lithium silicates in the lithiated Si anode after lithiation was confirmed by XRD pattern shown in Fig. 61e [33].

Table 6 summarizes the parameters which were extracted from the fitting curves of variously doped Si film in the as-deposited and after lithiation. It can be seen that after the lithiation the positions of peaks were changed significantly. The main TO peak increased for lithiated samples, and the highest climb was registered for the *p*-type sample. The shift of LO peaks also happened, and again it was more observed for the *p*-type Si, while for the *n*-type sample it was the lowest increase.

Considering LA peak, its big shift after lithiation was observed for both undoped and *p*-type samples. The last 2LA band decreased for undoped and *p*-type, however, slightly increased for the *n*-type sample. In general, the *n*-type Si experienced less shift comparing to undoped and *p*-type Si thin film anodes.

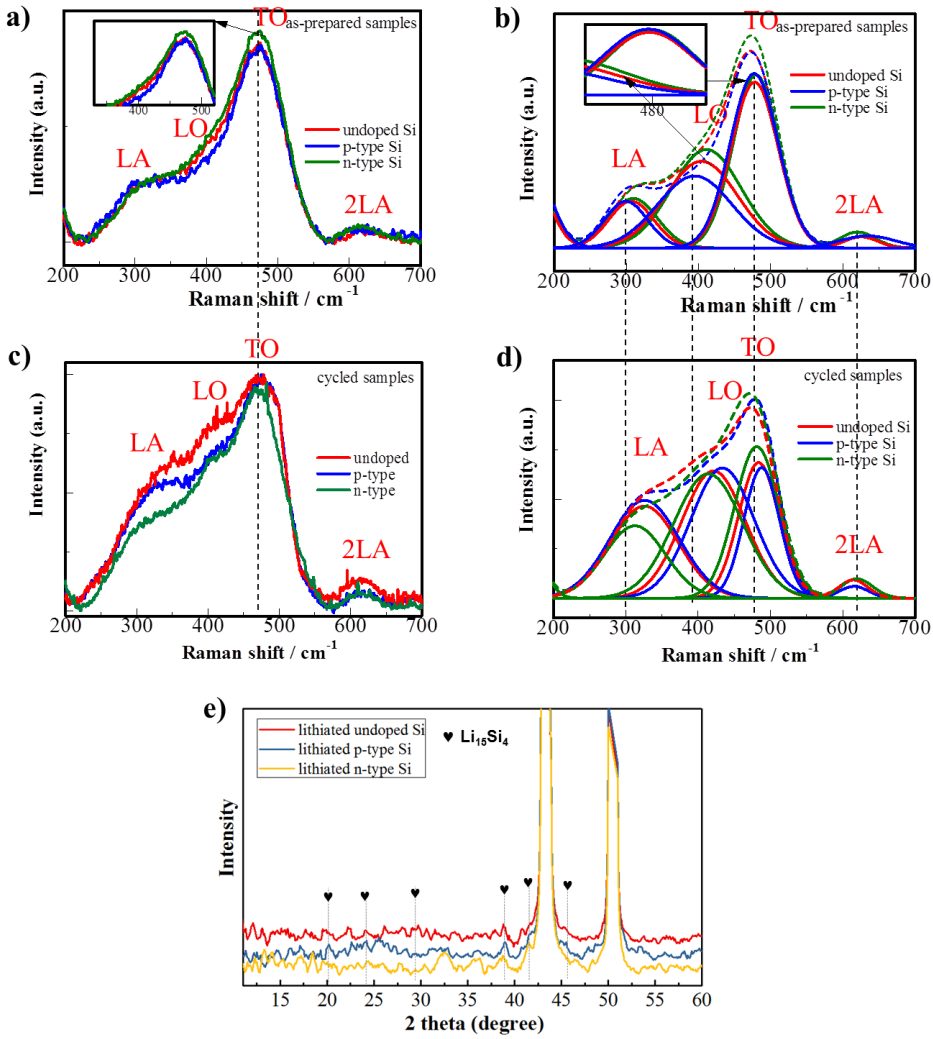

Fig. 61 Normalized Raman spectra for undoped, *p*-type and *n*-type Si thin films (a) before and (c) after cycling; and the fitting results (b) before and (d) after cycling; (e) XRD pattern of lithiated Si thin film.

Comparing the FWHM for pristine samples, TO and LO scattering peaks have noticeably lower values for the *n*-type doped Si thin film, while the FWHM of LA is

much higher. FWHM of 2LA for *p*-type is significantly wider than that of the two others. The reasons are the same that were explained above for pristine *n*-type and *p*-type doped Si thin films, i.e. the influence of the frequencies of B and P scattering photons which distorts the near-located LA, LO, and 2LA peaks. The general behavior of FWHM value for all bands of each lithiated sample was theirs decrease, except LA and 2LA bands, which FWHM was found to be lower for all type of lithiated samples. This phenomenon opens new questions and requires further deep investigation.

Table 6 – The positions of the peaks on Raman spectra of variously doped pristine and lithiated Si thin film samples.

Peaks\Si type	Undoped		*p*-type		*n*-type doped	
	pristine	lithiated	pristine	lithiated	pristine	lithiated
	peaks positions					
TO	477.8	480.3	477	487.9	479.7	481.2
LO	404	415.9	394.9	433.8	410.9	414.1
LA	306.8	332.3	299.4	325.6	309.8	312.5
2LA	625.2	618.7	634	615.7	620	619.6
	full width at half maximum (FWHM)					
FWHM(TO)	76.7	66.6	78	57.9	74.5	72.8
FWHM(LO)	117	76.2	121	103.2	113	112.3
FWHM(LA)	73.2	111.7	70	113.1	77.7	99.6
FWHM(2LA)	54.3	54	89	46	58.4	51.6

In order to observe the behavior of the *n*-type Si electrode in the cell *in situ* Raman studies were performed. Fig. 62a shows the Raman spectra of the cell components – Si, Cu, electrolyte (LPF_6 in EC:DEC:EMC) and Si with the electrolyte to see the original signs. The main Si peak is visible at around 480 cm^{-1}; the scattering from the electrolyte is presented by several peaks at around 741 cm^{-1} for $LiPF_4$, 940–980 cm^{-1} for EC and DEC additives [215], 1110 cm^{-1} for Li_2CO_3[216] and peak originated at ~570 cm^{-1} which is more probably related to the Li_2O [217].

Cu substrate did not have any significant peaks that could be noticed in the final spectrum of Si thin film anode at its cycling. Thus, the abovementioned peaks were observed in the spectra in Fig. 62b,c. Due to the several components were contributed to the spectra, the structural modification of Si could be hardly seen; however, the general behavior of Si-electrolyte system can be retrieved. From Fig. 62b and c, according to the trend of the Si peak at 480 cm^{-1} during lithiation/delithiation, there is an obvious decrease in the intensity after the beginning of the lithiation. This can be explained by the beginning of the alloying reaction and/or other irreversible reactions taking place in the first cycle.

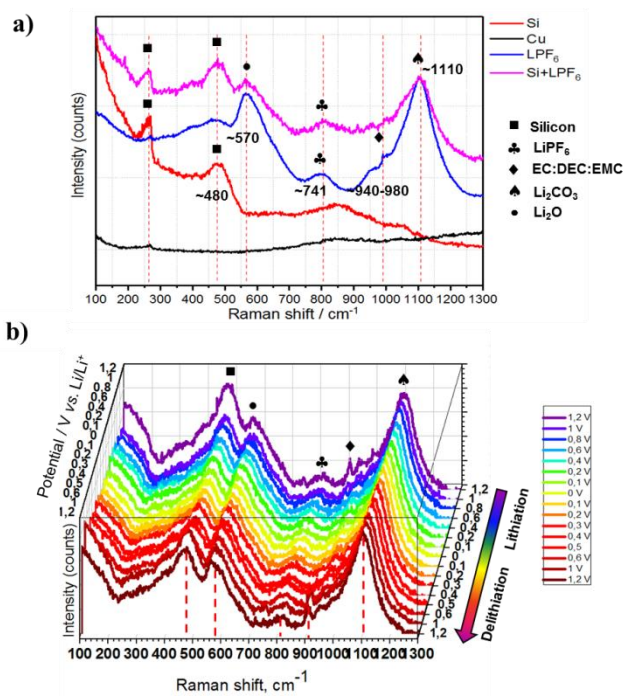

Fig. 62 (a) The separate spectra of cell components, (b) *in situ* Raman spectra of Si thin film anode during first cycle (CV at 0.3 mV s^{-1} in a potential range 0.01 – 1.2 V).

When the lithiation process is in progress, the peak of Si becomes equal in height with the unchanged near-located peak at ~580 cm^{-1}. During the delithiation, especially considering the last several spectra at 0.6 – 1.2 V, it can be noticed that the intensity of Si peak is increasing again. Another interesting fact discovered in this study is the behavior of EC and DEC electrolyte additives components via the shift

of around 980 cm^{-1}, which can be noticed in the early stage of lithiation (0.6 – 1.2 V) and the same potential only at the end of the delithiation process. We suppose that this can indicate on the reversibility of EC and DEC participation at the ongoing electrochemical processes, in particular, in the SEI layer formation.

As it was shown above, among three types of samples – undoped, *p*-type and *n*-type Si thin films, the latter one demonstrated the longest cycle life and CE stability. Initially, we believed that the enhanced electronic conductivity can result in the improvement of *p*- and *n*-type doped anodes. It was suggested that the possible reason is due to the fact that the electron mobility occurs in *n*-type (P) Si via movement of free electrons as happens in metals, while in *p*-type (B) Si, it goes via mobility of the positive holes which can be limited by the neighboring Si/dopant species making the electronic conductivity inferior. However, the measurements of the electronic properties obtained for these samples revealed the absolutely opposite results than the expected ones.

In order to clarify the results and to estimate the charge/discharge characteristics of doped Si negative electrodes, the electronic energy band diagram of the anode-electrolyte interface was considered (region between conduction (E_{CB}) and (E_{VB}) valence bands). At the first immersion of semiconductor into the electrolyte, the potential (Fermi level) is not equal between two different phases. In order to equilibrate this interface, the charge from one phase moves to the other causing the "band bending" in the semiconductor phase [218]. Fig. 63 represents the energy levels at a semiconductor-electrolyte interface before and after contact for *n*-type and *p*-type doped semiconductors, respectively. After contact, the net result of equilibration is that Fermi level (E_F) in semiconductor becomes equal to that of electrolyte ($E_{F,redox}$) and a ''built-in'' voltage, V_{SC}, forms in Si.

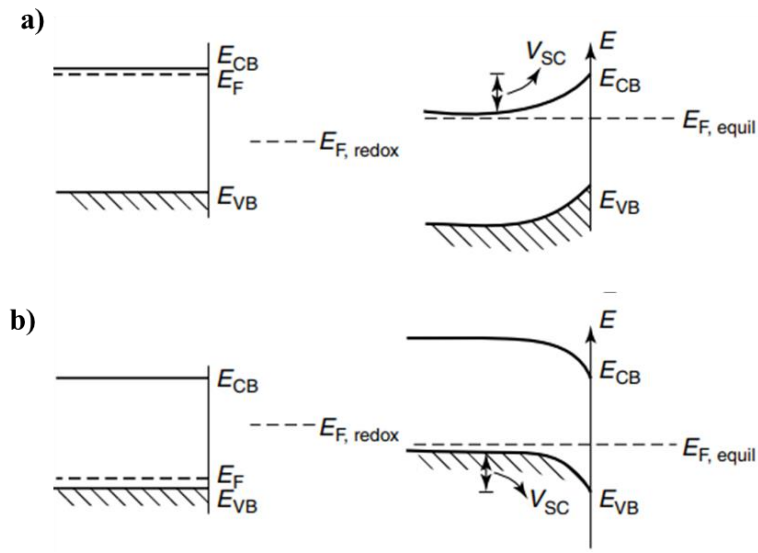

Fig. 63 The Si-electrolyte interface before and after equilibration (a) for *n*-type semiconductor and (b) for *p*-type semiconductor. [218]

For the *n*-type Si (Fig. 63a), the electronic charge consumed for Fermi level equilibration in the semiconductor comes from the donor impurities. The Si's Fermi level in the *n*-type Si decreases up to the same level as in electrolyte, while for the *p*-type Si, the Fermi level has to increase (Fig. 63b).

During the Li^+ insertion, an electron has to move to an unoccupied state in the host band structure. In the *n*-type Si, the electron has to occupy a conduction band, whereas, for *p*-type Si, low energy valence band with is available [219]. This, in turn, can cause a delay of the charge flow in the *n*-type Si due to the higher potential barrier [220]. From the other hand, it was reported that the incorporation of B and P dopants may reduce the lattice spacing of crystalline Si that resulted in the rise of the Li^+ ions insertion [219,221]. Taking into account the above considerations, Li^+ ions insertion into the *n*-type doped Si is energetically less preferably comparing with the *p*-type and undoped Si.

In our research, the Si thin films of the amorphous phase were prepared. Due to the high concentration of inactive impurities, the incorporation of dopants led to the decrease in conductivity and mobility of the *p*- and *n*-type Si. As a subsequence, it

was complicated to detect by structural investigation the decrease of Si-Si interatomic distances as the result of by the incorporation of the dopants. However, considering the results of Raman spectroscopy of the variously doped lithiated Si, it was observed that *n*-type Si experienced less shift comparing to undoped and *p*-type Si. In fact, such suppression of the structural degradation can partially confirm the theoretic discussion that explains the better electrochemical characteristics of the *n*-type Si by the low energy increase of Li^+ ions insertion.

Thus, the delivered capacity increased up to around 1500 mAh g^{-1} by extending the lower cut-off voltage from 0.1 V to 0.01V. The improved performance of *n*-type Si was explained by the existing energy barriers for the lithiation insertion. In addition, *ex situ* and *in situ* Raman spectroscopy was applied in order to detect the structural changes in the Si with the various dopants and the general modification trend of the Si and electrolyte peaks.

6.3.3 Effect of the electrolyte additive on the cycling performance of Si anode

The content of electrolyte can influence the electrochemical properties of the cell. In the Literature review (Chapter 2, §2.5.2), certain additives were presented to improve the cycle life of Si-based anode. Unsaturated compounds are usually used as additives in nonaqueous electrolytes because they have unsaturated functional groups (double or triple bonds) which can easily run polymerization at the conditions of the electrochemical loads (reduction/oxidation). VC is one of the main promising representatives of unsaturated additives [222] and can be polymerized into poly(vinyl carbonate) (PVCA) on the electrode surface during charge/discharge process, which strengthens the SEI layer and finally improves the cycling performance of the batteries. In this work, 5% VC was added into the standard LPF_6 in EC:DMC:EMC (1:1:1, vol.) via 3 h stirring the solution in Ar-filled glovebox.

The results of the electrochemical cycling of the Si thin film anode cycled in the abovementioned electrolyte at the current density around 15 μA cm^{-2} with the addition of 5% VC are shown below. Fig. 64a illustrates the potential profile of

assembled cells with Si anode. All plateaus correspond to the typical Si potential curves explained in earlier sections; and the dQ/dV plot in Fig. 64b also shows the same behavior of the lithiation/delithiation process as for *n*-type Si film anode cycled without VC. However, one can see the differential capacity value of Si thin film in the 250th cycle which almost does not differ from that in the 100th cycle. For the period 100–250 cycles, no noticeable polarization can be observed. Fig. 64c shows the cycling of the cells with *n*-type Si thin film with VC (red) and without it (green). One can see that the cycling performance of the former cell is much better in spite of small gradual capacity decay can be observed there. Fig. 64d demonstrates the CE plot for the same cell, comparing which it can be noticed that CE for VC-containing cell is 99.3% in the first 100 cycles following by increasing up to 99.7% in the rest of cycles.

The rate capability graph is shown in Fig. 64e. The first four cycles related to the same current density that was used in above described electrochemical results (15 μA cm^{-2}). From the 5th cycle, the current density was decreased up to 7 μA cm^{-2} that led to the increase of capacity by 300 μAh g^{-1}. However, when the elevated current densities were applied, the performance of Si anode deteriorated. The current densities of 60 μA cm^{-2} and 120 μA cm^{-2} resulted in the capacity retention of 700 μAh g^{-1} and 200 μAh g^{-1}, respectively. After return to the first current density of 15 μA cm^{-2}, the Si anode showed the initial performance without significant capacity fade.

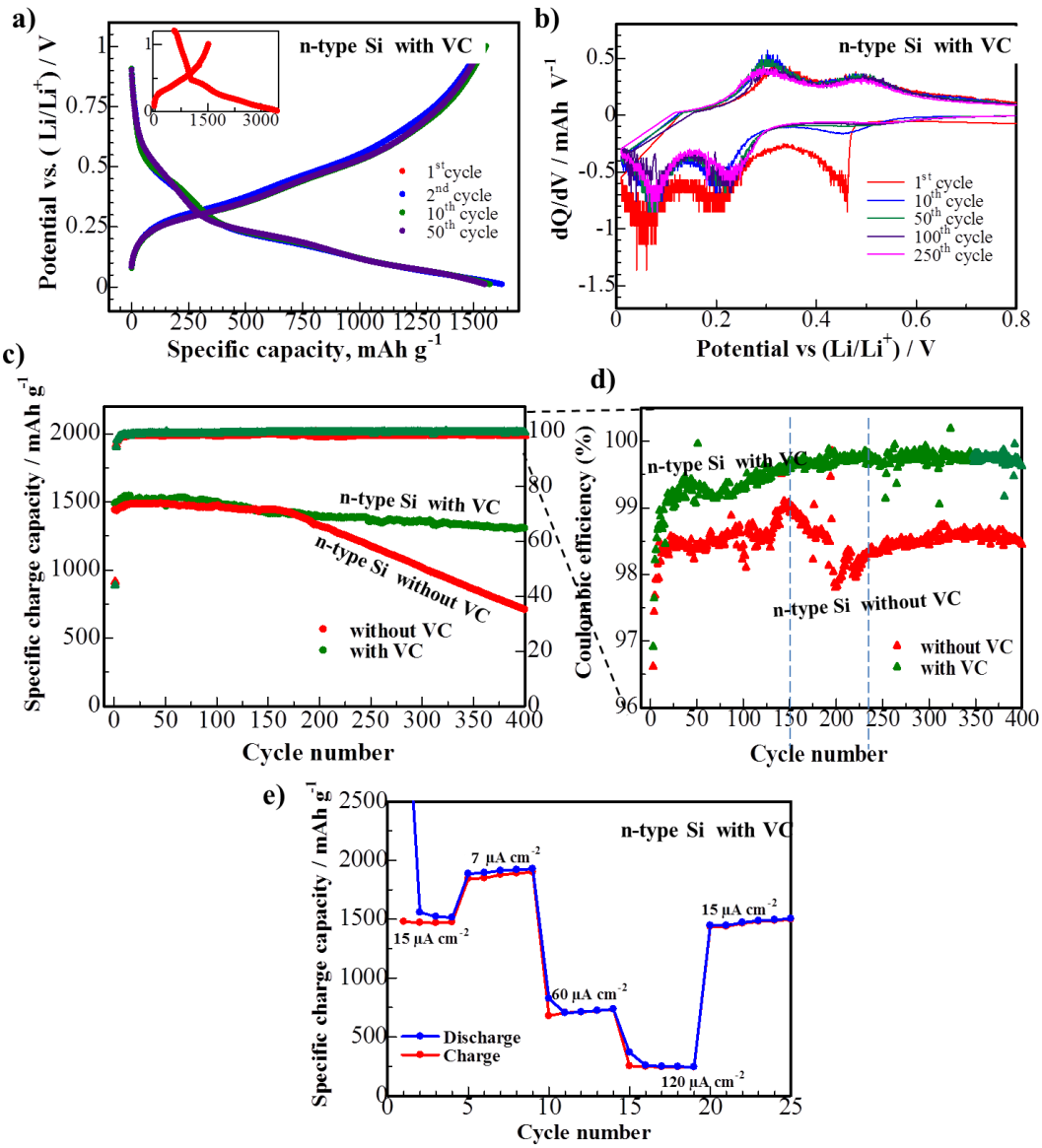

Fig. 64 Electrochemical test results for of Si thin film anode in the presence of VC additive (a) potential profiles, (b) differential capacity plots, (c) cycling performance, (d) CE plot, and (e) rate capability.

The EIS graphs for the cells assembled with commercial electrolyte and the same electrolyte with VC are demonstrated in Fig. 65a and b, respectively. The EIS spectra for both types of samples showed the same behavior. The semicircle in the high-frequency region relates to resistance for Li^+ ions diffusion through the SEI

layer; the medium-frequency region corresponds to charge transfer resistance between the SEI and Si interface; and the low-frequency region is assigned to Warburg impedance diffusion of Li^+ ions in the Si and insertion capacitance accumulation of Li^+ ions in its bulk [136]. For both cells, EIS was the equivalent after the first cycle then decreased after 10 cycles and again increased after the 50th cycle. However, for the samples cycled with VC, the values of impedance in all cycles were slightly higher, which can be resulted from the modified properties of SEI layer, in particular plasticity or density. We did not register the stability of EIS in the presence of VC-containing electrolyte as it was reported in work [136]. Besides, our EIS observations for 3% VC-containing electrolyte can be compared with another study where the authors recorded the impedance decrease with cycling [223].

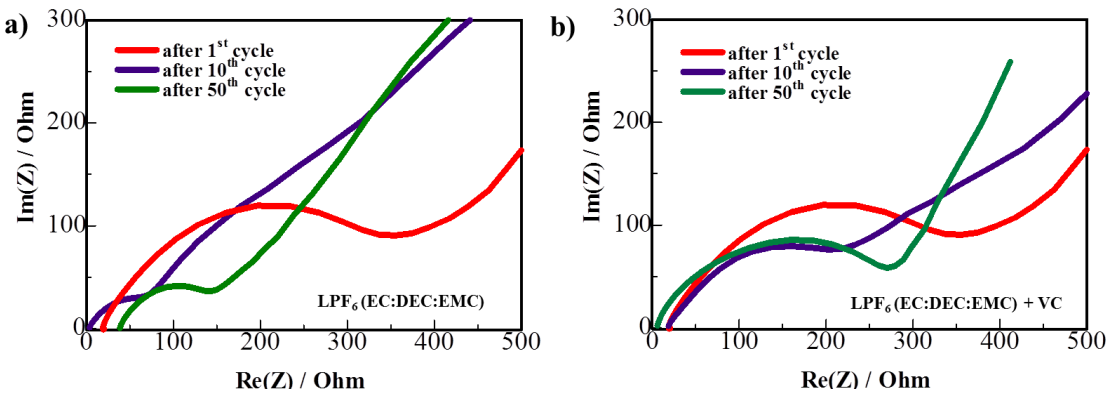

Fig. 65 Electrochemical impedance spectroscopy for the half-cells (a) without VC and (b) with VC.

Fig. 66 shows the post-mortem SEI layer investigation of the surface of Si thin film anodes which were cycled for 1(Fig. 66a,b), 10 (Fig. 66c,d), 50 (Fig. 66e,f) cycles in the absence and presence of VC electrolyte additive. Comparing SEM images of Si surface after 1st cycle for both types of samples, it could be noticed from Fig. 66a that the cracks already presented in the formed SEI in the absence of VC. After 10 cycles, the number of the cracks was higher for Si surface, cycled with VC-free electrolyte, while in VC-containing electrolyte it was no obvious cracks at all. The obvious benefit of the VC additive could be observed even after 50 cycles of

cycling (see Fig. 66e,f). The SEI layer formed at the decomposition of VC-containing electrolyte looks more steady and ductile than that of VC-free electrolyte. More likely, this could originate from the fact that VC additive pushes the polymeric species generation at the electrolyte decomposition instead of $(CH_2OCO_2Li)_2$, which is the major component in the conventional SEI species formed at the decomposition of electrolyte [224]. Interestingly, it was found that SEI layer, formed in the presence of VC, had the small nanoscale pores of around 500 nm and 10-50 nm in a diameter as can be seen from the SEM image insets for the samples cycled for 50 cycles. The smaller pores can be also noticed in Fig. 66d for SEI/Si surface cycled with VC for 10 cycles.

As a possible explanation of appearance of extensive porosity of "VC-containing" SEI layer can be an assumption that the gas could be generated in the process of SEI layer formation or maybe even later in case some reactants are trapped into the dense polymeric SEI matrix, which may slow down the reactions and limit the release of gas. It is known that the main gas products at the decomposition of VC-containing electrolyte are C_2H_4 and CO_2 [225]. The gas can be accumulated inside of SEI and then released breaking the layer. However, it is not excluded that CO, C_2H_6, CH_4, and H_2 could be also produced and impact the pore occurrence [226]. According to the recent studies, one of the main component of SEI layer, solid lithium fluoride (LF), occurs with the release of H_2 gas during the decomposition of HF electrolyte impurity [227]. In spite of it was reported that VC inhibited the production of LiF crystals, the latter anyway formed in the noticeable amounts revealed by XPS measurements [224,225,228]

In fact, the porous SEI layer could affect positively on improving of Si thin film in two aspects. Firstly, the ionic conductivity of the system will be higher due to the presence of the shortest ways for Li^+ ions migration towards to electrode. Secondly, such pores also could accommodate the stress in the SEI layer during the Si expansion and prevent the SEI film cracking.

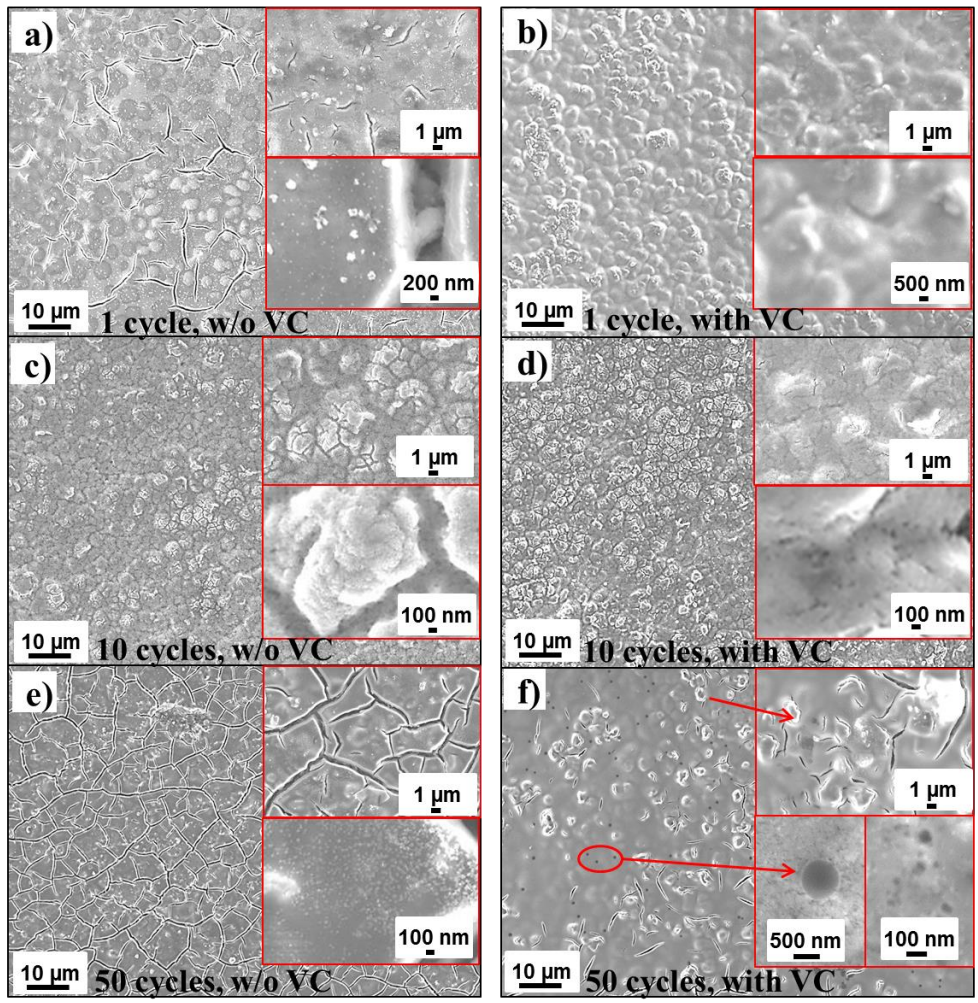

Fig. 66 Post-mortem SEM analysis of SEI on Si thin film cycled in the cells without (left column) and with VC (right column).

Fig. 67 demonstrates the FIB/SEM images of the same Si samples. For the samples cycled only once (Fig. 67a,b), the difference in the formed SEI could be easily observed; no cracks were noticed in the "VC-containing" SEI layer. However, if we compare the magnified cross-sectional views of Si films (Fig. 67c,d), the interesting discrepancy could be noticed. Si thin film cycled in the VC-free electrolyte (Fig. 67c) has the diverse morphology than that of another sample (Fig. 67d); the upper part of film expanded much more than the lower part, besides there are cracks in the lower Si part lying close to the substrate. From the cross-sectional

image of Si film cycled with VC (Fig. 67d), we could see that Si is uniform in thickness, and the SEI layer can be easier distinguished on its surface.

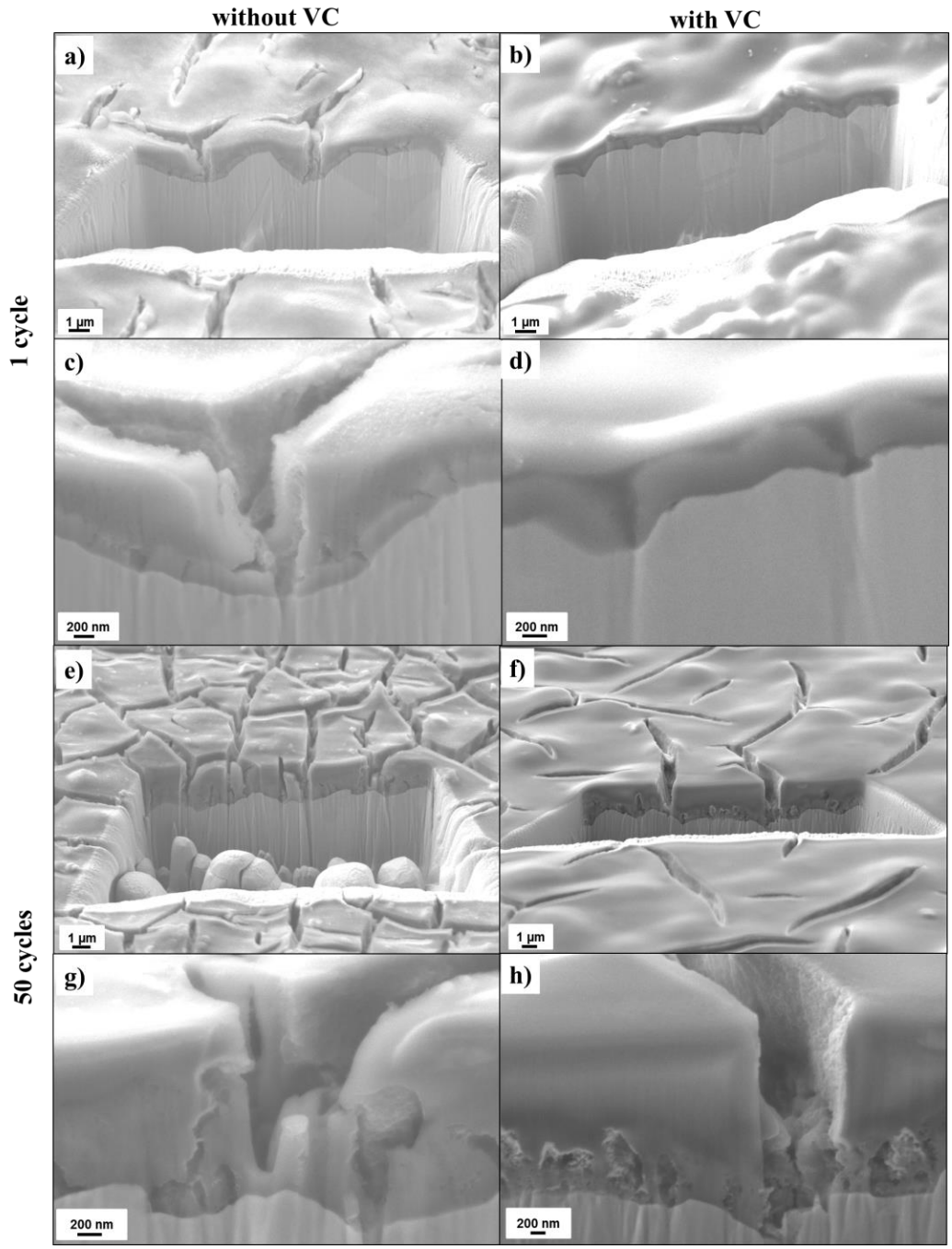

Fig. 67 FIB/SEM images of Si thin film cycled for 1 and 50 cycles in the cells (a,c,e,g) without VC and (b,d,f,h) with VC.

Considering the images of both types of films after 50 cycles (Fig. 67e,f), one can see that there are fewer cracks in the SEI layer on Si film cycled in VC-containing electrolyte. From Fig. 67g and h, the cross-sectional morphology of Si films could not be observed clearly because of SEI layer melted under focused ion beam, besides for VC-free SEI layer the FIB cutting occurred much easier. At the comparison of the Si-substrate interface region, it was not noticed the deterioration of the adhesion of the Si thin film in both VC-free and VC-containing cells.

In order to investigate the topology of the SEI layer formed in both types of the cells, AFM studies of the samples were performed. The topology of the SEI layer formed at the decomposition of Si in the VC-free electrolyte (Fig. 68a-c) looked like as rough after the first cycle, and it became smoother with time. The roughness, in the beginning, could be originated from the formation of the LF crystallites that are usually observed as the separate particles in the SEI layer grow up with time [136,229]. After 50 cycles, the particles disappeared that can be explained by continuous growing SEI layer which covered those particles. The small prolonged cracks can be noticed on the region of 10×10 μm. For the "VC-containing" SEI layer (Fig. 68d-f), the opposite behavior of the topology was revealed. The mapped square surface region with dimensions 10×10 μm did not contain the cracks which more rarely occurred due to the above-discussed properties of SEI containing the products of VC decomposition. The SEI layer, being well formed and very smooth in the beginning, acquired greater roughness with each subsequent cycle. More likely, that such different behavior can indicate the difference of the SEI formation mechanisms of both types of the SEI. It was reported earlier [224] that VC exhibited a reductive current at 1.5 V vs. Li/Li^+, which is higher potential than that without VC indicating that VC will react first to form the SEI layer, therefore poly(VC) species dominate in the SEI content as it has been reveled in other work [230]. Considering SEM image in Fig. 66f and AFM topology of VC-containing SEI, it looks like some particles are lying on the surface of SEI. The similar observations were reported before for VC-containing electrolyte, where such particles were referred to LF crystallites and/or

oxides [231]. It can be supposed, taking into account that VC-based SEI layer has already formed and did not exhibit the signs of significant continuous growth; such crystallites can form at lower potentials on its surface increasing surface roughness. However, from the closer view in Fig. 69, one can notice that the particles do not just lie on the surface of the SEI, they are inside or under its surface.

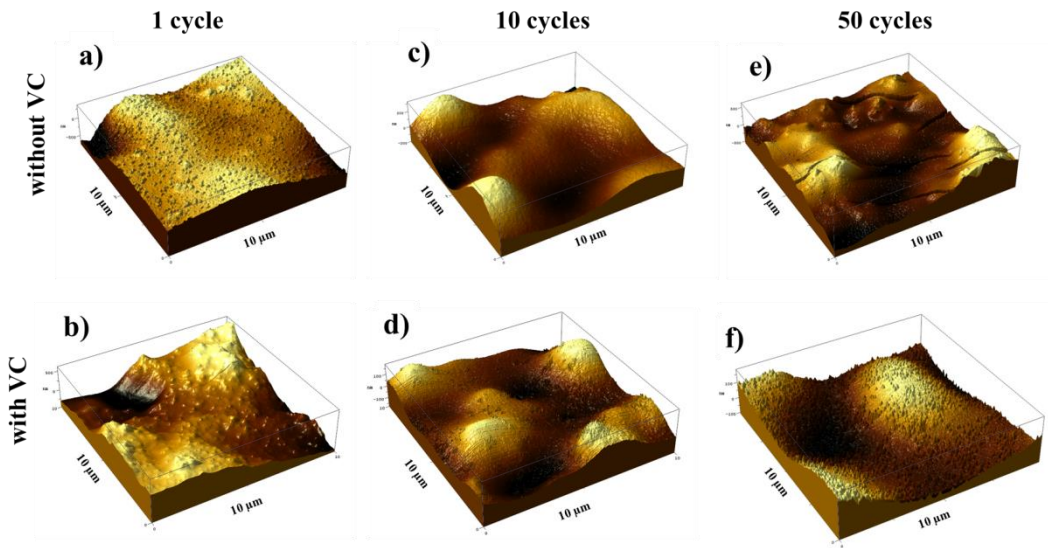

Fig. 68 AFM analysis of the surface of the Si thin film anodes cycled for 1, 10, 50 cycles without VC for (a,c,e) and with VC (b,d,f), respectively.

Fig. 70 illustrates the topology and morphology of the a-Si samples after 400 cycles. In these images, it could be seen that the surface of the sample became very rough with time. Comparing to the post-mortem images of samples for Si cycled in a conventional electrolyte (Fig. 59), one can notice the significant reduction of the material degradation. Fig. 70a,b shows the Si thin film covered by SEI, which is still in good condition with few cracks. After removing SEI, from Fig. 70c,d, the Si surface demonstrates the cracking, however the distance between the cracks is not wide. This is due to the fact that VC-containing SEI restrained the material during expansion and mitigated the pulverization during lithium extraction. Fig. 70e shows the cross section of the Si thin film which noticeable expanded but its delamination from the substrate was not seen. Thus, VC additive has improved not only SEI layer

but also prevented loss of Si active material which could able to rearrange its morphology under SEI film. Besides, the roughness of the anode surface noticed in Fig. 66, Fig. 68, Fig. 69 could be originated simply from the restructuration of Si material.

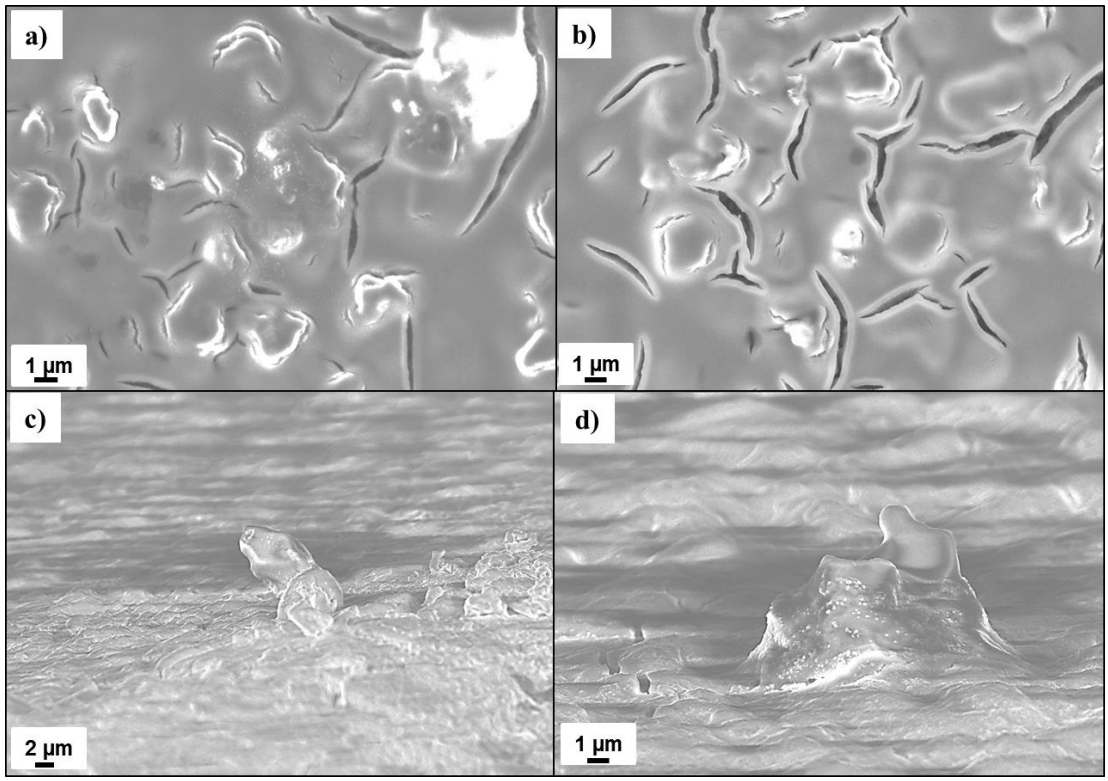

Fig. 69 (a-d) SEM of Si thin film cycled in VC containing electrolyte after 50 cycles.

In general, the presented electrochemical test graphs obviously evidenced the positive and significant effect of VC electrolyte additive on the improvement of the Si thin film based anode. The SEI layer containing polymeric species helped to protect Si thin film from its mechanical degradation.

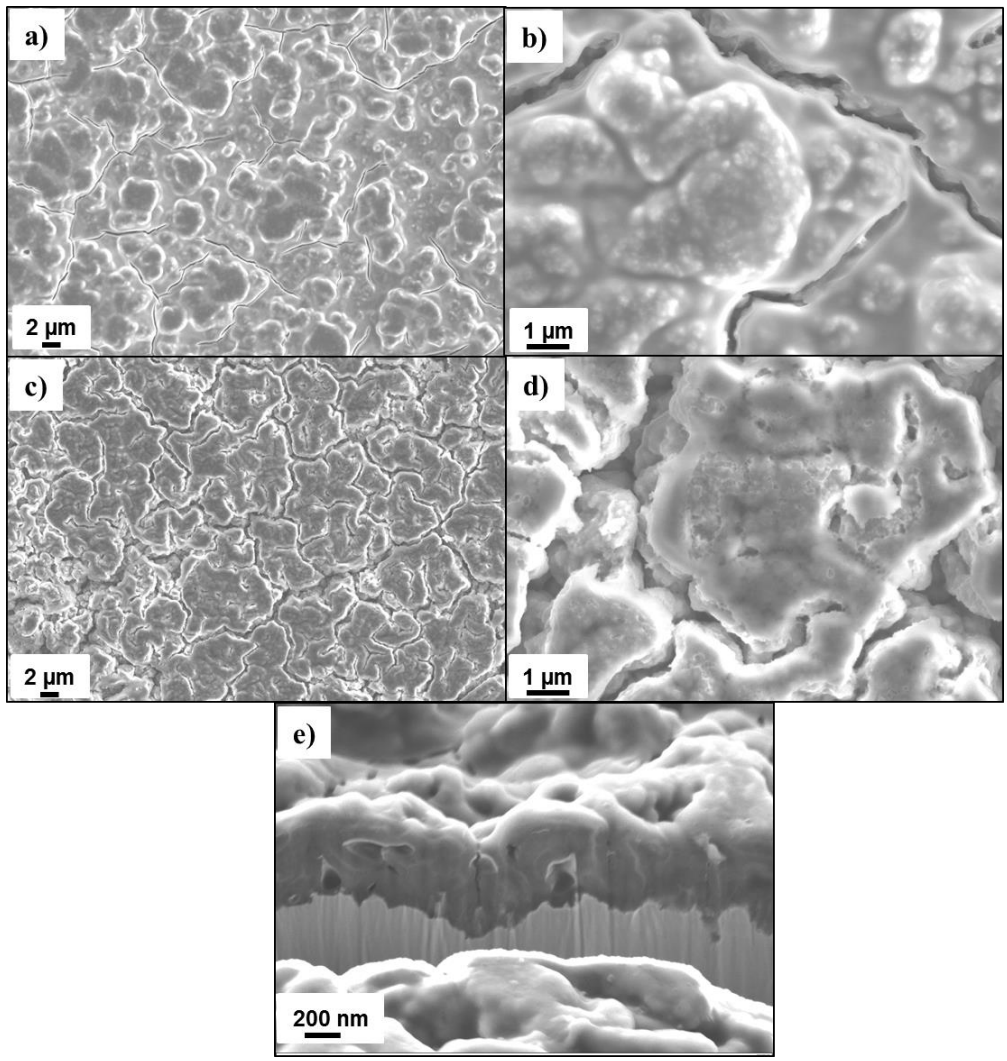

Fig. 70 Post-mortem SEM of Si thin film cycled in VC containing electrolyte for 400 cycles: (a-b) with and (c,d) without SEI layer and (e) FIB/SEM image of Si film cross-section.

6.4 Design and study of composite Si-GF-Ni anode

The alternative successful way for an improvement of the Si thin film is a combination of various anode materials using the benefits. In this section, the design of a novel layered composite anode, the *n*-type doped a-Si thin film on GF coated nickel (Ni) foam for LIBs is presented. GF provide highly conductive stable sublayer for Si thin film. The preparation and basic characterization of GF were presented in

Chapter 5 (§5.4). The technical conditions for Si thin film deposition remained the same (Chapter 6, §6.2).

In order to further study the beneficial effects of prepared materials as anodes for LIBs, their electrochemical performance was examined in Li half-cells. Fig. 71 shows CVs of the samples measured at a scan rate of 0.1 mV s^{-1} within a potential range 0 – 3 V. In order to distinguish the peaks coming from the current collector itself, CV curves of Ni foam were illustrated as well. In Fig. 71a, the peaks appeared at around 1.37 V and 1.23 V related to an initial insertion of Li^+ ions into NiO native layer of Ni foam followed by a displacement process with the formation of Li_2O and reduction of NiO to Ni [232,233]. This process is partially reversible experiencing a decomposition at oxidation of Li_2O and converts back to NiO and Li^+ ion at 1.3 V and 2.5 V[234]. Fig. 71b demonstrates the peaks of GF lithiation/delithiation: an initial SEI layer formation at 0.7 V, disappearing in consequent cycles, the main reduction peaks at around 0.1 V and 0.01 V, and for the oxidation at around 0.25 V [235,236]. So, in the prepared anode system, two materials – GF and NiO were recorded to have the electrochemical activity. However, comparing both CV graphs, recorded under the same conditions for the initial two cycles, we see that intensities of NiO lithiation/delithiation peaks are much lower than those for GF.

The CV plots of 3D Si-Ni anode are illustrated in Fig. 71c. Distinguishable cathodic peaks observed at around 1.37 V and 0.4 V during the initial discharge process can be ascribed to the first occurred reactions between Li^+ ions and electrolyte on a NiO native layer and on the surface of Si [202], respectively, with the formation of solid electrolyte interphase (SEI) on the electrode surface. Another cathodic peak at around 0.84 V is related to the reaction between Li^+ ions and NiO native layer of Ni foam where NiO reduces to Ni and Li_2O forms [232,233]. The next process is alloying of Li^+ ions into Si thin film (Li_xSi_y) at the potentials of 0.012 V and 0.001 V with the posterior dealloying at 0.33 V and 0.53 V, which corresponds to a release of Li^+ ions from Li_xSi_y alloy during the discharge stage. The anodic peak of around 1.3 V can be ascribed to a reversible reaction between Ni and Li_2O

[232,233]. Fig. 71d shows the CV curves of Si-GF-Ni anode. An initial SEI layer formation on GF surface can be indicated by a small peak at around 0.7 V, disappearing in the following cycles. The lithiation reaction of GF extends the peak intensity at around 0.01 V as well as that of its corresponding delithiation peak at around 0.3 V. The reaction governing the first delithiation peak of Si usually occurs at the same potential [235,236]. Besides, the second Si delithiation peak at 0.49 V is observed on the anodic scans, indicating the participation of Si in the overall electrochemical reaction. It is noticeable in the magnified graph in Fig. 71d that the NiO lithiation/delithiation peaks are still present in Si-GF-Ni electrode indicating that the native oxide layer was not completely removed from the Ni foam surface.

Fig. 72 shows the electrochemical results of galvanostatic charge/discharge cycling of the GF-Ni, Si-Ni and Si-GF-Ni anodes performed at a current density of 30 μA cm^{-2} within a potential window of 0.1 – 1.5 V. All plateaus on charge/discharge curves correspond to the lithiation/delithiation potentials observed in the CV plots above. Fig. 72a demonstrates the voltage profiles for GF-Ni anode with the magnified inset of the potential curves for the 1st cycle. In general, Li^+ ions have the insertion reactions with NiO at the potentials of around 1.23 V and with GF at the potential onset of around 0.2 V. The delithiation from GF can be observed to start at around 0.2 V and from NiO occurs at the potentials of 1.3 V and 2.5 V. From voltage profile, we see that lithiation and delithiation peaks of NiO can be observed in all cycles. Moreover, if we compare the 100th and 250th charge curves, it can be clearly seen that the duration of NiO-Li reaction increases significantly. At the same time, GF film has a higher contribution to the capacity than NiO. Besides, the GF intercalation ability increased upon cycling as well that can be evidenced by an extensional plateau of the GF delithiation. In the initial cycles, the reversible capacity from GF is around 50 μAh (155 mAh g^{-1}) corresponds to that of graphite and increases up to 125 μAh (195 mAh g^{-1}) in the 100th cycle, where the duration of the delithiation reactions beyond the GF delithiation reaction range is significantly longer. Fig. 72b shows the differential plots for GF-Ni anode. One can notice the

formation of new phases at 0.04 V, 0.1 V, 0.2 V and wide peak close to 1 V related to some reaction between Li and NiO. Besides, the amount of electrons and therefore capacity obtained from all these reversible reactions increases with time.

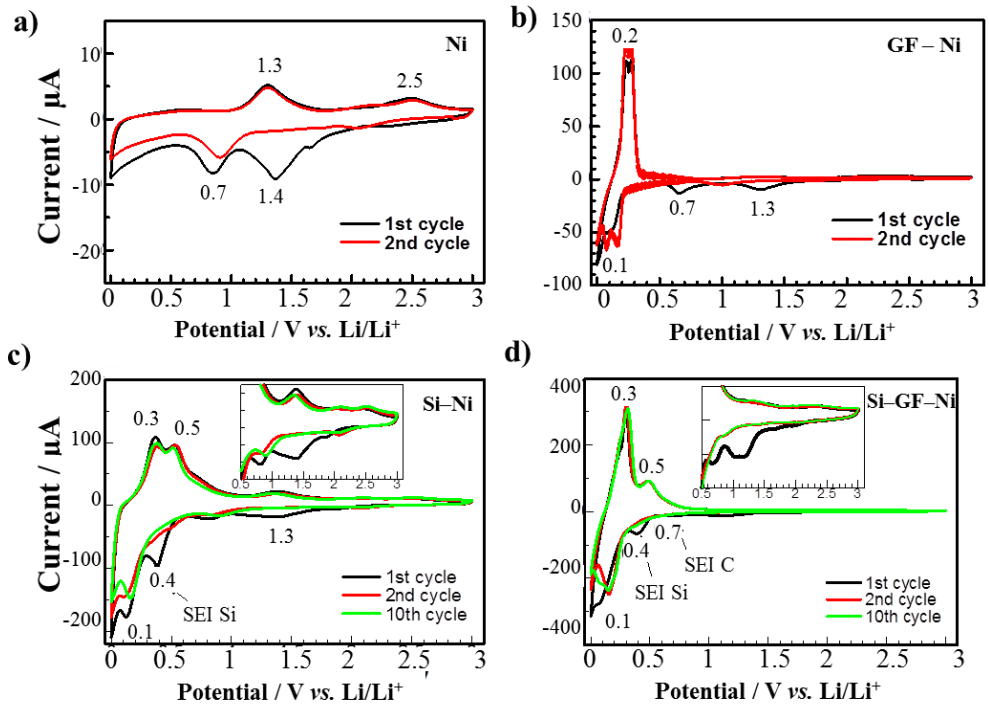

Fig. 71 CV plots of (a) Ni, (b) GF-Ni, (C) Si-Ni, and (d) Si-GF-Ni.

From Fig. 72c, Si thin film on pure Ni loses the most of its initial reversible charge capacity (90 µAh or 2318 mAh g^{-1}) in the 1st cycle and then experiences a gradual capacity fading. The differential capacity plots for Si-Ni anode shown in Fig. 72d illustrates the SEI layer formation on Si at around 0.45 V and Li silicates formation as was explained in the previous paragraphs. The Si-GF-Ni (Fig. 72e) anode exhibits the high initial charge capacity of around 167 µAh, which stabilizes within further several cycles. The differential capacity plots for Si-GF-Ni anode shown in Fig. 72f demonstrates the formation of the same phases which were observed separately in case of GF and Si.

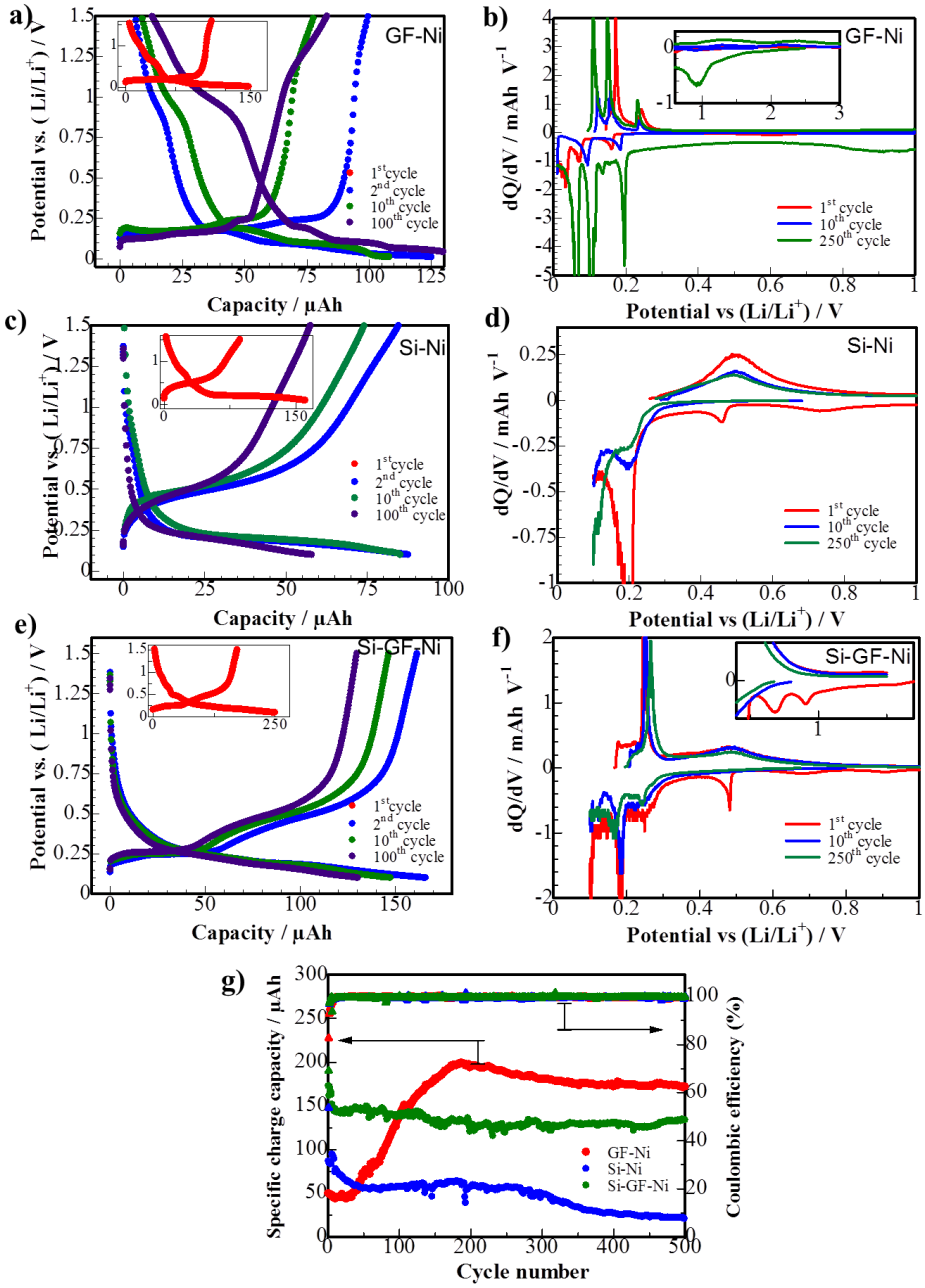

Fig. 72 Potential profiles of (a) GF-Ni, (c) Si-Ni, (e) Si-GF-Ni; differential plots o f (b) GF-Ni, (d) Si-Ni, (f) Si-GF-Ni; (g) cycling performance and CE.

Fig. 72g shows the results for the cycling performances of three anodes, we could see that the lithium cell with Si-GF-Ni has the overall reversible capacity (2nd cycle) two times higher than two other anodes. Taking into account that, the cycling

performance of the GF coated Ni foam anode system experiences the increase of the capacity with a sharp climb after 75th cycle and Si-Ni anode has the capacity fading, the stability of Si-GF-Ni can be achieved by this compensation of two materials integrated into one compositional layered anode.

If the retained capacities of the anodes are presented in the specific gravimetrical units, Si-GF-Ni delivers a capacity of only 326/225 mAh g^{-1} and 175/175 mAh g^{-1} in the first and last discharge/charge, respectively, which is due to a low content of Si (about 9 %). However, from the cycling performance, it could be easily observed that half of this capacity is delivered by Si film.

Fig. 73a,b shows the SEM images of materials used for the preparation of the anode. Fig. 73c and d depict images of pristine a-Si thin film with an inset image of higher magnification. The morphology of Si film for both cases, Si-Ni and Si-G-Ni, was absolutely the same as for the film discussed earlier (Chapter 6, §6.3.1). Due to the complicated structure of substrate and deposition technique, it is hard to provide the mean value of Si thin film thickness; however the observed range of thicknesses was between 50 – 150 nm.

Fig. 73e,f illustrates SEM images of the samples retracted from the cells cycled 500 times. The post-cycling investigations of Si-Ni anode (Fig. 73e) revealed the presence of cracks and partial delamination of Si thin film from Ni foam. Besides, this detachment was not so wide as for flat monolithic Si thin films reported earlier [9]. From SEM images of Si-GF-Ni shown in Fig. 73f, we detected extensive delamination of GF sheets together with the sputtered Si thin film. In spite of this, the designed anode system did not have any failure in maintaining its capacity. We suppose, that this can be explained by the fact that there was a strong adhesion at the GF-Si interface region. More likely, that even at the partial material delamination from foam, GF still had the contact with current CC, which provided the paths for electron mobility.

Thus, Si-GF-Ni anode maintains the overall capacity within a range of 130 – 150 μAh upon all 500 cycles performed. The designed 3D compositional Si-GF-Ni

electrode showed promising potential for use in LIBs owing to a combination of two active materials in one system.

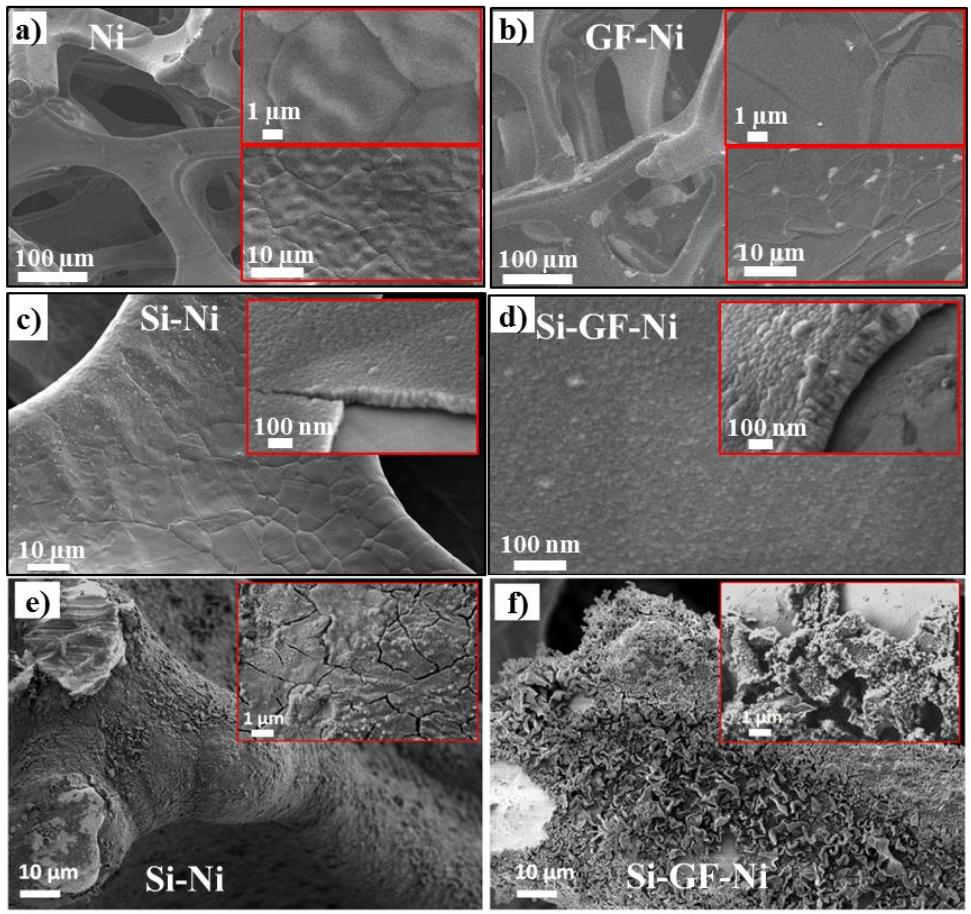

Fig. 73 SEM images of pristine samples (a) Ni foam, (b) GF-Ni, (c) Si-Ni, (d) Si-GF-Ni anodes; and the samples after 500 cycles (e) Si-Ni, (f) Si-GF-Ni.

6.5 Summary

The presented results provide the information on the preparation and optimization of amorphous Si thin film anode on the porous substrate as well as compositional Si-GF anode on the 3D shaped substrate. The study on the effect of the surface condition evidenced that porous-like Cu foil with high surface significantly improved the cycling stability up to 110 cycles and, according to SEM images, decreased the degradation rate of Si thin film. During the study of the doping

effect, it was clearly showed that the incorporation of *n*-type dopant prolonged the cycle life of the Si thin film anode (up to 175 cycles). The addition of VC electrolyte additive provided the strong SEI layer and helped to extend delivering of stable capacity up to 400 cycles. The promising features of electrochemical results of GF grown on Ni foam were observed. The intensifying capacity of GF helped to compensate for the fade of Si capacity. The designed anode could able to retain the stable capacity up to 500 cycles even without VC additive. The investigations were accompanied by Raman spectroscopic studies, AFM topological mapping and SEM imaging before cycling, as well as applying *ex situ* and *in situ* approaches.

7 FINAL CONCLUSIONS AND FUTURE WORKS

In this doctoral dissertation, the main focus was directed on the design and engineering of advanced Si-based thin film anode materials for LIMBs. Two materials were investigated as the anodes, 3C-SiC and Si. The fabrication of the thin films, the properties of prepared material and the final electrochemical performances were discussed.

7.1 Conclusion and future works for the study of 3C-SiC as an anode for LIMBs

In order to investigate the 3C-SiC electrochemical characteristics, the various engineering approaches were applied. For the first time, the electrochemical study on the ability of monocrystalline SiC with a cubic lattice to react with Li^+ ions was performed. This research was pushed by the desire to find a new material that can be intercalated by Li^+ ions. Taking into account that 3C-SiC is a very strong material, its use can open a new horizon in microbatteries. The challenges in this part of the research were related to the fact, that epitaxial ~350 nm thick 3C-SiC was grown on the 525 μm Si wafer, so it could not be tested in a conventional way with liquid electrolyte because highly active Si clearly dominated in the electrochemical reactions. First of all, the alloying of 3C-SiC and Li should be excluded. Thus, the study on the interaction of these materials at the elevated temperatures was performed which revealed that a crystal of 3C-SiC remained almost intact. The advanced SP method showed some signs of the electrochemical activity of 3C-SiC. Several lithiation and delithiation peaks were observed in CV plots. Finally, 3C-SiC thin film separated from Si wafer was electrochemically tested using the liquid electrolyte, and the obtained CV and charge-discharge graphs were similar to those recorded during SP method. The possible charge-discharge capacities were found to be much lower than the expected values. The post-mortem XRD, Raman, SEM, and TEM analysis confirmed a structural and mechanical intactness of the 3C-SiC after electrochemical cycling. XPS of samples after full lithiation showed that Li^+ ions were concentrated on near-surface layers of 3C-SiC. Despite the diameter of Li^+ ions

is less than the lattice parameters of 3C-SiC, they cannot penetrate deeper into its bulk.

Therefore, *the future works for the development of 3C-SiC* anode should be directed on to the understanding of this phenomenon. First of all, the nature of possible reaction, intercalation or capacitance, in 3C-SiC during Li^+ ion insertion should be evidenced. The modeling should be done in order to simulate the reaction at the atomic level (for instance, by VASP program, the Vienna Ab initio simulation package), which can provide the real reasons and possible scenarios how to change materials in order to allow Li^+ ions to go inside of crystal and, maybe even, to initiate their intercalation. Then, the synthesis of 3C-SiC with modified crystal parameters should be done; the material should be characterized and electrochemically assessed until the capacity will be obviously increased.

7.2 Conclusion and future works for the development of amorphous Si-based thin films as an anode for LIMBs

Another part of the research was devoted to the implementation of various engineering strategies such etching, magnetron sputtering, for solving the problems of pure Si thin film anode which are the enormous volume change during lithiation/delithiation, low conductivity and continuous formation of the SEI layer. The *n*-type amorphous Si on the porous substrate and Si on GF coated Ni foam was successfully designed and tested.

The Cu foil was modified by etching and used as a porous substrate. The increase of the surface area as well as the formation of a cave-lake topology significantly decreased the degradation rate of Si and, therefore, improved the cycling performance. The study of the doping effect on the cycling performance clearly revealed that *n*-type Si works better than undoped and *p*-type doped samples. The influence of VC addition into the electrolyte was found to bring an improvement of the Si thin film anode in terms of its better mechanical stability. This is due to the modified composition of the SEI layer that acted as a deterrent coating and helped to

accommodate the expansion of Si thin film from the top as well as preventing its extensive pulverization and delamination. In the case of using Ni foam as the porous substrate for Si film, the increased surface helped to retain 50% of initial reversible capacity after 300 cycles. However, using GF as an additional electrochemically active component and a conductive layer for Si demonstrated even better results in the doubled capacity value and stability which was extended up to 500 cycles. It is worth to underline, the presence of GF demonstrated the alternative way to prolong the battery operation time; even if Si degrades GF can remain to guarantee a backup power upon a long term cycling. It may be a noteworthy solution for special cases such as medical and some other electronic devices, where there are risks of stopping vital processes because of unexpected battery failure.

The comparison of the results obtained from Si-based anodes designed in this thesis with those already published by other authors can be found in the Appendix 1, Table A1. There were difficulties with the comparison due to the different representations of the capacity unit such as total (μAh), areal (μAh cm^{-2}), specific (μAh g^{-1}) or volumetric (μAh cm^{-2} μm^{-1}) capacity. However, in general, it could be seen that our Si-based anodes demonstrated one of the top results in terms of cycling performance, capacity and number of stable cycles.

Thus, the planned design and engineering of the Si-based thin film anode materials for LIMBs was successfully realized within this research.

For *the future improvement of amorphous Si-based anodes,* several approaches could be applied. Regarding the *n*-type amorphous *Si anode on the porous substrate*, the improvement can be achieved by studying the etching parameters to additionally increase the substrate roughness. For *Si-GF-Ni foam*, the optimization of designed anode should be directed, first of all, onto achieving better adhesion between grown GF and foam. The logical way is to make a surface treatment of foam's wires in order to apply the effect which was observed for Si on the porous Cu foil. Secondly, another method for the Si deposition on foam should be employed to achieve better uniformity of the film on the foam surface. Besides, the method should provide the

ability to obtain the amorphous phase of Si and easy incorporation of dopants. Thirdly, some additional elements might be incorporated into Si during deposition to passivate the defects usually present in the amorphous Si. The presence of H_2 is not desirable because it can easily leak from material even at room temperature reacting with electrolyte components which in turn results in the additional amount of LiF. The latter is known to increase impedance that will negatively affect the capacity or/and cycling life. The effect of VC additive on the total number of stable cycles of Si-GF-Ni anode should be reported. The final step for both Si on porous Cu and Si-GF-Ni anodes would be to test them with the solid electrolytes, ceramic, polymer or gel-polymer, as well as with cathodes, that will be used in the future research and development of the thin film LIMBs production.

BIBLIOGRAPHY

[1] V. Bormashov, S. Troschiev, A. Volkov, S. Tarelkin, E. Korostylev, A. Golovanov, M. Kuznetsov, D. Teteruk, N. Kornilov, S. Terentiev, S. Buga, V. Blank, Development of nuclear microbattery prototype based on Schottky barrier diamond diodes, Phys. Status Solidi. 2012 (2015) 2539–2547.

[2] S. Ferrari, M. Loveridge, S.D. Beattie, M. Jahn, R.J. Dashwood, R. Bhagat, Latest advances in the manufacturing of 3D rechargeable lithium microbatteries, J. Power Sources. 286 (2015) 25–46.

[3] J.-M. Tarascon, M. Armand, Issues and challenges facing rechargeable lithium batteries, Nature. 414 (2001) 359–367.

[4] M. Armand, J.-M. Tarascon, Building better batteries, Nature. 451 (2008) 652–657.

[5] J. Troiano, How do lithium ion batteries work? A nanotechnology explainer, (2013) URL: http://sustainable-nano.com/2013/10/15/how-do.

[6] X. Zhang, Numerical modeling of energy storage materials, Stanford University, 2017.

[7] D. Deng, Li-ion batteries: Basics, progress, and challenges, Energy Sci. Eng. 3 (2015) 385–418.

[8] S.D. Jones, J.R. Akridge, F.K. Shokoohi, Thin film rechargeable Li batteries, Solid State Ionics. 69 (1994) 357–368.

[9] J.P. Maranchi, A.F. Hepp, P.N. Kumta, High capacity, reversible silicon thin-film anodes for lithium-ion batteries, Electrochem. Solid-State Lett. 6 (2003) A198–A201.

[10] J.F. Ribeiro, R. Sousa, M.F. Silva, L.M. Goncalves, M.M. Silva, J.H. Correia, Thin-film materials for solid-state rechargeable lithium batteries, ECS Trans. 45 (2013) 139–142.

[11] N.J. Dudney, Thin film micro-batteries, Electrochem. Soc. Interface. 17 (2008) 44–48.

[12] N. Nitta, G. Yushin, High-capacity anode materials for lithium-ion batteries: Choice of elements and structures for active particles, Part. Part. Syst. Charact. 31 (2014) 317–336.

[13] U. Kasavajjula, C. Wang, A.J. Appleby, Nano- and bulk-silicon-based insertion anodes for lithium-ion secondary cells, J. Power Sources. 163 (2007) 1003–1039.

[14] A. Mukanova, A. Jetybayeva, S.-T. Myung, S.-S. Kim, Z. Bakenov, A mini-review on the development of Si-based thin film anodes for Li-ion batteries, Mater. Today Energy. 9 (2018) 49–66.

[15] T.S.D. Kumari, D. Jeyakumar, T.P. Kumar, Nano silicon carbide: a new lithium-insertion anode material on the horizon, RSC Adv. 3 (2013) 15028–15034.

[16] H. Zhang, H. Xu, Nanocrystalline silicon carbide thin fi lm electrodes for lithium-ion batteries, Solid State Ionics. 263 (2014) 23–26.

[17] G. Nyström, A. Marais, E. Karabulut, L. Wågberg, Y. Cui, M.M. Hamedi,

Self-assembled three-dimensional and compressible interdigitated thin-film supercapacitors and batteries., Nat. Commun. 6 (2015) 1–8.
[18] J.H. Pikul, H. Gang Zhang, J. Cho, P. V. Braun, W.P. King, High-power lithium ion microbatteries from interdigitated three-dimensional bicontinuous nanoporous electrodes, Nat. Commun. 4 (2013) 1–5.
[19] T. Takamura, S. Ohara, M. Uehara, J. Suzuki, K. Sekine, A vacuum deposited Si film having a Li extraction capacity over 2000 mAh/g with a long cycle life, J. Power Sources. 129 (2004) 96–100.
[20] H.K.E. Latha, A. Udayakumar, V.S. Prasad, Effect of nitrogen doping on the electrical properties of 3C-SiC thin films for high-temperature sensors applications, Acta Met. Sin. (Engl. Lett.). 27 (2014) 168–174.
[21] X. Zuo, J. Zhu, P. Müller-Buschbaum, Y.-J. Cheng, Silicon based lithium-ion battery anodes: A chronicle perspective review, Nano Energy. 31 (2017) 113–143.
[22] W.J. Zhang, A review of the electrochemical performance of alloy anodes for lithium-ion batteries, J. Power Sources. 196 (2011) 13–24.
[23] P. Meister, H. Jia, J. Li, R. Kloepsch, M. Winter, T. Placke, Best practice: performance and cost evaluation of lithium ion battery active materials with special emphasis on energy efficiency, Chem. Mater. 28 (2016) 7203–7217.
[24] M.N. Obrovac, L.J. Krause, Reversible cycling of crystalline silicon powder, J. Electrochem. Soc. 154 (2007) A103–A108.
[25] A. Casimir, H. Zhang, O. Ogoke, J.C. Amine, J. Lu, G. Wu, Silicon-based anodes for lithium-ion batteries: Effectiveness of materials synthesis and electrode preparation, Nano Energy. 27 (2016) 359–376.
[26] M.N. Obrovac, L. Christensen, Structural changes in silicon anodes during lithium insertion/extraction, Electrochem. Solid-State Lett. 7 (2004) A93–A96.
[27] J. Graetz, C.C. Ahn, R. Yazami, B. Fultz, Highly reversible lithium storage in nanostructured silicon, Electrochem. Solid State Lett. 6 (2003) A194–A197.
[28] S. Bourderau, T. Brousse, D.. Schleich, Amorphous silicon as a possible anode material for Li-ion batteries, J. Power Sources. 81–82 (1999) 233–236.
[29] H.-C. Shin, J. a. Corno, J.L. Gole, M. Liu, Porous silicon negative electrodes for rechargeable lithium batteries, J. Power Sources. 139 (2005) 314–320.
[30] X.H. Liu, L. Zhong, S. Huang, S.X. Mao, T. Zhu, J.Y. Huang, Size-dependent fracture of silicon nanoparticles during lithiation, ACS Nano. 6 (2012) 1522–1531.
[31] J. Chen, Recent progress in advanced materials for lithium ion batteries, Materials (Basel). 6 (2013) 156–183.
[32] J.R. Szczech, S. Jin, Nanostructured silicon for high capacity lithium battery anodes, Energy Environ. Sci. 4 (2011) 56–72.
[33] T.D. Hatchard, J.R. Dahn, In situ XRD and electrochemical study of the reaction of lithium with amorphous silicon, J. Electrochem. Soc. 151 (2004) A838–A842.
[34] D. Ma, Z. Cao, A. Hu, Si-based anode materials for li-ion batteries: A mini review, Nano-Micro Lett. 6 (2014) 347–358.

[35] P. Limthongkul, Y. Il Jang, N.J. Dudney, Y.M. Chiang, Electrochemically-driven solid-state amorphization in lithium-metal anodes, J. Power Sources. 119–121 (2003) 604–609.
[36] A. Bordes, E. De Vito, C. Haon, C. Secouard, A. Montani, P. Marcus, Investigation of lithium lnsertion mechanisms of a thin-film Si electrode by coupling time-of-flight secondary-ion mass spectrometry, X-ray Photoelectron Spectroscopy, and Focused-Ion-Beam/SEM, ACS Appl. Mater. Interfaces. 7 (2015) 27853–27862.
[37] H. Guo, H. Zhao, C. Yin, W. Qiu, A nanosized silicon thin film as high capacity anode material for Li-ion rechargeable batteries, Mater. Sci. Eng. B. 131 (2006) 173–176.
[38] L.B. Chen, J.Y. Xie, H.C. Yu, T.H. Wang, An amorphous Si thin film anode with high capacity and long cycling life for lithium ion batteries, J. Appl. Electrochem. 39 (2009) 1157–1162.
[39] K. Yoshimura, J. Suzuki, K. Sekine, T. Takamura, Evaluation of the Li insertion/extraction reaction rate at a vacuum-deposited silicon film anode, J. Power Sources. 146 (2005) 445–447.
[40] T.L. Kulova, Y. V. Pleskov, A.M. Skundin, E.I. Terukov, O.I. Kon'kov, Lithium intercalation into amorphous-silicon thin films: An electrochemical-impedance study, Russ. J. Electrochem. 42 (2006) 708–714.
[41] T.L. Kulova, A.M. Skundin, Y. V Pleskov, O.I. Kon, The Li insertion/extraction characteristics of amorphous silicon thin films, Chem. Biochem. Q. 21 (2007) 83–92.
[42] A. Reyes Jiménez, R. Klöpsch, R. Wagner, U.C. Rodehorst, M. Kolek, R. Nölle, M. Winter, T. Placke, A step toward high-energy silicon-based thin film lithium ion batteries, ACS Nano. 11 (2017) 4731−4744.
[43] F. Strauß, E. Hüger, P. Heitjans, T. Geue, J. Stahn, H. Schmidt, Lithium permeation through thin lithium-silicon films for battery applications investigated by neutron reflectometry, Energy Technol. 4 (2016) 1582–1587.
[44] S.J. Lee, J.K. Lee, S.H. Chung, H.Y. Lee, S.M. Lee, H.K. Baik, Stress effect on cycle properties of the silicon thin-film anode, J. Power Sources. 97–98 (2001) 191–193.
[45] Y. Gwak, J. Moon, M. Cho, Multi-scale analysis of an electrochemical model including coupled diffusion, stress, and nonideal solution in a silicon thin film anode, J. Power Sources. 307 (2016) 856–865.
[46] K. Zhao, ES240 Final Project: FEM study on intercalation-induced stress level in amorphous Si thin film anode of Lithium-ion battery, Cambridge, 2008.
[47] S. Pal, S.S. Damle, P.N. Kumta, S. Maiti, Modeling of lithium segregation induced delamination of a-Si thin film anode in Li-ion batteries, Comput. Mater. Sci. 79 (2013) 877–887.
[48] J. Shaffer, P. Peralta, Finite element analysis of silicon thin films on soft substrates as anodes for lithium ion batteries, Arizona State Univesity, 2011.
[49] S.H. Patel, Numerical modeling of the failure mechanisms in Si thin film anode for Li-ion batteries, Michigan Technological University, 2011.

[50] B. Jerliu, E. Hüger, L. Dörrer, B.K. Seidlhofer, R. Steitz, V. Oberst, U. Geckle, M. Bruns, H. Schmidt, Volume expansion during lithiation of amorphous silicon thin film electrodes studied by in-operando neutron reflectometry, J. Phys. Chem. C. 118 (2014) 9395–9399.
[51] C. Pereira-Nabais, J. Światowska, M. Rosso, F. Ozanam, A. Seyeux, A. Gohier, P. Tran-Van, M. Cassir, P. Marcus, Effect of lithiation potential and cycling on chemical and morphological evolution of si thin film electrode studied by ToF-SIMS, ACS Appl. Mater. Interfaces. 6 (2014) 13023–13033.
[52] R. Ruffo, S.S. Hong, C.K. Chan, R.A. Huggins, Y. Cui, Impedance analysis of silicon nanowire lithium ion battery anodes, J.Phys.Chem.C. 113 (2009) 11390–11398.
[53] H. Xia, S. Tang, L. Lu, Properties of amorphous Si thin film anodes prepared by pulsed laser deposition, Mater. Res. Bull. 42 (2007) 1301–1309.
[54] A.A. Arie, J.K. Lee, Estimation of Li-ion diffusion coefficients in C60 coated Si thin film anodes using electrochemical techniques, Defect Diffus. Forum. 326–328 (2012) 87–92.
[55] H. Jung, M. Park, S.H. Han, H. Lim, S.K. Joo, Amorphous silicon thin-film negative electrode prepared by low pressure chemical vapor deposition for lithium-ion batteries, Solid State Commun. 125 (2003) 387–390.
[56] H. Jung, M. Park, Y.G. Yoon, G.B. Kim, S.K. Joo, Amorphous silicon anode for lithium-ion rechargeable batteries, J. Power Sources. 115 (2003) 346–351.
[57] J.P. Maranchi, a. F. Hepp, a. G. Evans, N.T. Nuhfer, P.N. Kumta, Interfacial properties of the a-Si/Cu: active–inactive thin-film anode system for lithium-ion batteries, J. Electrochem. Soc. 153 (2006) A1246–A1253.
[58] U. Tocoglu, T. Cetinkaya, O. Cevher, M.O. Guler, H. Akbulut, Nanostructured silicon thin film electrodes for Li-ion batteries, Acta Phys. Pol. A. 123 (2013) 380–382.
[59] T. Moon, C. Kim, B. Park, Electrochemical performance of amorphous-silicon thin films for lithium rechargeable batteries, J. Power Sources. 155 (2006) 391–394.
[60] M.S. Park, G.X. Wang, H.K. Liu, S.X. Dou, Electrochemical properties of Si thin film prepared by pulsed laser deposition for lithium ion micro-batteries, Electrochim. Acta. 51 (2006) 5246–5249.
[61] R.S. Omampuliyur, M. Bhuiyan, Z. Han, Z. Jing, L. Li, E.A. Fitzgerald, C. V Thompson, W.K. Choi, Nanostructured thin film silicon anodes for Li-ion microbatteries, J. Nanosci. Nanotechnol. 15 (2015) 4926–4933.
[62] J. Li, A.K. Dozier, Y. Li, F. Yang, Y.-T. Cheng, Crack pattern formation in thin film lithium-ion battery electrodes, J. Electrochem. Soc. 158 (2011) A689–A694.
[63] S. Ohara, J. Suzuki, K. Sekine, T. Takamura, Li insertion/extraction reaction at a Si film evaporated on a Ni foil, J. Power Sources. 119–121 (2003) 591–596.
[64] S. Ohara, J. Suzuki, K. Sekine, T. Takamura, A thin film silicon anode for Li-ion batteries having a very large specific capacity and long cycle life, J. Power

Sources. 136 (2004) 303–306.
[65] A.A. Arie, J.K. Lee, Electrochemical properties of P-doped silicon thin film anodes of lithium ion batteries, 737 (2013) 80–84.
[66] V. Baranchugov, E. Markevich, E. Pollak, G. Salitra, D. Aurbach, Amorphous silicon thin films as a high capacity anodes for Li-ion batteries in ionic liquid electrolytes, Electrochem. Commun. 9 (2007) 796–800.
[67] J.-K. Kim, G.-B. Cho, H.-S. Ryu, H.-J. Ahn, K.-K. Cho, K.-W. Kim, A. Matic, P. Jacobsson, J.-H. Ahn, Electrochemical properties of a full cell of lithium iron phosphate cathode using thin amorphous silicon anode, Solid State Ionics. 268 (2014) 256–260.
[68] M.T. Demirkan, L. Trahey, T. Karabacak, Cycling performance of density modulated multilayer silicon thin film anodes in Li-ion batteries, J. Power Sources. 273 (2015) 52–61.
[69] K.L. Lee, J.Y. Jung, S.W. Lee, H.S. Moon, J.W. Park, Electrochemical characteristics of a-Si thin film anode for Li-ion rechargeable batteries, J. Power Sources. 129 (2004) 270–274.
[70] S.K.J. H. X. Deng, C. Y. Chung, M. Park, C.H. Park, Effect of substrate surface conditions on electrochemical performance of Si thin film anode, ECS Trans. 2 (2007) 105–112.
[71] M. Uehara, J. Suzuki, K. Tamura, K. Sekine, T. Takamura, Thick vacuum deposited silicon films suitable for the anode of Li-ion battery, J. Power Sources. 146 (2005) 441–444.
[72] T. Zhang, H.P. Zhang, L.C. Yang, B. Wang, Y.P. Wu, T. Takamura, The structural evolution and lithiation behavior of vacuum-deposited Si film with high reversible capacity, Electrochim. Acta. 53 (2008) 5660–5664.
[73] M. Wang, Z. Geng, Facile synthesis of multilayer-like Si thin film as high-performance anode materials for lithium-ion batteries, Appl. Phys. A. 122 (2016) 528.
[74] G. Cho, J. Noh, H. Sung, S. Lee, Y. Im, H. Ahn, K. Kim, Patterned Si thin film electrodes for enhancing structural stability, Nanoscale Res. Lett. 7 (2012) 20.
[75] G.B. Cho, J.P. Noh, H.J. Sung, S.Y. Choi, S.H. Lee, H.J. Ahn, T.H. Nam, K.W. Kim, Improved electrochemical properties of patterned Si film electrodes, Microelectron. Eng. 89 (2012) 104–108.
[76] X. Xiao, P. Liu, M.W. Verbrugge, H. Haftbaradaran, H. Gao, Improved cycling stability of silicon thin film electrodes through patterning for high energy density lithium batteries, J. Power Sources. 196 (2011) 1409–1416.
[77] G.B. Cho, J.K. Kim, S.H. Lee, G. Kim, J. Noh, K. Cho, K. Kim, T. Nam, H. Ahn, Facile fabrication of patterned Si film electrodes containing trench-structured Cu current collectors for thin-film batteries, Electrochim. Acta. 224 (2017) 649–659.
[78] J.-S. Jeong, M.-R. Chae, H.-B. Park, Y.-M. Im, H.-J. Ahn, T.-H. Nam, K.-W. Kim, G.-B. Cho, Annealing effect on electrochemical properties of patterned Si film electrodes for thin-film batteries, Curr. Appl. Phys. (2017) 1–5.

[79] C. Yu, X. Li, T. Ma, J. Rong, R. Zhang, J. Shaffer, Y. An, Q. Liu, B. Wei, H. Jiang, Silicon thin films as anodes for high-performance lithium-ion batteries with effective stress relaxation, Adv. Energy Mater. 2 (2012) 68–73.
[80] L. Baggetto, D. Danilov, P.H.L. Notten, Honeycomb-structured silicon: Remarkable morphological changes induced by electrochemical (De)lithiation, Adv. Mater. 23 (2011) 1563–1566.
[81] X. Wang, L. Huang, Y. Zhang, F. Yin, Z. Bakenov, N. Umirov, M. Jin, G. Zhou, Novel silicon nanowire film on copper foil as high performance anode for lithium-ion batteries, Ionics (Kiel). 24 (2018) 373–378.
[82] S. Fujitani, H. Yagi, K. Sayama, T. Yoshida, K. Tarui, New a-Si alloy thin film anode with self organized micro columnar structure, in: Electrochem. Soc., 2003: p. 1.
[83] M. Ge, J. Rong, X. Fang, C. Zhou, Porous doped silicon nanowires for lithium ion battery anode with long cycle life, Nano Lett. 12 (2012) 2318–2323.
[84] R. Lin, S. Zhang, Z. Du, H. Fang, Y. Ren, X. Wu, Copper nanowires based current collector for light-weight and flexible composite silicon anode with high stability and specific capacity, RSC Adv. 5 (2015) 87090–87097.
[85] F. Dogan, L.D. Sanjeewa, S.J. Hwu, J.T. Vaughey, Electrodeposited copper foams as substrates for thin film silicon electrodes, Solid State Ionics. 288 (2015) 204–206.
[86] A. Mukanova, A. Nurpeissova, S.S. Kim, M. Myronov, Z. Bakenov, N-type doped silicon thin film on a porous Cu current collector as the negative electrode for Li-ion batteries, ChemistryOpen. 7 (2018) 92–96.
[87] X.H. Huang, J.B. Wu, Y.Q. Cao, P. Zhang, Y. Lin, R.Q. Guo, Cobalt nanosheet arrays supported silicon film as anode materials for lithium ion batteries, Electrochim. Acta. 203 (2016) 213–220.
[88] X. Chen, K. Gerasopoulos, J. Guo, A. Brown, C. Wang, R. Ghodssi, J.N. Culver, A patterned 3D silicon anode fabricated by electrodeposition on a virus-structured current collector, Adv. Funct. Mater. 21 (2011) 380–387.
[89] J.O. Song, H.T. Shim, D.J. Byun, J.K. Lee, A study on the effect of structure and P-doping of Si thin film as an anode for lithium rechargeable batteries, Adv. Nanomater. Process. 124–126 (2007) 1063–1066.
[90] H.J. Ahn, Y.S. Kim, W.B. Kim, Y.E. Sung, T.Y. Seong, Formation and characterization of Cu-Si nanocomposite electrodes for rechargeable Li batteries, J. Power Sources. 163 (2006) 211–214.
[91] B.D. Polat, O.L. Eryilmaz, O. Keles, A. Erdemir, K. Amine, Compositionally graded SiCu thin film anode by magnetron sputtering for lithium ion battery, Thin Solid Films. 596 (2015) 190–197.
[92] C.M. Hwang, C.H. Lim, J.H. Yang, J.W. Park, Electrochemical properties of negative SiMox electrodes deposited on a roughened substrate for rechargeable lithium batteries, J. Power Sources. 194 (2009) 1061–1067.
[93] J.B. Kim, H.Y. Lee, K.S. Lee, S.H. Lim, S.M. Lee, Fe/Si multi-layer thin film anodes for lithium rechargeable thin film batteries, Electrochem. Commun. 5 (2003) 544–548.

[94] J.B. Kim, B.S. Jun, S.M. Lee, Improvement of capacity and cyclability of Fe/Si multilayer thin film anodes for lithium rechargeable batteries, Electrochim. Acta. 50 (2005) 3390–3394.
[95] Q. Zhang, J. Liu, Z.Y. Wu, J.T. Li, L. Huang, S.G. Sun, 3D nanostructured multilayer Si/Al film with excellent cycle performance as anode material for lithium-ion battery, J. Alloys Compd. 657 (2016) 559–564.
[96] H. Liu, M. Zhu, Z. Du, M.N. Obrovac, The electrochemistry of amorphous Si-B thin film electrodes in Li cells, J. Electrochem. Soc. 163 (2015) A192–A196.
[97] H. Li, H. Bai, Z. Tao, J. Chen, Si-Y multi-layer thin films as anode materials of high-capacity lithium-ion batteries, J. Power Sources. 217 (2012) 102–107.
[98] S. Guo, H. Li, H. Bai, Z. Tao, J. Chen, Ti/Si/Ti sandwich-like thin film as the anode of lithium-ion batteries, J. Power Sources. 248 (2014) 1141–1148.
[99] Z. Wen, F. Tian, Cu-doped silicon film as anode for lithium ion batteries prepared by ion-beam sputtering, Int. J. Electrochem. Sci. 8 (2013) 10129–10137.
[100] Y.H. Wang, Y. He, R.J. Xiao, H. Li, K.E. Aifantis, X.J. Huang, Investigation of crack patterns and cyclic performance of Ti-Si nanocomposite thin film anodes for lithium ion batteries, J. Power Sources. 202 (2012) 236–245.
[101] V.A. Sethuraman, K. Kowolik, V. Srinivasan, Increased cycling efficiency and rate capability of copper-coated silicon anodes in lithium-ion batteries, J. Power Sources. 196 (2011) 393–398.
[102] S. Hieu, N.J. Lim, Improving the performance of silicon anode in lithium-ion batteries by Cu2O coating layer, J Appl Electrochem. 44 (2014) 353–360.
[103] M.K. Datta, J. Maranchi, S.J. Chung, R. Epur, K. Kadakia, P. Jampani, P.N. Kumta, Amorphous silicon-carbon based nano-scale thin film anode materials for lithium ion batteries, Electrochim. Acta. 56 (2011) 4717–4723.
[104] N. Garino, E. Biserni, A.L. Bassi, P. Bruno, C. Gerbaldi, Mesoporous Si and multi-layered Si/C films by pulsed laser deposition as Li-ion microbattery anodes, J. Electrochem. Soc. 162 (2015) A1816–A1822.
[105] A.A. Arie, J.O. Song, J.K. Lee, Structural and electrochemical properties of fullerene-coated silicon thin film as anode materials for lithium secondary batteries, Mater. Chem. Phys. 113 (2009) 249–254.
[106] E. Biserni, M. Xie, R. Brescia, A. Scarpellini, M. Hashempour, P. Movahed, S.M. George, M. Bestetti, A. Li Bassi, P. Bruno, Silicon algae with carbon topping as thin-film anodes for lithium-ion microbatteries by a two-step facile method, J. Power Sources. 274 (2015) 252–259.
[107] C. Wu, C. Chang, J. Duh, Silicon nitride coated silicon thin fi lm on three dimensions current collector for lithium ion battery anode, J. Power Sources. 325 (2016) 64–70.
[108] A.A. Arie, J.O. Song, J.K. Lee, Structural and electrochemical properties of fullerene-coated silicon thin film as anode materials for lithium secondary batteries, Mater. Chem. Phys. 113 (2009) 249–254.
[109] M. Haro, V. Singh, S. Steinhauer, E. Toulkeridou, Nanoscale heterogeneity of multilayered Si anodes with embedded nanoparticle scaffolds for Li-ion

batteries, Adv. Sci. 1700180 (2017) 1700180.
[110] Y. Tong, Z. Xu, C. Liu, G. Zhang, J. Wang, Z.G. Wu, Magnetic sputtered amorphous Si/C multilayer thin films as anode materials for lithium ion batteries, J. Power Sources. 247 (2014) 78–83.
[111] K. Xu, Y. He, L. Ben, H. Li, X. Huang, Enhanced electrochemical performance of Si-Cu-Ti thin films by surface covered with Cu3Si nanowires, J. Power Sources. 281 (2015) 455–460.
[112] J. Brumbarov, J. Kunze-Liebhäuser, Silicon on conductive self-organized TiO2 nanotubes – A high capacity anode material for Li-ion batteries, J. Power Sources. 258 (2014) 129–133.
[113] J. Lin, J. Guo, C. Liu, H. Guo, Artificial solid electrolyte interphase with in-situ formed porosity for enhancing lithiation of silicon wafer, J. Power Sources. 336 (2016) 401–407.
[114] G. Radhakrishnan, P.M. Adams, B. Foran, M. V. Quinzio, M.J. Brodie, Pulsed laser deposited Si on multilayer graphene as anode material for lithium ion batteries, APL Mater. 1 (2013) 062103.
[115] U. Toçoğlu, G. Hatipoğlu, M. Alaf, F. Kayış, H. Akbulut, Electrochemical characterization of silicon/graphene/MWCNT hybrid lithium-ion battery anodes produced via RF magnetron sputtering, Appl. Surf. Sci. 389 (2016) 507–513.
[116] A. Mukanova, A. Nurpeissova, A. Urazbayev, S. Kim, M. Myronov, Z. Bakenov, Silicon thin film on graphene coated nickel foam as an anode for Li-ion batteries, Electrochim. Acta. 258 (2017) 800–806.
[117] K.F. Chiu, S.H. Su, H.J. Leu, C.Y. Wu, Silicon thin film anodes coated on micron carbon-fiber current collectors for lithium ion batteries, Surf. Coatings Technol. 267 (2015) 70–74.
[118] Y.Q. Zhang, X.H. Xia, X.L. Wang, Y.J. Mai, S.J. Shi, Y.Y. Tang, L. Li, J.P. Tu, Silicon / graphene-sheet hybrid fi lm as anode for lithium ion batteries, Electrochem. Commun. 23 (2012) 17–20.
[119] H. Sun, A.E.D.R. Castillo, S. Monaco, A. Capasso, A. Ansaldo, M. Prato, D.A. Dinh;, V. Pellegrini, B. Scrosati, L. Manna, F. Bonaccorso, Binder-free graphene as advanced anode for lithium batteries Haiyan, J. Mater. Chem. A. 4 (2016) 6886–6895.
[120] F.J. Sonia, M.K. Jangid, B. Ananthoju, M. Aslam, P. Johari, A. Mukhopadhyay, Understanding the Li-storage in few layers graphene with respect to bulk graphite : experimental , analytical and computational study, J. Mater. Chem. A Mater. Energy Sustain. 5 (2017) 8662–8679.
[121] T.M. Paronyan, A.K. Thapa, A. Sherehiy, J.B. Jasinski, J.S.D. Jangam, Incommensurate graphene foam as a high capacity lithium intercalation anode, Sci. Rep. 7 (2017) 39944.
[122] Y. Chikhray, T. Kulsartov, V. Shestakov, I. Kenzhina, S. Askerbekov, J. Sumita, S. Ueta, T. Shibata, N. Sakaba, K. Abdullin, R. Nemkayeva, Corrosion test of HTGR graphite with SiC coating, in: Int. Top. Meet. High Temp. React. Technol., 2016: pp. 572–577.

[123] C.R. Stoldt, M.C. Fritz, C. Carraro, R. Maboudian, Micromechanical properties of silicon-carbide thin films deposited using single-source chemical-vapor deposition, Appl. Phys. Lett. 79 (2001) 347–349.
[124] Sadao Adachi, Cubic Silicon Carbide (3C-SiC), in: Opt. Constants Cryst. Amorph. Semicond., Springer US, 1999: pp. 63–72.
[125] P.A.A. V.S. Zakhvalinskii, E.A. Piljuk, I.Yu. Goncharov, V.G. Rodriges, A.P. Kuzmenko, S.V. Taran, RF magnetron sputtering of silicon carbide and silicon nitride films for solar cells, J. Nano Electron. Physocs. 6 (2014) 13–14.
[126] M. Shiratani, K. Kamataki, G. Uchida, K. Koga, H. Seo, N. Itagaki, T. Ishihara, SiC nanoparticle composite anode for Li-ion batteries, MRS Proc. 1678 (2014) 1–5.
[127] S.W. Lee, B.M. Gallant, H.R. Byon, P.T. Hammond, Y. Shao-Horn, Nanostructured carbon-based electrodes: bridging the gap between thin-film lithium-ion batteries and electrochemical capacitors, Energy Environ. Sci. 4 (2011) 1972.
[128] F. Li, Y. Sharma, V. Shah, M. Jennings, A. Pérez-tomás, M. Myronov, C. Fisher, D. Leadley, P. Mawby, Electrical activation of nitrogen heavily implanted 3C-SiC (100), Appl. Surf. Sci. 353 (2015) 958–963.
[129] T. Ayalew, SiC semiconductor devices technology, modeling, and simulation, Technischen Universität Wien, 2004.
[130] M. Choi, Y. Xiao, J. Hwang, I. Belharouak, Y. Sun, Novel strategy to improve the Li-storage performance of micro silicon anodes, J. Power Sources. 348 (2017) 302–310.
[131] J. Liang, X. Li, Z. Hou, W. Zhang, Y. Zhu, Y. Qian, A deep reduction and partial oxidation strategy for fabrication of mesoporous Si anode for lithium ion batteries, ACS Nano. 10 (2016) 2295–2304.
[132] C.K. Chan, R. Ruffo, S.S. Hong, Y. Cui, Surface chemistry and morphology of the solid electrolyte interphase on silicon nanowire lithium-ion battery anodes, J. Power Sources. 189 (2009) 1132–1140.
[133] N.S. Choi, K.H. Yew, H. Kim, S.S. Kim, W.U. Choi, Surface layer formed on silicon thin-film electrode in lithium bis(oxalato) borate-based electrolyte, J. Power Sources. 172 (2007) 404–409.
[134] N.S. Choi, K.H. Yew, K.Y. Lee, M. Sung, H. Kim, S.S. Kim, Effect of fluoroethylene carbonate additive on interfacial properties of silicon thin-film electrode, J. Power Sources. 161 (2006) 1254–1259.
[135] K. Fridman, R. Sharabi, R. Elazari, G. Gershinsky, E. Markevich, G. Salitra, D. Aurbach, A. Garsuch, J. Lampert, A new advanced lithium ion battery: Combination of high performance amorphous columnar silicon thin film anode, 5 V LiNi0.5Mn1 5O 4 spinel cathode and fluoroethylene carbonate-based electrolyte solution, Electrochem. Commun. 33 (2013) 31–34.
[136] L. Chen, K. Wang, X. Xie, J. Xie, Enhancing electrochemical performance of silicon film anode by vinylene carbonate electrolyte additive, Electrochem. Solid-State Lett. 9 (2006) A512–A515.
[137] T.L. Kulova, Irreversible capacity of the amorphous silicon thin-film

electrodes, Russ. J. Electrochem. 44 (2008) 525–529.
[138] S.-W. Song, S.-W. Baek, Silane-derived SEI stabilization on thin-film electrodes of nanocrystalline Si for lithium batteries, Electrochem. Solid-State Lett. 12 (2009) A23–A27.
[139] Y.-G. Ryu, S. Lee, S. Mah, D.J. Lee, K. Kwon, S. Hwang, S. Doo, Electrochemical behaviors of silicon electrode in lithium salt solution containing alkoxy silane additives, J. Electrochem. Soc. 155 (2008) A583–A589.
[140] K. Takada, Progress and prospective of solid-state lithium batteries, Acta Mater. 61 (2013) 759–770.
[141] S. Ohta, T. Kobayashi, J. Seki, T. Asaoka, Electrochemical performance of an all-solid-state lithium ion battery with garnet-type oxide electrolyte, J. Power Sources. 202 (2012) 332–335.
[142] J.W. Fergus, Ceramic and polymeric solid electrolytes for lithium-ion batteries, J. Power Sources. 195 (2010) 4554–4569.
[143] M.S. Whittingham, Lithium batteries and cathode materials, Chem. Rev. 104 (2004) 4271–4301.
[144] R. Miyazaki, N. Ohta, T. Ohnishi, K. Takada, Anode properties of silicon-rich amorphous silicon suboxide fi lms in all-solid-state lithium batteries, J. Power Sources. 329 (2016) 41–49.
[145] J.F.M. Oudenhoven, L. Baggetto, P.H.L. Notten, All-solid-state lithium-ion microbatteries: A review of various three-dimensional concepts, Adv. Energy Mater. 1 (2011) 10–33.
[146] L. Baggetto, R.A.H. Niessen, F. Roozehoom, P.H.L. Notten, High energy density all-solid-state batteries: A challenging concept towards 3D integration, Adv. Funct. Mater. 18 (2008) 1057–1066.
[147] F. Le Cras, B. Pecquenard, V. Dubois, V.P. Phan, D. Guy-Bouyssou, All-solid-state lithium-ion microbatteries using silicon nanofilm anodes: high performance and memory effect, Adv. Energy Mater. 5 (2015) 1501061.
[148] V.P. Phan, B. Pecquenard, F. Le Cras, High-performance all-solid-state cells fabricated with silicon electrodes, Adv. Funct. Mater. 22 (2012) 2580–2584.
[149] C. Gong, D. Ruzmetov, A. Pearse, D. Ma, J.N. Munday, G. Rubloff, A.A. Talin, M.S. Leite, Surface/interface effects on high-performance thin-film all-solid-state Li-ion batteries, ACS Appl. Mater. Interfaces. 7 (2015) 26007–26011.
[150] A.A. Talin, D. Ruzmetov, A. Kolmakov, K. McKelvey, N. Ware, F. El Gabaly, B. Dunn, H.S. White, Fabrication, testing, and simulation of all-solid-state three-dimensional Li-ion batteries, ACS Appl. Mater. Interfaces. 8 (2016) 32385–32391.
[151] J.W. Fergus, Ceramic and polymeric solid electrolytes for lithium-ion batteries, J. Power Sources. 195 (2010) 4554–4569.
[152] S. Ohta, T. Kobayashi, J. Seki, T. Asaoka, Electrochemical performance of an all-solid-state lithium ion battery with garnet-type oxide electrolyte, J. Power Sources. 202 (2012) 332–335.

[153] S. Swann, Magnetron sputtering, Phys. Technol. 19 (1988) 67–75.
[154] Ion beam sputter deposition, PolygonPhysics. (2016).
[155] D. Bäuerle, R. Rössler, J. Pedarnig, S.H. Yun, R. Dinu, N. Arnold, Pulsed laser deposition, Appl. Phys. A Mater. Sci. Process. 69 (1999) S45–S48.
[156] W. Schwarzacher, Electrodeposition: A Technology for the Future, Electrochem. Soc. Interface. 15 (2006) 32–35.
[157] R. Epur, M. Ramanathan, F.R. Beck, A. Manivannan, P.N. Kumta, Electrodeposition of amorphous silicon anode for lithium ion batteries, Mater. Sci. Eng. B. 177 (2012) 1157–1162.
[158] B. Gattu, R. Epur, P.M. Shanti, P.H. Jampani, Pulsed current electrodeposition of silicon thin films anodes for lithium ion battery applications, Inorganics Artic. 5 (2017) 1–14.
[159] C.A. Vlaic, S. Ivanov, R. Peipmann, A. Eisenhardt, M. Himmerlich, S. Krischok, A. Bund, Electrochemical lithiation of thin silicon based layers potentiostatically deposited from ionic liquid, Electrochim. Acta. 168 (2015) 403–413.
[160] G. Ferraresi, L. Czornomaz, C. Villevieille, P. Novak, M. El Kazzi, Elucidating the surface reactions of an amorphous Si thin film as a model electrode for Li-ion batteries, ACS Appl. Mater. Interfaces. 8 (2016) 29791–29798.
[161] J. Brumbarov, J. Kunze-Liebhäuser, Silicon on conductive self-organized TiO2 nanotubes – A high capacity anode material for Li-ion batteries, J. Power Sources. 258 (2014) 129–133.
[162] N. Elgrishi, K.J. Rountree, B.D. McCarthy, E.S. Rountree, T.T. Eisenhart, J.L. Dempsey, A practical beginner's guide to cyclic voltammetry, J. Chem. Educ. 95 (2018) 197–206.
[163] N. Loeffler, D. Bresser, S. Passerini, Secondary lithium-ion battery anodes: from first commercial batteries to recent research activities, Johnson Matthey Technol. Rev. 59 (2015) 34–44.
[164] G. Oltean, N. Plylahan, C. Ihrfors, W. Wei, C. Xu, K. Edström, L. Nyholm, P. Johansson, T. Gustafsson, Towards Li-ion batteries operating at 80 °C: ionic liquid versus conventional liquid electrolytes, Batteries. 4 (2018) 2.
[165] E.M.F. Vieira, J.F. Ribeiro, M.M. Silva, L. Dupont, J.H. Correia, L.M. Goncalves, Flexible solid-state Li – ion battery using Ge thin film anode and LiCoO2 cathode, in: 26th Micromechanics Microsystems Eur. Conf., 2015: pp. 1–4.
[166] Y. Chatillon, C. Bonnet, F. Lapicque, Differential capacity plot as a tool for determination of electroactive surface area within a PEMFC stack, J. Appl. Electrochem. 43 (2013) 1017–1026.
[167] M.J. Loveridge, M.J. Lain, I.D. Johnson, A. Roberts, S.D. Beattie, R. Dashwood, J.A. Darr, R. Bhagat, Towards high capacity Li-ion batteries based on silicon-graphene compositeanodes and sub-micron V-doped LiFePO4 cathodes, Sci. Rep. 6 (2016) 1–11.
[168] Y. Yang, X. Liu, Z. Dai, F. Yuan, Y. Bando, D. Golberg, X. Wang, In situ

electrochemistry of rechargeable battery materials: status report and perspectives, Adv. Mater. 29 (2017) 1–22.
[169] P.P.R.M.L. Harks, F.M. Mulder, P.H.L. Notten, In situ methods for Li-ion battery research : A review of recent developments, J. Power Sources. 288 (2015) 92–105.
[170] G.V. Zaia, Epitaxial growth of Si and 3C-SiC by chemical vapor deposition, Technische Universität München Epitaxial, 2002.
[171] R. Anzalone, A. Severino, G. D'Arrigo, C. Bongiorno, G. Abbondanza, G. Foti, S. Saddow, F. La Via, Heteroepitaxy of 3C -SiC on different on-axis oriented silicon substrates, J. Appl. Phys. 105 (2009) 084910.
[172] O. Kordina, A. Henry, E. Janzén, SiC epitaxial growth on large area substrates: History and evolution, Research Signpost, 2012.
[173] G. Colston, S.D. Rhead, V.A. Shah, O.J. Newell, I.P. Dolbnya, D.R. Leadley, M. Myronov, Mapping the strain state of 3C-SiC / Si (001) suspended structures using μ-XRD, Mater. Sci. Forum. 858 (2016) 274–277.
[174] M. Myronov, G. Colston, S. Rhead, Growing epitaxial 3C-SiC on single-crystal silicon, EP 3 325 695 A1, 2017.
[175] J. Ruska, The quantitative calculation of SiC polytypes from measurements of X- ray diffraction peak intensities, J. Mater. Sci. 14 (1979) 2013–2017.
[176] C.J. A.Gupta, D. Paramanik, S. Varma, CVD growth and characterization of 3C-SiC thin films, Bull.Mater.Sci. 27 (2004) 445–451.
[177] J. V Anguita, J. Purans, A. Kuzmin, A. Jorio, M.A. Pimenta, Raman spectra of silicon carbide small particles and nanowires, J. Phys. Condens. Matter. 17 (2005) 2387–2395.
[178] M. Hundhausen, R. Püsche, J. Röhrl, L. Ley, Characterization of defects in silicon carbide by raman spectroscopy, Basic Solid State Phys. 1368 (2008) 1356–1368.
[179] D. Talwar, L. Wan, C. Tin, Z. Feng, Assessing biaxial stress and strain in 3C-SiC/Si (001) by Raman scattering spectroscopy, J. Mater. Sci. Eng. 06 (2017) 1–8.
[180] J.H. Boo, S.B. Lee, K.S. Yu, M.M. Sung, Y. Kim, High vacuum chemical vapor deposition of cubic SiC thin films on Si(001) substrates using single source precursor, Surf. Coatings Technol. 131 (2000) 147–152.
[181] C.K. Jung, D.C. Lim, H.G. Jee, M.G. Park, S.J. Ku, K.S. Yu, B. Hong, S.B. Lee, J.H. Boo, Hydrogenated amorphous and crystalline SiC thin films grown by RF-PECVD and thermal MOCVD; comparative study of structural and optical properties, Surf. Coatings Technol. 171 (2003) 46–50.
[182] M.. Paridah, A. Moradbak, A.. Mohamed, F. abdulwahab taiwo Owolabi, M. Asniza, S.H.. Abdul Khalid, 3C-SiC — From Electronic to MEMS Devices, in: Adv. Silicon Carbide Devices Process. Hedral, InTech, 2015: p. 13.
[183] K. Kanamura, Y. Yamada, K. Annaka, N. Nakata, H. Munakata, Electrochemical evaluation of active materials for lithium ion batteries by one (single) particle measurement, Electrochem. Soc. Japan. 84 (2016) 759–765.
[184] D. (Central L. of E.P.S.-B.A. of S.) Vladikova, Materials for lithium-ion

batteries, in: C. Julien, Z. Stoynov (Eds.), Springer Science + Business Media, B.V., 2012: pp. 581–596.
[185] L.L. Tian, Q.C. Zhuang, J. Li, Y.L. Shi, J.P. Chen, F. Lu, S.G. Sun, Mechanism of intercalation and deintercalation of lithium ions in graphene nanosheets, Chinese Sci. Bull. 56 (2011) 3204–3212.
[186] H. Wu, G. Chan, J.W. Choi, I. Ryu, Y. Yao, M.T. McDowell, S.W. Lee, A. Jackson, Y. Yang, L. Hu, Y. Cui, Stable cycling of double-walled silicon nanotube battery anodes through solid–electrolyte interphase control, Nat. Nanotechnol. 7 (2012) 310–315.
[187] C. Chen, R. Agrawal, C. Wang, High performance Li4Ti5O12/Si composite anodes for Li-ion batteries, Nanomaterials. 5 (2015) 1469–1480.
[188] B.E. Conway, Electrochemical supercapacitors: scientific fundamentals and technological applications, Springer Science & Business Media, 2013.
[189] V.Z. Barsukov, V.G. Khomenko, S. V Chivikov, I. V Barsukov, On the faradaic and non-faradaic mechanisms of electrochemical processes in conducting polymers and some other reversible systems with solid-phase reagents, Electrochim. Acta. 46 (2001) 4083–4094.
[190] S. Amini, J. Garay, G. Liu, A.A. Balandin, R. Abbaschian, Growth of large-area graphene films from metal-carbon melts, J. Appl. Phys. 108 (2010) 1–21.
[191] C. Yang, Y. Yin, S. Zhang, N. Li, Y. Guo, Accommodating lithium into 3D current collectors with a submicron skeleton towards long-life lithium metal anodes, Nat. Commun. 6 (2015) 1–9.
[192] A. Mukanova, R. Tussupbayev, A. Sabitov, I. Bondarenko, R. Nemkaeva, B. Aldamzharov, Z. Bakenov, CVD graphene growth on a surface of liquid gallium, Mater. Today Proc. 4 (2017) 4548–4554.
[193] S.S. Nanda, M.J. Kim, K.S. Yeom, S.S. A.An, H. Ju, D.K. Yi, Raman spectrum of graphene with its versatile future perspectives, TrAC Trends Anal. Chem. 80 (2016) 125–131.
[194] A.C. Ferrari, J.C. Meyer, V. Scardaci, C. Casiraghi, M. Lazzeri, F. Mauri, S. Piscanec, D. Jiang, K.S. Novoselov, S. Roth, A.K. Geim, Raman spectrum of graphene and graphene layers, Phys. Rev. Lett. 97 (2006) 187401.
[195] Y. Hao, Y. Wang, L. Wang, Z. Ni, Z. Wang, R. Wang, C.K. Koo, Z. Shen, J.T.L. Thong, Probing layer number and stacking order of few-layer graphene by raman spectroscopy, Small. 6 (2010) 195–200.
[196] A.C. Ferrari, J. Robertson, P. Trans, R.S. Lond, Raman spectroscopy of amorphous, nanostructured, diamond − like carbon, and nanodiamond, Philos. Trans. R. Soc. A. 362 (2004) 2477–2512.
[197] Rattana, S.Chaiyakun, N.Witit-anun, N.Nuntawong, P.Chindaudom, S.Oaew, C.Kedkeaw, P.Limsuwand, Preparation and characterization of graphene oxide nanosheets, Procedia Eng. 32 (2012) 759–764.
[198] C.L. and G.S. Yuxi Xu, Hua Bai, Gewu Lu, Flexible graphene films via the filtration of water-soluble noncovalent functionalized graphene sheets, J. Am. Chem. Soc. 130 (2008) 5856–5857.
[199] Z. Chen, W. Ren, L. Gao, B. Liu, S. Pei, H. Cheng, Three-dimensional

flexible and conductive interconnected graphene networks grown by chemical vapour deposition, Nat. Mater. 10 (2011) 424–428.
[200] L. Baraton, Z.B. He, C.S. Lee, C.S. Cojocaru, M. Châtelet, J.-L. Maurice, Y.H. Lee, D. Pribat, On the mechanisms of precipitation of graphene on nickel thin films, 1 (2011) 1–6.
[201] D. Samsonov, J. Goree, Particle growth in a sputtering discharge, J. Vac. Sci. Technol. A Vacuum, Surfaces, Film. 17 (2002) 2835–2840.
[202] C. Li, C. Liu, W. Wang, Z. Mutlu, J. Bell, K. Ahmed, R. Ye, M. Ozkan, C.S. Ozkan, Silicon derived from glass bottles as anode materials for lithium ion full cell batteries, Sci. Rep. (2017) 1–11.
[203] J. Tarascon, P. Poizot, S. Laruelle, S. Grugeon, L. Dupont, Nano-sized transition-metal oxides as negative-electrode materials for lithium-ion batteries, Nature. 407 (2000) 496–499.
[204] R. Janssen, A. Janotta, Optical and electrical properties of doped amorphous silicon suboxides, Phys. Rev. B. 60 (1999) 13561–1357.
[205] S. Paulo, Electrical conductivity of amorphous silicon doped with rare-earth elements, Phys. Rev. B. 43 (1991) 8946–8950.
[206] T.S. Ameshima, N.A. Ndoh, Y.A. Ndoh, Activation Behavior of Boron and Phosphorus Atoms Implanted in Polycrystalline Silicon Films by Heat Treatment at 250 C, Jpn. J. Appl. Phys. 44 (2005) 1186–1191.
[207] D. Caputo, G. De Cesare, Activation of dopant in the p-layer of amorphous silicon solar cells under illumination, Sol. Energy Mater. Sol. Cells. 43 (1996) 263–272.
[208] P. Alpuim, V. Chu, R.A. Redol, J.P. Conde, Doping of amorphous and microcrystalline silicon films deposited at low substrate temperatures by hot-wire chemical vapor deposition, J. Vac. Sci. Technol. A. 19 (2001) 2328.
[209] Sijie Liu, N. Huo, S. Gan, Y. Li, Z. Wei, B. Huang, J. Liu, J. Li, H. Chen, Thickness-dependent Raman spectra, transport properties and infrared photoresponse of few-layer black phosphorus, J. Mater. Chem. C. 3 (2015) 10974.
[210] and S.I. N. Fukata, J. Chen, T. Sekiguchi, N. Okada, K. Murakami, T. Tsurui, Doping and hydrogen passivation of boron in silicon nanowires synthesized by laser ablation, Appl. Phys. Lett. 89 (2006) 203109.
[211] T.C. Yang, K. Nomoto, B. Puthen-veettil, Z. Lin, L. Wu, T. Zhang, Properties of silicon nanocrystals with boron and phosphorus doping fabricated via silicon rich oxide and silicon dioxide bilayers, Mater. Res. Express. 4 (2017) 075004.
[212] L.S. Hoyos, B. Faroldi, L. Cornaglia, Reactivity of rice husk-derived lithium silicates followed by in situ Raman spectroscopy, J. Alloys Compd. 778 (2019) 699–711.
[213] T. Seuthe, M. Grehn, J. Bonse, M. Eberstein, H.J. Eichler, A. Mermillod-Blondin, Structural modifications of binary lithium silicate glasses upon femtosecond laser pulse irradiation probed by micro-Raman spectroscopy, Opt. Mater. Express. 3 (2013) 755.

[214] A. Sifuentes, A.C. Stowe, N. Smyrl, Determination of the role of Li2O on the corrosion of lithium hydride, J. Alloys Compd. 580 (2013) S271–S273.
[215] S.M. Russell, O. Borodin, A. V. Cresce, J.A. Allen, J. Peng, K. Xu, M. Dai, M.P. Gobet, M.A. Schroeder, S.G. Greenbaum, R.E. Rogers, Solvation behavior of carbonate-based electrolytes in sodium ion batteries, Phys. Chem. Chem. Phys. 19 (2016) 574–586.
[216] F.S. Gittleson, K.P.C. Yao, D.G. Kwabi, S.Y. Sayed, W.H. Ryu, Y. Shao-Horn, A.D. Taylor, Raman Spectroscopy in Lithium-Oxygen Battery Systems, ChemElectroChem. 2 (2015) 1446–1457.
[217] R.S. Sánchez-Carrera, B. Kozinsky, Computational Raman spectroscopy of organometallic reaction products in lithium and sodium-based battery systems, Phys. Chem. Chem. Phys. 16 (2014) 24549–24558.
[218] K. Rajeshwar, Fundamentals of Semiconductor Electrochemistry and Photoelectrochemistry, in: A.J. Bard (Ed.), Encycl. Electrochem., Wiley-VCH Verlag GmbH & Co. KGaA, 2007.
[219] B.R. Long, M.K.Y. Chan, P. Greeley, A.A. Gewirth, Dopant modulated Li insertion in Si for battery anodes: theory and experiment, J. Phys. Chem. C. 115 (2011) 18916–18921.
[220] M. Lee, D. Yoon, U.J. Lee, N. Umirov, A. Mukanova, S. Kim, The electrochemical performances of n-type extended lattice spaced Si negative electrodes for lithium-ion batteries, Front. Chem. 7 (2019) 389.
[221] Y. Domi, H. Usui, M. Shimizu, Y. Kakimoto, H. Sakaguchi, Effect of phosphorus-doping on electrochemical performance of silicon negative electrodes in lithium-ion batteries, ACS Appl. Mater. Interfaces. 8 (2016) 7125–7132.
[222] J. Chai, Z. Liu, J. Ma, J. Wang, X. Liu, H. Liu, J. Zhang, G. Cui, L. Chen, In situ generation of poly (vinylene carbonate) based bolid electrolyte with interfacial stability for LiCoO2 lithium batteries, Adv. Sci. 4 (2017) 16000377.
[223] C.C. Nguyen, B.L. Lucht, Comparative study of fluoroethylene carbonate and vinylene carbonate for silicon anodes in lithium ion batteries, J. Electrochem. Soc. 161 (2014) A1933–A1938.
[224] H.H. Lee, Y.Y. Wang, C.C. Wan, M.H. Yang, H.C. Wu, D.T. Shieh, The function of vinylene carbonate as a thermal additive to electrolyte in lithium batteries, J. Appl. Electrochem. 35 (2005) 615–623.
[225] B. Zhang, M. Metzger, S. Solchenbach, M. Payne, S. Meini, H.A. Gasteiger, A. Garsuch, B.L. Lucht, Role of 1,3-propane sultone and vinylene carbonate in solid electrolyte interface formation and gas generation, J. Phys. Chem. C. 119 (2015) 11337–11348.
[226] X. Teng, C. Zhan, Y. Bai, L. Ma, Q. Liu, C. Wu, F. Wu, Y. Yang, J. Lu, K. Amine, In-situ analysis of gas generation in lithium ion batteries with different carbonate-based electrolytes., ACS Appl. Mater. Interfaces. 7 (2015) 22751–22755.
[227] D. Strmcnik, I.E. Castelli, J.G. Connell, D. Haering, M. Zorko, P. Martins, P.P. Lopes, B. Genorio, T. Østergaard, H.A. Gasteiger, F. Maglia, B.K.

Antonopoulos, V.R. Stamenkovic, J. Rossmeisl, N.M. Markovic, Electrocatalytic transformation of HF impurity to H2 and LiF in lithium-ion batteries, Nat. Catal. 1 (2018) 255–262.
[228] A. Rezqita, M. Sauer, A. Foelske, H. Kronberger, A. Trifonova, The effect of electrolyte additives on electrochemical performance of silicon/mesoporous carbon (Si/MC) for anode materials for lithium-ion batteries, Electrochim. Acta. 247 (2017) 600–609.
[229] A.M. Andersson, K. Edström, Chemical composition and morphology of the elevated temperature SEI on graphite, J. Electrochem. Soc. 148 (2002) A1100.
[230] L. El Ouatani, R. Dedryvère, C. Siret, P. Biensan, S. Reynaud, P. Iratçabal, D. Gonbeau, The effect of vinylene carbonate additive on surface film formation on both electrodes in Li-ion batteries, J. Electrochem. Soc. 156 (2008) A103.
[231] S.H. Lee, I.S. Jo, J. Kim, Surface analysis of the solid electrolyte interface formed by additives on graphite electrodes in Li-ion batteries using XPS, FE-AES, and XHR-SEM techniques, Surf. Interface Anal. 46 (2014) 570–576.
[232] G. Evmenenko, T.T. Fister, D.B. Buchholz, Q. Li, K.S. Chen, J. Wu, V.P. Dravid, M.C. Hersam, P. Fenter, M.J. Bedzyk, Morphological Evolution of Multilayer Ni/NiO Thin Film Electrodes during Lithiation, ACS Appl. Mater. Interfaces. 8 (2016) 19979–19986.
[233] P. Poizot, S. Laruelle, S. Grugeon, L. Dupont, J. Tarascon, Nano-sizedtransition-metaloxidesas negative-electrode materials for lithium-ion batteries, Nature. 407 (2000) 496–499.
[234] L. Cao, D. Wang, R. Wang, NiO thin fi lms grown directly on Cu foils by pulsed laser deposition as anode materials for lithium ion batteries, Mater. Lett. 132 (2014) 357–360.
[235] A.P. Cohn, L. Oakes, R. Carter, S. Chatterjee, A.S. Westover, K. Share, C.L. Pint, Assessing the improved performance of freestanding, flexible graphene and carbon nanotube hybrid foams for lithium ion battery anodes, Nanoscale. 6 (2014) 4669.
[236] F. Ding, W. Xu, D. Choi, W. Wang, X. Li, M.H. Engelhard, X. Chen, Z. Yang, J.-G. Zhang, Enhanced performance of graphite anode materials by AlF3 coating for lithium-ion batteries, J. Mater. Chem. 22 (2012) 12745.
[237] C. Pereira-Nabais, J. Światowska, A. Chagnes, F. Ozanam, A. Gohier, P. Tran-Van, C.S. Cojocaru, M. Cassir, P. Marcus, Interphase chemistry of Si electrodes used as anodes in Li-ion batteries, Appl. Surf. Sci. 266 (2013) 5–16.
[238] R. Ruffo, S.S. Hong, C.K. Chan, R.A. Huggins, Y. Cui, Impedance analysis of silicon nanowire lithium ion battery anodes, J. Phys. Chem. C. 113 (2009) 11390–11398.
[239] O.M. Vovk, B.K. Na, B.W. Cho, J.K. Lee, Electrochemical characteristics of amophous carbon coated silicon electrodes, Korean J. Chem. Eng. 26 (2009) 1034–1039.

APPENDIX 1

Table A1 – Literature data of the electrochemical properties of various a-Si thin film anode materials.

№	Thin film structure	Preparation method	Underlayer (nm)/ Substrate	Thickness (nm)	Cell (Electrolyte || Counter electrode)	Voltage range, Current/C-rate	Reversible discharge specific capacity (mAh g^{-1})	Number of cycles	Last discharge capacity (mAh g^{-1})	Ref.
1	monolithic Si	MS (rf, 150 W, 0.67 Pa)	Ti/Cu	35	1 M $LiPF_6$ / EC:DEC (1:1) || Li	0.1-5 V, 125 μA cm^{-2}	30 μAh	50	18 μAh	[44]
2	monolithic a-Si	MS (rf, 200W, 0.67 Pa)	Cu	250	1 M $LiPF_6$ / EC:DMC (2:1) || Li	0.02-1.2 V, C/2.5	3800	45	1800	[9,57]
				1000			3000	30	1250	
3	monolithic a-Si	MS (dc, 150 W, 0.5 Pa)	St. steel	400	1 M $LiPF_6$ / EC:DMC (NA) || Li	0.2-2 V, 800 mA g^{-1}	900	60	785	[58]
4	monolithic a-Si	MS (rf, 1.5 W/cm^2)	Cu	1000-2000	1 M $LiPF_6$ / EC:DMC (1:1) || Li	0.01-1 V, 100 μA cm^{-2}	1750	30	1500	[69]
5	monolithic a-Si	MS (rf, NA)	Cu	200	1 M $LiPF_6$ / EC:DEC (1:1) || Li	0.02-1.2 V, 0.5C	3200	70-200	3000-1300	[59]
6	monolithic a-Si	MS (rf, NA)	Cu	800			1300	10	1400	
7	monolithic a-Si	MS (rf, 60 W, 0.32 Pa)	Cu rough	275	1 M $LiPF_6$ / EC:DMC (1:1) + 1% VC || Li	0-1.5 V, 0.5C	2300	500	1700	[38]
8	monolithic a-Si	MS (dc, 0.67 Pa)	St. steel	100	1 M LiTFSI / MPPpTFSI || Li	3-4.3 V, C/16, C/10	3000	38	2750	[66]
9	monolithic a-Si	MS (rf, 0.4 Pa, 200 °C)	Cu rough	80	1 M $LiClO_4$ / EC:DEC (1:1) || Li	5 mV - 1 V, 0.5C	3000	80	2800	[70]
10	monolithic a-Si	MS (rf, 50 - 100 W)	Cu nanowires	NA	1 M $LiPF_6$ / EC:DEC (1:1) Li	0.01-1.5 V, 0.2C	2303	60	2060	[84]
11	monolithic a-Si	MS (rf, 100 W, 1 Pa)	St. steel	100	1 M $LiPF_6$ / EC:DMC (1:1) Li	0.002-2 V, C/10	3800	30	3400	[62]
				200			3300		2850	
				500			2000		1300	

№	Thin film structure	Preparation method	Underlayer (nm)/ Substrate	Thickness (nm)	Cell (Electrolyte || Counter electrode)	Voltage range, Current/C-rate	Reversible discharge specific capacity (mAh g^{-1})	Number of cycles	Last discharge capacity (mAh g^{-1})	Ref.
12	monolithic a-Si	ED ($SiCl_4$, - 3.4 V vs. Pt, Ar, 20 °C)	Cu foam	1500-4000	.3M LPF_6 / EC:EMC (3:7) Li	0.01-1.5 V, 50 μA cm^{-2}	~950	60	920	[85]
13	monolithic a-Si	LP-CVD (SiH_4/Ar/H_2, 200 sccm, 650 °C, 1333 Pa)	Ni porous (10-50 μm)	1200	M $LiPF_6$ / EC:DMC (1:1) Li	0.05-1.1 V, NA	1000	20	200	[28]
14	monolithic a-Si	CVD (Si_2H_6, 0.4 Pa, 450 °C)	Mo	~50	1 M $LiClO_4$ / PC || Li	0.1-3 V, 100 μA cm^{-2} 0.2-3 V, 250 μA cm^{-2}	3000 ~3200	75 90	~0 3000	[56]
15	monolithic a-Si	GD ($8 \cdot 10^{-4}$ Pa)	Ni	100	M $LiPF_6$ / EC:DMC (1:1) Li	0-1.5 V, NA	2500	50	1800	[27]
16	monolithic a-Si	ED ($SiCl_4$, - 1.6V vs. Pt, Ar, 20 °C)	Cu	300-1000	1M LPF_6 / EC:DEC (1:2) || Li	0.02-1.2 V, 400 mA g^{-1}	1300	100	1260	[157]
17	monolithic a-Si	EBE (10^{-4} Pa)	Cu rough	200	.3 M $LiPF_6$ / EC:DEC (3:7 + 3% FEC || Li	.05-2 V, 63.2 μAh cm^{-2}	3800	80	3450	[134]
18	monolithic c-Si	MS (rf, 200 W, $3.4 \cdot 10^{-4}$ Pa)	Cu	112 312	M $LiPF_6$ / EC:DMC (1:1) Li	0.01-1.5 V, 0.5C	4200 4000	25	3150	[37]
19	monolithic a-Si	EBE (10^{-4} Pa)	Cu	200	.3M $LiPF_6$ / EC/DEC (3:7 || Li 0.7M LiBOB / EC/DEC (3:7) || Li	0.05-2 V, 0.2C	3600 3600	100	1800 3000	[133]
20	monolithic a-Si	PLD (500 °C, 5 Hz, 25 ns, 67 Pa, 3 J cm^{-2})	St. steel	1500	1M LPF_6 / EC:DMC (1:1) | Li	0.005-1.5 V(NA)	19 μAh cm^{-2}	70	15 μAh cm^{-2}	[60]
21	monolithic a-Si	PLD (20 °C, 10 Hz, 10^{-2} Pa, 150-160 J cm^{-2})	St. steel	120	1M LPF_6 / EC:DEC (1:1) || Li	0-1.5 V, 100 μA cm^{-2}	58 μAh cm^{-2}	50	55 μAh cm^{-2}	[53]

№	Thin film structure	Preparation method	Underlayer (nm)/ Substrate	Thickness (nm)	Cell (Electrolyte || Counter electrode)	Voltage range, Current/C-rate	Reversible discharge specific capacity (mAh g^{-1})	Number of cycles	Last discharge capacity (mAh g^{-1})	Ref.
22	monolithic a-Si	MS (dc)	NA	6000	M $LiPF_6$ / FEC:DMC (1:4 || $LiNi_{0.5}Mn_{1.5}O_4$	0.01-1.2 V, C/8	140	150	125	[135]
23	monolithic a-Si	PED (5000 Hz)	Cu	NA	1 M $LiPF_6$ / EC:DEC:FEC (45:45:10) || Li	0.01–1.2 V, 0.3 A g^{-1}	1200	500	805	[158]
24	monolithic a-Si	LPCVD (Si_2H_6, 40 Pa and 450 °C)	Mo(300)/ quartz	50	1 M LiClO4 / PC | Li M LiClO4 / PC || $LiMn_2O$	0-1 V, 100 μA cm^{-2} 3-4.4 V, 100 μA cm^{-2}	1300 330	300 400	~400 330	[55]
25	monolithic a-Si	MS (dc, 0.34 W cm^{-2}, 0.5 Pa, Ar)	W(250)/Si wafer	120	Si | LIPON || LiTiOS	0.05-1 V, 2C	130 μAh cm^{-2}	1200	112 μAh cm^{-2}	[147]
26	monolithic a-Si	MS (0.67 Pa, Ar)	Cu annealed	330	1MLPF_6 / EC:DEC (1:1) || $LiFePO_4$/C	2.5-4.4 V, 1C	124	100	100	[67]
27	monolithic c-Si	BC ($2.6 \cdot 10^{-2}$ Pa, 10% H_2+ 90 % N_2)	Ni	100	M $LiPF_6$ / EC:DMC (1:1) Li	0-1.5 V, NA	1000	50	525	[27]
28	monolithic c-Si	PLD (0.67 Pa, 200 °C, 3–4 mJ/cm^2, 10 Hz)	St. steel	42	1M LPF_6 / EC:DEC (1:1) + 5 % $CH_3Si[OCH_3]_3$ || Li	0.1-1.5 V, 35 μA cm^{-2}, 1C	2900	200	2400	[138]
29	monolithic Si, *n*-type	IBD (rf, $4.5 \cdot 10^{-3}$ Pa)	Cu	150	1M $LiPF_6$ / EC:DMC (1:1) + 1% VC || Li	0-1.5 V, 0.05 mA cm^{-2}	2000	200	1900	[136]
30	monolithic a-Si, *n*-type	PE-CVD (rf, 120W/200W, 4 Pa/ 10.7Pa, PH_3/SiH_4/Ar, 200-400 °C)	Cu	425-540	1 M $LiPF_6$ / EC:DMC:DEC (1:1:1) || Li	0-1.5 V, 100 μA cm^{-2}	3800	50	2250	[89]
31	monolithic a-Si, *n*-type	MS DC (0.34 W cm^{-2}, 0.5 Pa, Ar 100%, 13 nm min^{-1})	Cu	100-400	1 M $LiPF_6$ / EC:PC:DMC (1:1:3) 2% of VC || Li	.05-1 V, 100 μAh cm^{-2} 2C	39 μAh cm-2	1500	38 μAh cm^{-2}	[148]

№	Thin film structure	Preparation method	Underlayer (nm)/ Substrate	Thickness (nm)	Cell (Electrolyte || Counter electrode)	Voltage range, Current/C-rate	Reversible discharge specific capacity (mAh g^{-1})	Number of cycles	Last discharge capacity (mAh g^{-1})	Ref.
32	monolithic a-Si, *n*-type	VE (NA)	Ni	50 150	1M $LiClO_4$ / PC || Li	0-2.5 V, 1C	3750 2500	200	3850 2200	[64]
33	monolithic Si, P-doped	VE (NA)	Ni rough	1000	1M $LiClO_4$ / PC || Li	NA	2700	200	1750	[71]
34	monolithic Si, P-doped	VE (NA)	Cu rough	3600		NA	2350	50	2100	
35	monolithic a-Si, P-doped	VE($1.3 \cdot 10^{-5}$ Pa)	Ni rough	50	1M $LiClO_4$ / PC || Li	0-2 V, 2C 12C 30C	 3600 3400 2300	 200 900 2500	 3600 3200 2200	[19]
36	monolithic a-Si, P-doped		Ni rough	300 440	1M $LiClO_4$ / PC || Li	0-2 V,1C	2300 2200	180 200	1900 2000	
37	monolithic a-Si, *n*-type	MS (rf, 85 W, 0.03 Pa)	St. steel	200 550 1.1	M $LiPF_6$ / EC:DEC (1:1) Li	0.01-3 V, 500 mA g^{-1}	4400 3100 3000	50	4200 1000 700	[61]
38	monolithic a-Si, *n*-type	MS (rf, 85 W, 0.03 Pa)	St. steel	140			4200	20	4200	
39	nanoporous a-Si, *n*-type	MS (rf, 85 W, 0.03 Pa)	Si/ St. steel	450 750			3200 3100	20	2800 2400	
40	nanopillars a-Si, *n*-type	MS (rf, 85 W, 0.03 Pa)	Si/ St. steel	450 750			4000 3500	50	3900 4000	
41	monolithic Si, P-doped	RF-PECVD (200W, 10.6 Pa, SiH_4+PH_3, 150 °C)	Cu	500-600	$LiCF_3SO_3$ / EC:PC / PAN:PVDF (gel-polymer) Li	0.001-1.5 V, 0.3 C	3150	50	2585	[65]

№	Thin film structure	Preparation method	Underlayer (nm)/ Substrate	Thickness (nm)	Cell (Electrolyte || Counter electrode)	Voltage range, Current/C-rate	Reversible discharge specific capacity (mAh g^{-1})	Number of cycles	Last discharge capacity (mAh g^{-1})	Ref.
42	monolithic a-Si, B-doped	VE ($1 \cdot 10^{-5}$ Pa,deposition rate of 0.1 nm /min)	Ni	77	1M $LiClO_4$ / PC || Li	0-2 V, 1 mV s^{-1}	1500	1250	1000	[63]
43	a-Si, Cu-doped	MS(rf, 60W, 0.67 Pa,	Cu	220	M $LiPF_6$ / EC:DEC (1:1) Li	0-2 V, 20 μA cm^{-2}	~410 μAh $cm^{-2} \cdot \mu m^{-1}$	40	~360 μAh $cm^{-2} \mu m^{-1}$	[90]
44	monolithic a-Si/Cu (non-graded)	MS (NA, Si/Cu - 2200 W/350 W)	St. steel	~3000	M $LiPF_6$ / EC:DMC (1:1) Li	0.2-1.2 V, C/12	1100	100	250	[91]
45	monolithic a-Si/Cu (graded)	MS (NA, Si/Cu - 50 W/350 W)					1400	100	600	
46	a-Si film, Cu-doped	IBD (2.5 kV, 40 mA)	Cu	10000	M $LiPF_6$ / EC:DMC (1:1) Li	0.02-1.5 V, NA	590	100	550	[99]
47	monolithic a-Si+O_2	MS (rf, 200 W, 0.45 Pa)	St. steel	50 300	70$Li_2S \cdot 30P_2S_5$ || Li	0.01-1.2 V, 0.1 mA cm^{-2}	2800 2800	100	2500 2000	[144]
48	a-Si + 20% C and 20% O_2	ED (SiCl4 in [BMP][TFSI], -2 V vs. Pt, Ar, 20 °C)	Cu	1000-1200	M $LiPF_6$ / EC:DMC (1:1) Li 1 M LiTFSI [BMP][TFSI] | Li	0.02-1.5 V, 0.1C	1200 600	120 90	1080 500	[159]
49	a-$SiMo_x$ alloy	MS (0.67 Pa, Ar)	Cu rough	4000	1M LPF_6 / EC:DMC (1:1) | Li	0.01-1 V, 714 μA cm^{-2} (0.2C)	1319	100	1180	[92]
50	monolithic a-Si:H	PE-CVD (rf, 250 °C, SiH_4, 13.56 MHz, 0.10 W cm^{-2}, 50 Pa and 33 sccm)	St. steel	30	1 M LiClO4 / PC || Li	0.125-2 V, 1C	3500	100	2250	[51] [237]

№	Thin film structure	Preparation method	Underlayer (nm)/ Substrate	Thickness (nm)	Cell (Electrolyte || Counter electrode)	Voltage range, Current/C-rate	Reversible discharge specific capacity (mAh g^{-1})	Number of cycles	Last discharge capacity (mAh g^{-1})	Ref.
51	monolithic c-Si:H	GD (hf, SiH_4, 100°C) GD (hf, SiH_4, 250°C)	St. steel	800 600	NA	NA	1000 1400	100	250 500	[40]
52	monolithic c-Si:H	GD (hf, SiH_4, 250°C)	St. steel	250	1M $LiClO_4$ / PC:DMC (7:3) || Li	0-1.2 V, 0.07 mA	2900	NA	NA	[137]
53	monolithic Si, 2-layer monolithic Si, 4-layer	MS (dc, 200 W, $1.5{\cdot}10^{-3}$ Pa/ $1.5{\cdot}10^{-4}$ Pa)	Cr(25)/Cu	190 380	1.2 M $LiPF_6$ / EC:EMC (3:7 || Li	0 mV-1.5 V, 40 μA/cm	~1800 ~2000	50	1392 1704	[68]
54	monolithic Si multilayer	MS (rf, 100 W, 1 Pa, periodic/constant bias)	Cr(10)/Cu	696 618	1 M $LiPF_6$ / EC:DEC (1:1) || Li	0.01-1 V, 0.2C	2050 1500	100	1905 600	[73]
55	lozenge-patterned Si	MS (dc, 0.67 Pa)	St. steel	350	1 M $LiPF_6$ / EC:DEC (1:1) || Li	0.01-1.2 V 0.5C	2200	120	1650	[74]
56	lozenge-patterned Si	MS (dc, 0.67 Pa)	St. steel rough	350	1 M $LiPF_6$ / EC:DMC (1:1) || Li	0.01-1.2 V, 0.2C	2250	100	2050	[75]
57	honeycombs a-Si	PE-CVD (rf, 350 W, 300 °C, SiH 4 + PH 3 + H 2, 1.6 mbar) + Lithography	TiN	1100	1M $LiClO_4$ / PC || Li	0.1-0.8 V, 75 μA cm^{-2}	52 μAh cm^{-2}	70	32 μAh cm^{-2}	[80]
58	hills-like a-Si	VE ($7.5{\cdot}10^{-3}$ Pa)	Cu rough	6000	1M LPF_6 / EC:DEC:DMC (1:1:1) | Li	0.01–2.0 V, μA cm^{-2}	1220	20	1050	[72]
59	patterned a-Si	MS (NA)	Cu patterned	560	1M LPF_6 / EC:DMC (1:1) | Li	0-1.5 V, 0.5 C	2800	100	2100	[77]

№	Thin film structure	Preparation method	Underlayer (nm)/ Substrate	Thickness (nm)	Cell (Electrolyte || Counter electrode)	Voltage range, Current/C-rate	Reversible discharge specific capacity (mAh g^{-1})	Number of cycles	Last discharge capacity (mAh g^{-1})	Ref.
60	Si nanowires	ED (-2.4 V vs. Pt,)	3D TMV/Ni on SS	80	NA	0.01-1.5 V, 0.25C	2300	173	1200	[88]
61	3D Si anode	LPCVD (SiH_4, 33.3 Pa, 610 °C)	TiN	50	1 M $LiPF_6$ | EC:DEC || Li 1M $LiClO_4$ / PC || Li LIPON (1 μm) || Li	0-3 V, 1C	3500 3600 3500	60	1200 ~2350 3500	[146]
62	a-Si-graphene/carbon nanotubes	MS (rf, 0.5 Pa, 150 W)	graphene/ carbon nanotubes paper	13000	M $LiPF_6$ / EC:DEC (1:1) Li	0.01-2.5 V, 100 mAh g	1417	100	425	[115]
63	porous c-Si nanowires, B-doped	Etching of Si wafers ($HF+AgNO_3$, 3 h)	Si wafer	Diameter and wall ~ 8	NA	0.01-2.0 V, 0,15C 0.3C 0.6C 0.9C 1.2C 2.4C	3700 2600 2000 1900 1700 1300	20	3500 2500 2000 1900 1700 1300	[83]
64	Si nanowires	Vapour–Liquid–Solid growth (SiH_4+Ar, $5.3{\cdot}10^3$ Pa, 485 °C, 20 min)	Au/St. steel	100 (diam.))μm (length)	M LiPF6 / EC:DEC (1:1) Li	0.07-0.7V, C/5 0.07-2V, C/5	1700 2500	80	2000 1300	[238]
65	Si porous, *n*-type	MS (rf, 80 W, 0.66 Pa)	porous Cu	400	1 M $LiPF_6$ / DEC:EC:EMC (1:1:1) || Li	0.1-1.5V, 30 μAcm^{-2}	76 μAcm^{-2}	100	67 μAcm^{-2}	[86]
66	c-Si ribbons	-	Cr/Au/Cr/ PDMS	400	M $LiPF_6$ / EC:DEC (1:1) Li	0.005 – 3 V, C/4	4137	500	3498	[79]

№	Thin film structure	Preparation method	Underlayer (nm)/ Substrate	Thickness (nm)	Cell (Electrolyte || Counter electrode)	Voltage range, Current/C-rate	Reversible discharge specific capacity (mAh g^{-1})	Number of cycles	Last discharge capacity (mAh g^{-1})	Ref.
67	Cu-coated a-Si	MS (rf, 200 W, 0.667 Pa)	Cu/Cu	500	.2 M $LiPF_6$ / EC:DEC (3:7 +10% FEC || Li	0.01-1.2 V, 25 μA cm^{-2}	2100	60	1900	[101]
68	Si/Cu multilayer	MS (NA)	Cu	Si/Cu 50/400	LiPON || $LiCoO_2$	30 nA	16 μAh cm^{-2}	100	14 μAh cm^{-2}	[149]
69	Cu_2O-coated Si	ECR-MOCVD (1.33 Pa, 200°C)	Cu	Cu_2O/Si 200/800	1 M $LiPF_6$ EC:EMC:DC (1:1:1) || Li	0-2 V, 1C	1630	100	500	[102]
70	C-coated a-Si:H	RF-PECVD (200W, 1.3 Pa, SiH_4, 150 °C) + MS (C_{60}, 300 W)	Cu	NA	1M LPF_6 EC:DEC:DMC (1:1:1) || Li	0-2 V, 100 μA cm^{-2}	3500	100	1200	[239]
71	composite a-Si/B	MS (rf/dc, 110 W/150 W, 0.13 Pa)	Cu	NA	1 M $LiPF_6$ / EC:DEC:FEC (3:6:1) || Li	0.005-0.9 V, C/5	3250	3	3250	[96]
72	composite a-Si/Ti	MS (Si – rf, 20-40 W; Ti – dc,150 W, 0.5 Pa)	Ti/quartz	Ti:Si 60 (1:8.78) 30 (1:8.79) 30 (1:8.89)	M $LiPF_6$ / EC:DMC (1:1) Li	NA	250 μAh 140 μAh 310 μAh	20	200 μAh 140 μAh 290 μAh	[100]
73	monolithic Si	MS (rf, NA)	Cr/Cu	250	1 M $LiPF_6$ / EC:DEC (1:2) || Li	0.02-1.2 V, 100-500 μA cm^{-2}	2822	75	~800	[103]
74	composite Si/C bilayer			50/250			2509		~2450	
75	composite C/Si/C tri-layer			50/250/50			2025		~1900	
76	C-coated a-Si algae	PLD (20 Hz, 60-100Pa, 5J/cm^2)	Cu	1000	1M LPF_6 / EC:DEC (1:1) || Li	0.005-1.5 V, 54 μA cm^{-2}	80 μAh cm^{-2}	1000	80 μAh cm^{-2}	[106]

№	Thin film structure	Preparation method	Underlayer (nm)/ Substrate	Thickness (nm)	Cell (Electrolyte || Counter electrode)	Voltage range, Current/C-rate	Reversible discharge specific capacity (mAh g^{-1})	Number of cycles	Last discharge capacity (mAh g^{-1})	Ref.
77	composite Si/C multilayered	PLD (Si – 40 Pa, C- 5 Pa), annealing (400°C)	Cu	1000	M $LiPF_6$ / EC:DMC (1:1) Li	.02-1.5 V, 130 μA cm^{-2}	300 μAh cm^{-2}	100	85 μAh cm^{-2}	[104]
78	composite C/Si	MS ($5 \cdot 10^{-3}$ mbar, 20°C, Si -88 W, C – 40 W)	Cu	5/140 10/140 50/140	1 M $LiPF_6$ / EC:DEC (3:7) + 2% VC || Li	0.04–1.5 V 1C	2750 3000 3250	150	2400 2500 2750	[42]
79	composite Si/C/Si			70/5/70 70/10/70 70/50/70			2900 3000 3300		2600 2600 2750	
80	composite a-Si/C multilayers	MS (rf(Si), dc(C), 300 W, 1 Pa)	Cu	Si:C 500(5:1) 500 (6:1) 500(7:1) 1100(5:1) 1300(5:1)	1 M $LiPF_6$ / EC:DMC || Li	0.01-1.2 V, 1C	2100 2050 1300 100 300	200	2500 2000 250 1900 1700	[110]
81	composite Si/C_{60}	RF-PECVD (200W, 10.6 Pa, SiH_4, 150 °C)	Cu	300	1M LPF_6 / EC:DEC:DMC (1:1:1) || Li	0–2 V, 1500 μA cm^{-2}	2000	30	2500	[105]
82	composite Si/graphene	PLD for Si (<1.3×10^{-5} Pa) CVD for graphene (CH_4, 1050°C),	Ni	graphene/Si 23/6.35	1M $LiPF_6$ / DEC:DEC (1:1 || Li	0.01 - 3.0 V, C/10 to C/1.5	2400	100	NA	[114]

№	Thin film structure	Preparation method	Underlayer (nm)/ Substrate	Thickness (nm)	Cell (Electrolyte || Counter electrode)	Voltage range, Current/C-rate	Reversible discharge specific capacity (mAh g^{-1})	Number of cycles	Last discharge capacity (mAh g^{-1})	Ref.
83	Ti/Si/Ti multilayers	MS (0.5 Pa, 100 W)	Cu	Ti/Si/Ti 8/150/8 16/150/16 24/150/24 32/150/32 40/150/40	M $LiPF_6$ / EC:DEC (1:1) | Li	.01 - 2.0 V, 30 μA cm^{-}	2250 2060 1875 1750 1625	30	1875 1690 1500 1375 1250	[98]
84	Al-coated Si/Cu/Ti multilayers (with Cu_3Si nanowires)	MS (rf, 0.5 Pa, 60 W)	Cu(300)Ti(400)/quartz	Al/Si 0/400 2/400 4/400 8/400	M $LiPF_6$ / EC:DMC (1:1) Li	.005 – 2 V, 20 μA cm^{-}	1500 1000 1000 1000	100	1375 875 750 125	[111]
85	composite Si-Y multilayer	MS (rf, 0.5 Pa, 300°C)	Cu	Y/Si/Y/Si: Si – 225; Y: 15 22.5 30 37.5	1 M $LiPF_6$ / EC:DEC(1:1) | Li	NA	2800 2850 2500 2300	50	2250 2500 2050 1800	[97]
86	SiN-coated Si	Sputtering (dc, 80 W, Ar)	Cu micro-cone arrays	7.7 15.4 23.1	M $LiPF_6$ / EC:EMC (1:1) Li	0.05-1.2 V, 0.2C	2750 1800 1600	200	1250 750 800	[107]
87	composite a-Si-Fe multilayers	EBE (NA)	Cu	245.5	1M LPF_6 / EC:DEC (1:1) || Li	0-1.2 V, 30 μA cm^{-2}	140 μAh cm^{-2}	50	125 μAh cm^{-2}	[93]
88	Ti/Si/Fe multilayers	EBE (NA)	Ni etched	50/2000/400	M $LiPF_6$ / EC:DEC (1:1) Li	0-1.2 V, 200 μA cm^{-2}	450 μAh cm^{-2}	50	450 μAh cm^{-2}	[94]
89	3D a-Si, *n*-type/carbon fiber	MS (rf, 1.33 Pa, Ar)	carbon-fiber on St. steel	Diameter 3000–5000	M $LiPF_6$ / EC:EMC (1:2) Li	.01-1.5 V, 3750 μAcm	~1750	200	1000	[117]

№	Thin film structure	Preparation method	Underlayer (nm)/ Substrate	Thickness (nm)	Cell (Electrolyte || Counter electrode)	Voltage range, Current/C-rate	Reversible discharge specific capacity (mAh g^{-1})	Number of cycles	Last discharge capacity (mAh g^{-1})	Ref.
90	a-Si,*n*-type/graphene/Ni foam	MS for Si rf, 80 W, 0.66 Pa) CVD for graphene (CH_4, 1050°C)	Ni foam	50-400	1M LPF_6 / EC:DEC:EMC (1:1:1) || Li	0.1-1.5V, 30 μA cm^{-2}	141	500	75	[116]
91	3D a-Si, *n*-type/Co nanosheets	MS (rf, 60 W, 1.07 Pa)	Co/Ni	NA	M $LiPF_6$ / EC:DEC (1:1) Li	0-1.5 V, 0.1, 0.5, 1.2, 5C	2340	100	1910	[87]
92	3D Si/Al multilayers	MS (rf, 300 W, 0.75 Pa, Ar)	Cu nanoribbons	1000	1 M LPF_6 / EC:DMC:DEC (1:1:1) + 2% VC || Li 1 M $LiPF_6$ / EC:DMC:DEC (1:1:1) +2% VC + 10% FEC || Li	.1 -1.2 V, 4.2 A g^{-1} (1C 0.1 -1.2 V, 2.1 A g^{-1} (C/2)	1170 ~1800	120 300	1015 1175	[95]